Electrochemical Energy Reviews (2023) 6:27
https://doi.org/10.1007/s41918-023-00186-6

REVIEW ARTICLE

Pathways of the Electrochemical Nitrogen Reduction Reaction: From Ammonia Synthesis to Metal-N_2 Batteries

Sebastian Cyril Jesudass[1] · Subramani Surendran[2] · Joon Young Kim[2,3] · Tae-Yong An[2] · Gnanaprakasam Janani[2] · Tae-Hoon Kim[1] · Jung Kyu Kim[4] · Uk Sim[2,3]

Received: 14 April 2022 / Revised: 15 September 2022 / Accepted: 20 March 2023 / Published online: 3 August 2023

Abstract

Ammonia is considered as an alternative fuel resource for a sustainable green future. The production of ammonia involves the electrochemical nitrogen reduction reaction (NRR), which has gained considerable attention due to its eco-friendly resources and nonharmful byproducts. Even with the manifold works on NRR, the technique has not reached the industrial scale because of the impediments of NRR electrocatalysts, and in addition, state-of-the-art electrocatalysts have not yet been discovered. In this review, first, the mechanism of the NRR, key metrics, and operational procedures for NRR electrochemistry are presented. Then, the electrocatalyst designs for efficient NRR are briefly introduced, followed by a discussion on the influence of the electrolytes that enhance NRR performance. The counterion effects of electrolytes on NRR performance and strategies for suppressing the HER by electrolyte additives are also discussed. Later, the NRR mechanisms are upgraded, and a comprehensive review of metal-N_2 batteries is provided. This review summarizes the effective methods for performing the NRR and strategies to suppress the HER on various electrocatalysts by tuning electrolytes and their additives. The review concludes by discussing the prospects of metal-N_2 batteries.

Keywords Sustainable energy · NRR electrochemistry · Electrocatalysts · Electrolytes · Metal-N_2 battery

1 Introduction

The world's population is expected to reach 11 billion by the end of this century (2100) from 7.7 billion people in 2019, according to a report launched by the United Nations (UN) [1]. Modern energy demands, due to this profusion, have put forward an essential threat to seeking renewable, sustainable, economical, and eco-friendly strategies for tackling the upcoming energy crisis. The development of electrocatalysts paved an efficient, economical path to obtain products, such as hydrogen (H_2), ammonia (NH_3), and hydrocarbons, and the production of value-added chemicals from earth-abundant materials, such as water, nitrogen (N_2), oxygen (O_2) and carbon dioxide (CO_2). Over decades, scientists have relentlessly designed electrocatalysts that target the nitrogen reduction reaction (NRR) [2], hydrogen evolution reaction (HER) [3], oxygen reduction reaction (ORR) [4], carbon dioxide reduction reaction (CO_2RR) [5], and many other [6] electrochemical reactions that facilitate the formation of fuel products and value-added chemicals.

Among the valuable fuel products, ammonia (NH_3) has stood out greatly, exhibiting better storage and transport

Sebastian Cyril Jesudass, Subramani Surendran and Joonyoung Kim have contributed equally to this work.bio

✉ Tae-Hoon Kim
thk@jnu.ac.kr

✉ Jung Kyu Kim
legkim@skku.edu

✉ Uk Sim
usim@kentech.ac.kr

1 Department of Materials Science and Engineering, Chonnam National University, Gwangju 61186, Republic of Korea

2 Hydrogen Energy Technology Laboratory, Korea Institute of Energy Technology (KENTECH), Naju, Jeollanamdo 58330, Republic of Korea

3 Research Institute, NEEL Sciences, Inc., Naju 58326, Republic of Korea

4 School of Chemical Engineering, Sungkyunkwan University, 2066 Seobu-Ro, Jangan-Gu, Suwon 16419, Republic of Korea

facilities and more cost-efficient and eco-friendly production pathways than hydrogen, and ammonia is a long-term energy resource that serves as a low-cost hydrogen energy carrier [7]. Additionally, it serves as a source of fertilizers for agriculture and raw materials for explosives and coolants. The efficient production of ammonia, as shown in Eq. (1), has invariably been an important part of research interests for decades [8]. Currently, major ammonia production follows the polluting Haber–Bosch process. The Haber–Bosch technique uses high temperatures of approximately 350 °C and pressures ranging from 250 to 350 bar (1 bar = 100 000 Pa), and the minimum energy consumption is approximately 27.4–31.8 GJ $t_{NH_3}^{-1}$ with an efficiency of 65% [9]. This higher energy consumption in the Haber–Bosch process can be lessened by alternative routes, an enzymatic pathway and an electrochemical pathway. Along the enzymatic pathway, nitrogenase enzymes produce more hydrogen than the required ammonia, which shows the unreliability of the enzymatic pathway [10]. Ultimately, the choices are reduced to the electrochemical NRR, which is a promising candidate for green ammonia production.

$$N_2 + 3H_2 \rightarrow 2NH_3 \ \Delta H_f^\circ = -45.9 \text{ kJ mol}^{-1} \quad (1)$$

Electrochemical ammonia production involves NRR that adsorbs N_2 molecules on the catalyst surface. The electrochemical NRR uses electricity derived from renewable sources and N_2, along with protons from water dissociation.

Figure 1 represents the electrochemical ammonia production from water and renewable electricity and its application in various industrial and transportation sectors. Electrochemical NRR in an electrochemical cell is promoted by using an electrocatalyst that efficiently adsorbs N_2 gas onto the electrode surface and reduces it to ammonia. Electrocatalysts with a large surface area, highly porous structures with intrinsic catalytic activity, and excellent bulk conductivity exhibit better nitrogen adsorption energies and stability to catalyse the electrochemical reaction. However, this electrochemical NRR is suppressed by the slower kinetics of nitrogen adsorption onto the surface, and the splitting of the N_2 triple bond leads to reduced faradaic efficiency (FE) and lower ammonia production rates [11]. Studies show that the limiting potential of the HER is smaller than that of the NRR, which indicates that the HER competes with the NRR with smaller potentials for H_2 evolution in an electrocatalyst [12]. Additionally, from a kinetic point of view, protons and electrons undergo H_2 formation rather than NH_3 formation, which accounts for the extremely low faradaic efficiency (FE) and the reduction in ammonia yield of the electrocatalysts [13]. Thus, electrocatalysts are classified as noble metal-based, nonnoble metal-based, metal-free, and single-atom catalysts (SACs) that exhibit different orders of activity depending on their unique surface adsorption properties and affinity towards N_2 triple bond splitting.

HER suppression is of utmost importance for effective NRR performance. The active sites of the electrocatalyst are heavily utilized by the protons from the electrolyte because

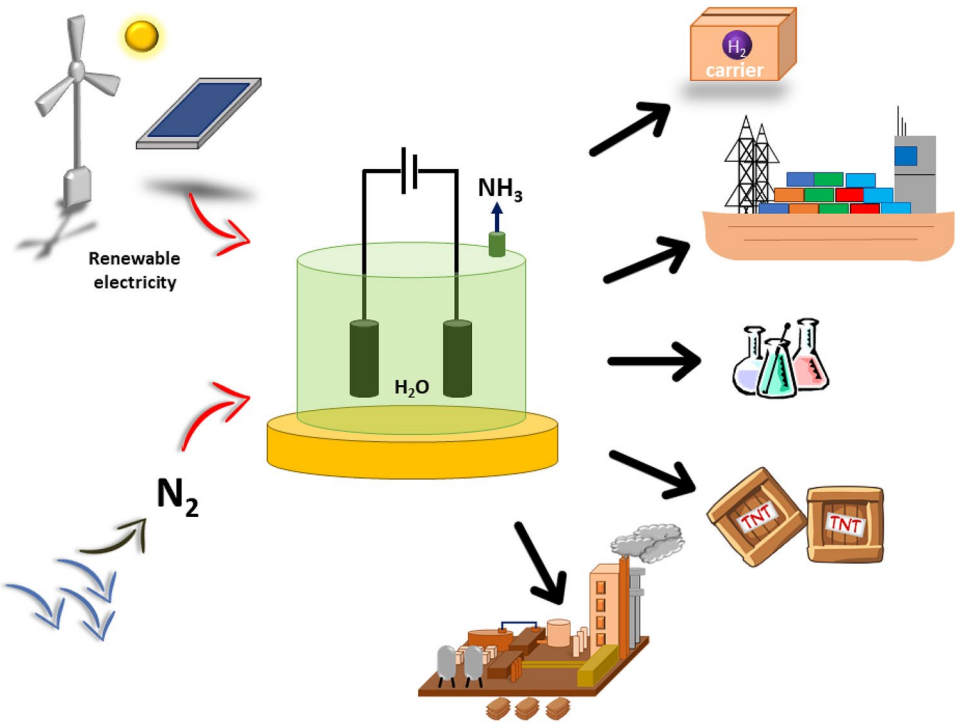

Fig. 1 Schematic of electrochemical ammonia production and its application in various sectors

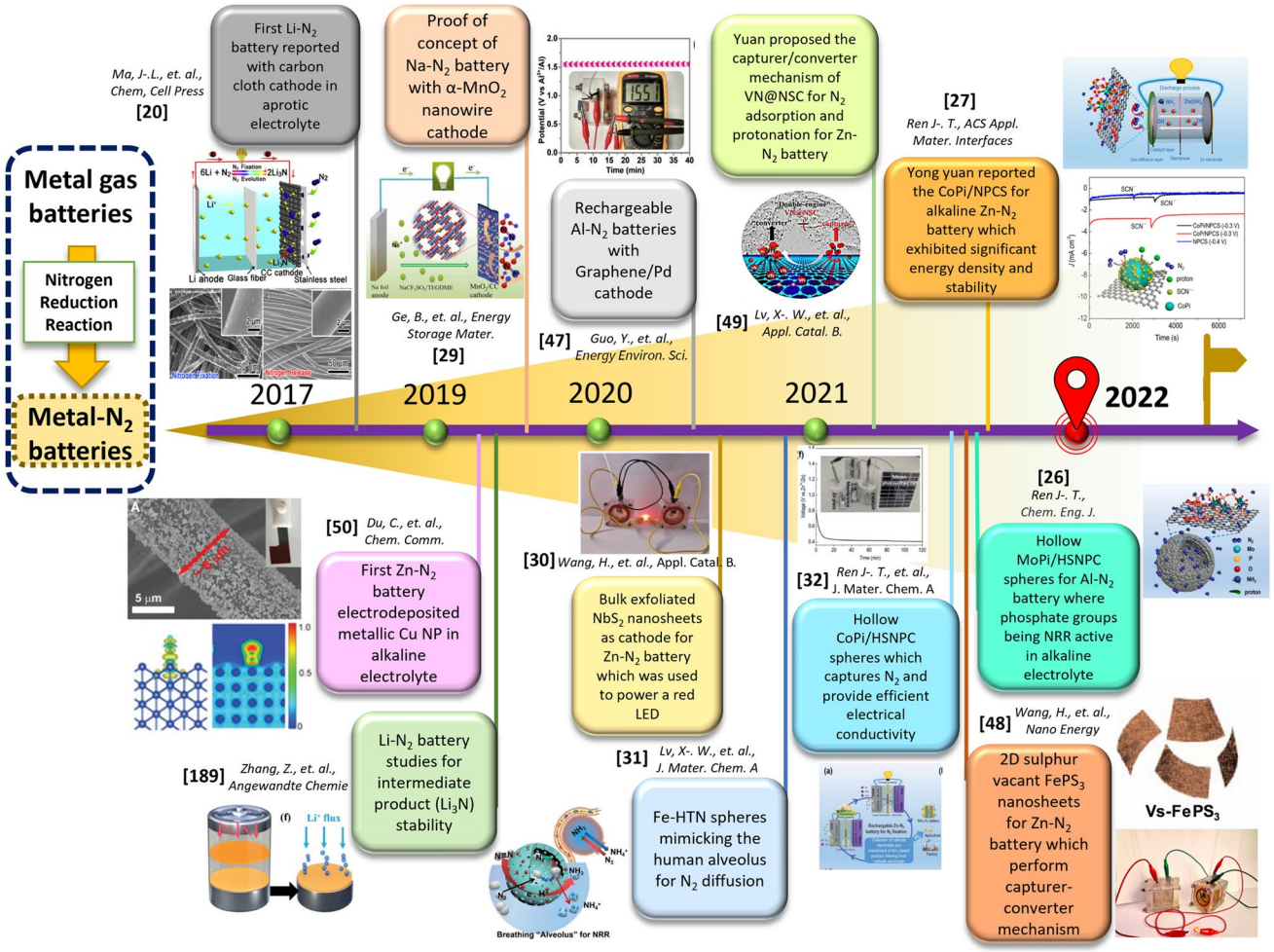

Fig. 2 Timeline representing the advancements in metal-N_2 batteries over the years. Adapted with permission from Ref. [20, 26, 29, 30, 48, 49]. Copyrights © 2017, 2019, 2020, 2021 Elsevier Ltd. Adapted with permission from Ref. [27]. Copyrights © 2021, American Chemical Society. Adapted with permission from Refs. [31, 32, 47, 50]. Copyrights © 2019, 2020, 2021, Royal Society of Chemistry. Adapted with permission from Ref. [189]. Copyrights (c) 2019, John Wiley & Sons, Inc

of the electronic effects between the electrocatalyst and the H^+ ions. This usage has a negative impact on the ammonia yield and the FE of the electrocatalyst, reducing the NRR performance. Hence, selectivity towards N_2 must be increased for electrocatalysts over the HER. Strategies such as tuning the d-bands of the electrocatalyst [14] and electrolyte modifications [15-17] have been followed and promising results are shown in reducing the HER. In later sections, we clearly discuss the important strategies that inhibit the HER for efficient NRR performance.

Upgrading the electrochemical NRR mechanisms into an energy storage device has proven to be the most needed plan for the current energy-demanding society. The importance of electrochemical energy storage (EES) devices has increased in the modern era of technology for electric vehicles and smart grid power storage [18, 19]. Various EES devices, such as rechargeable batteries, flow batteries, metal gas batteries, supercapacitors, and fuel cells, can store energy from smart grids and supply as needed. Among these devices, metal N_2 batteries have started attracting attention due to their readily available resources and the importance of the final product. Metal-N_2 batteries have importance due to ammonia production with simultaneous electricity generation. The history of metal-N_2 batteries dates back to 2017 when Zhang et al. [20-25] decided to fabricate a rechargeable Li-N_2 battery inspired by the high energy density of metal gas batteries, Al-CO_2, Li-CO_2, Li-SO_2, Na-CO_2, and Li-O_2. Later, several reports were published in response to the novelty of the work and prime expectations of metal-N_2 battery systems, as shown in Fig. 2 [26]. Soon after the first Zn-N_2 battery was reported in 2019 under an aqueous alkaline electrolyte, novel design strategies for the electrocatalyst were proposed and demonstrated as cathodes for the Zn-N_2

battery. The aprotic electrolytes in metal-N_2 batteries make their construction and maintenance tedious. Fortunately, alkaline metal-N_2 batteries have provided a safer, promising, and reliable approach due to the wide availability of resources and low maintenance costs. However, the limited NRR performance of alkaline metal-N_2 batteries shows the incubatory stage of these batteries for which various electrocatalysts have been constantly engineered to meet the current demands.

Presently, various metal-N_2 batteries are available, each having its own advantage owing to its cathode reactivity and anode configuration. An active electrocatalyst as the cathode is the integral unit for the battery because it effectively increases the activity by offering minimum resistance for the charge−discharge mechanisms. To date, only a few metal-N_2 batteries have been demonstrated (Li-N_2, Na-N_2, Al-N_2, Zn-N_2), and further upgrades to increase the faradaic efficiency (FE) and ammonia yield of electrocatalysts with a higher power density are foreseen. The real challenge lies in the activation of the strong triple bond of the nitrogen molecule, which prevents the battery system from reaching maturity.

Metal-N_2 batteries simultaneously undergo redox reactions at the cathode and metal anode to drive the charge storage mechanism. In the case of metal-N_2 batteries, N_2 reduction and oxidation reactions occur at the cathode for the discharge−charge cycles, respectively [20, 27]. Therefore, simultaneous ammonia production and electricity generation can be manifested over metal-N_2 batteries, which show importance over conventional metal-air batteries [27, 28]. Among the reported metal-N_2 batteries, including Li-N_2 batteries [20], Na-N_2 batteries [29], and Al-N_2 batteries [26], Zn-N_2 batteries hold great prospects due to the stability of the Zn anode in an alkaline environment and the fabrication of the battery in an ambient atmosphere [30]. In addition, Zn is widely available in the Earth's crust, is eco-friendly, has high capacity and stable discharge potential, and is a mature technology compared to other batteries [31, 32]. Therefore, Zn-N_2 batteries hold assuring commercial value and can be easily developed to provide industrial-scale applications.

The present review article focuses on the rational design strategies of an electrocatalyst from electrochemical NRR into metal-N_2 batteries. The review includes discussions on the novel electrocatalyst design strategies and the mechanisms of different electrocatalyst structures. The important role of electrolytes and the counterions in the electrolytes in driving the electrochemical NRR are reviewed. The advantage of suppressing the HER by electrolyte modifications is also explained. Moreover, incorporating NRR electrocatalysts into the metal-N_2 battery system and future aspects of metal-N_2 batteries are also discussed. Based on this discussion, the review develops a research orientation to incorporate an electrocatalyst as an active cathode for potential metal-N_2 battery applications.

2 Fundamentals of Electrochemical NRR and Metal-N_2 Batteries

The reduction of nitrogen to ammonia via the electrochemical NRR route is a feasible green method, and this approach is more energy efficient than the conventional Haber–Bosch process because of the low operating temperature. The electrochemical NRR process uses water, rather than natural gas, as a H_2 source [33]. NRR occurring at the electrocatalyst surface must be immune to hydrogen adsorption. The merits of the electrocatalyst include improving NRR selectivity and increasing ammonia yield and FE. NRR at the electrocatalyst surface occurs at more negative potentials, which can be compromised by HER. From a thermodynamic perspective, we can observe the HER being more favourable than the NRR due to the lower free energy of formation required for H_2 [34].

2.1 Theory of N_2 Adsorption

Nitrogen (N_2), a homonuclear nonpolar molecule, is a Lewis base surrounded by a lone pair of electrons. It does not possess a permanent dipole moment because of the even distribution of charges and equal sharing of electrons, as shown in Fig. 3a. Moreover, N_2 has a triple bond, with each atom holding 7 electrons with an electronic configuration of $1s^2 2s^2 2p^3$, which has pairs of electrons in the s orbitals with opposite spin and electrons in the p orbital with the same spin. N_2 forms a triple bond that exhibits excellent stability. However, ammonia production solely lies in N_2 bond cleavage and initial protonation. Further difficulties can be offered by the thermodynamic constraints from the intermediates during catalytic N_2 reduction [35, 36]. The adsorption of N_2 onto the electrocatalyst surface occurs at specific electron-deficient active sites. The active sites include transition metal sites with unoccupied d orbitals or heteroatoms with sp^2 orbitals that actively adsorb N_2.

As shown in Fig. 3b, c, the unoccupied d-orbitals receive an electron from N_2 to form a σ-bond and donate another occupied d-orbital electron back into the vacant π^* antibonding orbital, creating a π-back-donation effect, called the "donor–acceptor" mechanism. The donor–acceptor mechanism on N_2 activates the triple bond and forces it to remain adsorbed in the active site. Similarly, in the case of nonmetals, the vacant sites and the Lewis acid sites with an empty orbital accept an electron from N_2 to form a σ-bond and supply an electron from the neighbouring site into the π^* orbital of N_2, promoting the activation of the triple bond, as shown in Fig. 3d. This donor–acceptor mechanism of activating

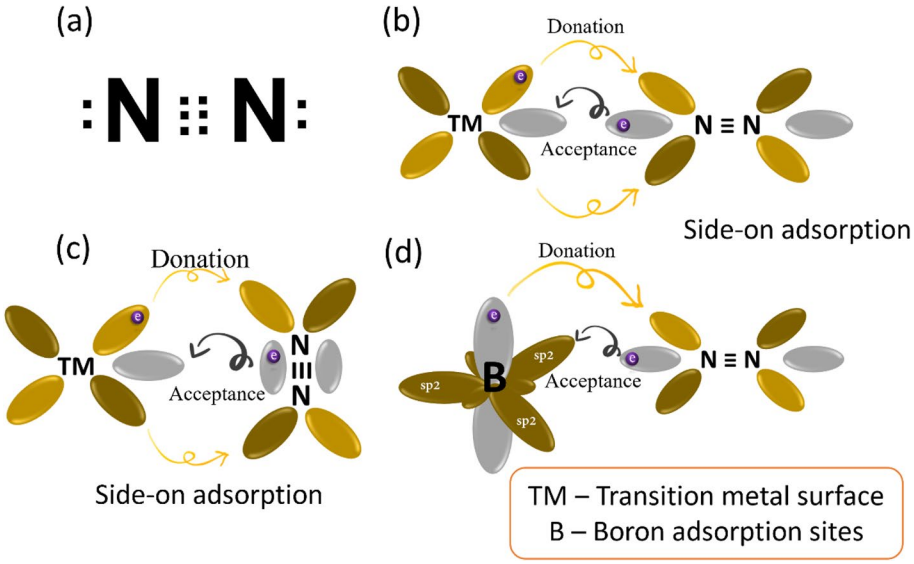

Fig. 3 **a** Representation of the N_2 molecule—Lewis dot structure. Orbital interaction on the transition metal centre via **b** end-on adsorption and **c** side-on adsorption. **d** Heteroatom sp^2 orbital interaction of the N_2 molecule

the N_2 triple bond has provided a general idea for designing electrocatalysts with transition metals and nonmetal substrates that exhibit higher affinity towards N_2 adsorption [36, 37].

2.2 Mechanism of N_2 Reduction

Ammonia can be produced by reducing N_2 in an electrochemical cell. Successful electrochemical N_2 reduction may follow an indirect pathway or a direct pathway. The indirect pathway is mediated through nonaqueous aprotic electrolytes and involves forming intermediates. These intermediates are usually the corresponding metal nitrides that can be hydrolysed to produce ammonia. Because of the instability, recyclability, and scalability of nonaqueous electrolytes, indirect ammonia synthesis does not compete with the current demands. However, because of the limited proton content, the indirect approach effectively suppresses the HER and side reactions, which produce higher ammonia yields with higher FE [38-42]. The Li-mediated ammonia synthesis (LiMEAS) pathway has been recognized by researchers and shows promising ammonia yields involving nitrides, but the process is energetically expensive and involves a two-step ammonia production method [40, 41, 43]. The direct pathway can be divided into two categories based on the nature of the electrolyte, viz., nonaqueous and aqueous. Ammonia production in nonaqueous electrolytes uses sacrificial proton donors, such as alcohols or cationic complexes, to protonate the adsorbed N_2 into ammonia [38, 39, 41, 42]. Ammonia production in aqueous electrolytes utilizes water as the proton source, which may be acidic, alkaline, or neutral in nature, for direct ammonia synthesis. The aqueous pathway is the most feasible approach to produce ammonia from atmospheric N_2, protons from water, and electricity from renewable sources.

Direct ammonia synthesis occurs under various pathways, of which dissociative and associative pathways are primarily followed. The dissociative and associative mechanisms are differentiated by either direct dissociation of the N_2 triple bond or by protonation of the adsorbed N_2 molecule, respectively. Furthermore, the associative mechanism is classified into two pathways: associative alternating and associative distal, as shown in Fig. 4. The dissociative pathway involves a large kinetic barrier that consumes high input energy for N_2 triple bond dissociation ($\Delta H = 941$ kJ mol^{-1}) [44]. The hydrogenation of the dissociative adsorbed N usually occurs with the H_2 produced from natural gas, producing CO_2 as the byproduct.

The associative pathway reduces the nitrogen molecule into ammonia in six proton-coupled electron transfer (PCET) steps. In the associative pathway, the N−N bond remains intact until all or some of the hydrogenation process is under the influence of end-on adsorption of dinitrogen to the catalyst surface. Moreover, this associative mechanism is further classified into alternating and distal pathways based on the sequential addition of hydrogen to the activated dinitrogen. In the associative alternating pathway, hydrogenation occurs simultaneously on both nitrogen atoms, and the ammonia molecule is released in the subsequent steps, as shown in Fig. 4b. In the associative distal pathway, the hydrogenation series occurs only on the first nitrogen atom, and only after the release of the first ammonia molecule does protonation of the other nitrogen occur, as shown in Fig. 4c [35].

Apart from these mechanisms, another pathway preferentially occurs on the surface of transition metal nitrides (TMNs) called the Mars–van Krevelen (MvK) mechanism, as shown in Fig. 4d [45]. In this pathway, first, the nitrogen

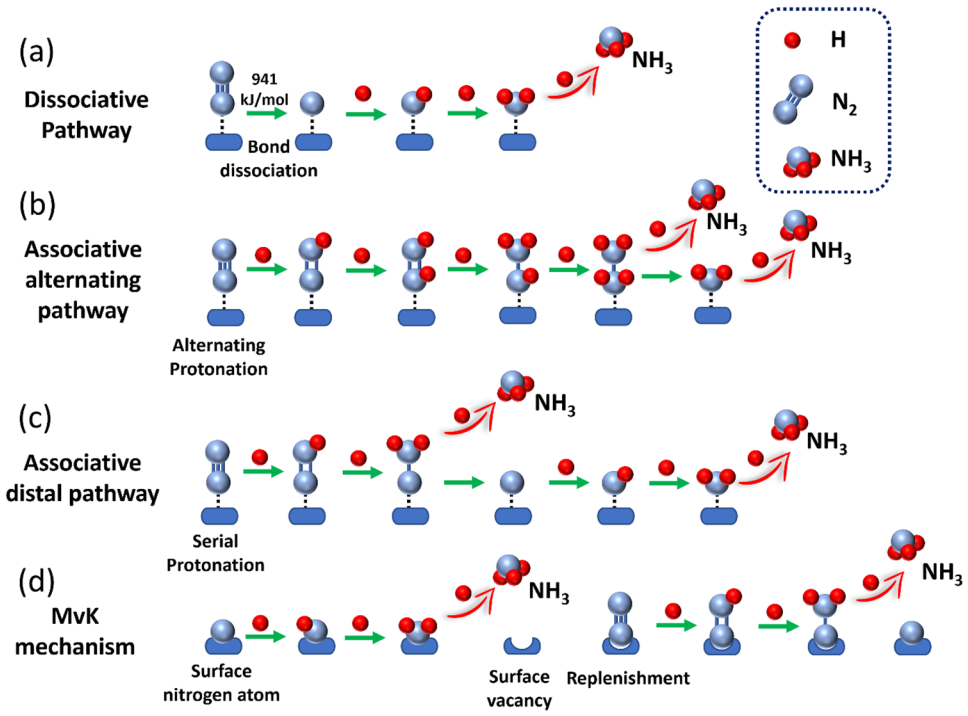

Fig. 4 Reaction scheme representing various electrochemical NRR mechanisms: **a** dissociative, **b** alternating associative, **c** distal associative, **d** and MvK mechanism

atoms on the surface of the catalyst are protonated to reduce to ammonia (NH_3), leaving behind a vacancy. Later, the vacancy is replenished with externally supplied nitrogen gas and is reduced to ammonia following the distal pathway [46]. In particular cases, the nitrogen atoms from the bulk are transferred to the N-vacant sites and are consecutively reduced to ammonia. This bulk migration of the N atoms to the surface transforms the electrocatalyst, hindering its stability [46].

2.3 Metal-N_2 Battery

Metal-air batteries have had a large impact on the scope of efficient energy storage devices. Inspired by the dual role of metal-CO_2 batteries in gas conversion with simultaneous electricity generation, researchers envision the metal-N_2 battery system for greater utilization of the conversion of atmospheric N_2. Similar to metal-air batteries, the metal-N_2 battery is constructed with a metal anode and NRR electrocatalyst-coated electrode as the cathode [20, 32, 47]. The electrode terms cathode and anode for the electrocatalyst-coated electrode and metal electrode remain the same, irrespective of the charge−discharge cycles. The mechanism of the metal-N_2 battery with the electrode terms is explained below for further clarification. The redox reaction in a metal-N_2 battery varies with the nature of the electrolyte, viz., nonaqueous and aqueous electrolytes. In a nonaqueous metal-N_2 battery, during discharge, N_2 reduction at the cathode by the corresponding metal ions forms nitrides (Fig. 5a), which can later be hydrolysed to ammonia [20, 29, 47]. During charging, under an external bias, the nitrides at the cathode dissociate into metal ions and gaseous nitrogen, as shown in Fig. 5b [20, 29, 47]. The cathode serves as a conductive substrate as well as a nucleation site for anchoring the discharge products in nonaqueous metal-N_2 batteries. The common nonaqueous batteries fabricated thus far are the Li-N_2 battery, Na-N_2 battery, and Al-N_2 battery [20, 29, 47].

Because of the economic, operational, and maintenance difficulties of using aprotic electrolytes, research has been targeted to design aqueous metal-N_2 batteries [26, 27, 30-32, 48, 49]. In aqueous metal-N_2 batteries, the cathode proceeds through the nitrogen reduction reaction (NRR) and oxygen evolution reaction (OER) during discharging and charging, respectively [32]. During discharging, the cathodic reaction is the NRR, which draws electrons and protons from the oxidized metal anode and electrolyte, respectively, forming ammonia (Fig. 5c) [26, 31]. Thus, simultaneous ammonia production and electricity generation can be manifested [49, 50].

During charging, the external bias reduces the oxidized metal, and the direction of electron flow is reversed (Fig. 5d) [32]. Accordingly, the anodic reaction over the cathode evolves oxygen as a result of the OER. The oxidation reaction at the electrocatalyst incorporates electrons into the cathode from the electrolytic hydroxide anions. Thus, in an alkaline metal-N_2 battery, the discharge process at the cathode occurs with the NRR, resulting in ammonia formation, and the charging process at the cathode occurs with the OER.

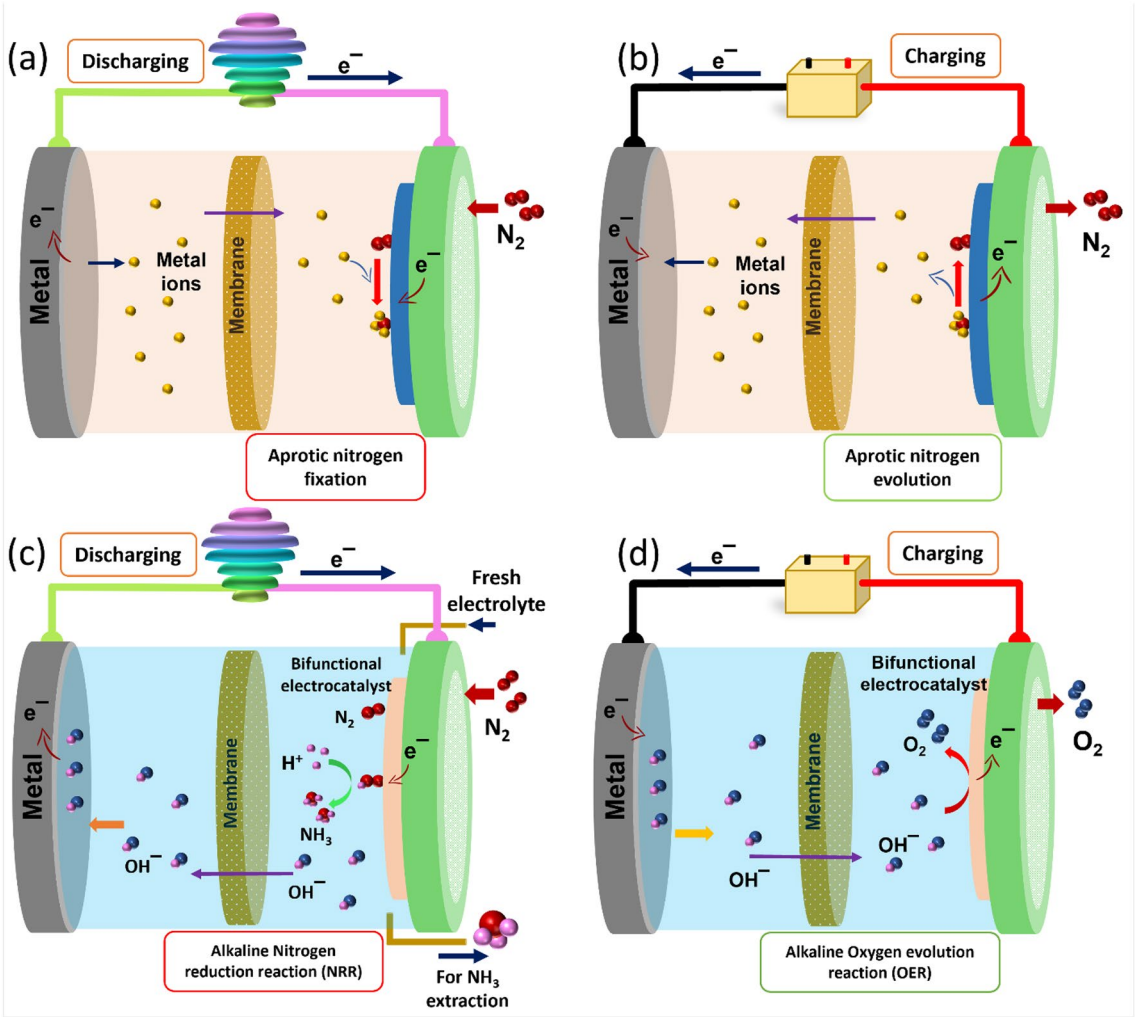

Fig. 5 Schematic of the metal-N_2 battery and its discharge−charge mechanisms in **a**, **b** aprotic electrolytes and **c**, **d** alkaline electrolytes

The NRR during discharge usually follows the associative pathway or the MvK mechanism, as stated previously, depending on the nature of the electrocatalyst. The mechanism of the OER following a 4-electron pathway during charging is stated below [51, 52].

$$^{*} + OH^{-} \rightarrow ^{*}OH + e^{-} \quad (2)$$

$$^{*}OH + OH^{-} \rightarrow ^{*}O + e^{-} + H_2O \quad (3)$$

$$^{*}O + OH^{-} \rightarrow ^{*}OOH + e^{-} \quad (4)$$

$$^{*}OOH + OH^{-} \rightarrow ^{*} O_2 + e^{-} + H_2O \quad (5)$$

where * represents the surface adsorption site of the bifunctional electrocatalyst at the cathode. Initially, upon charging, the first hydroxide ion is adsorbed on the electrode active site by one electron transfer (Eq. 2). Then, the second and third hydroxide ions react with the adsorbed hydroxide ion to form oxide and oxyhydroxides, which involve the second and third electron transfer steps (Eqs. 3, 4), respectively. Finally, the fourth OH^- ion reacts with the oxyhydroxide to release water and oxygen molecules into the electrolyte (Eq. 5).

2.4 Key Metrics in Determining NRR Performance

The key parameters for determining the rate of the NRR are ammonia yield and faradaic efficiency (FE). Graphs are drawn for the applied potential (V) vs. the obtained production rate of ammonia and FE, respectively. These parameters determine the activity of the electrocatalyst towards the NRR and its selectivity over the HER.

2.4.1 Calculation of Ammonia (NH_3) Yield

The NH_3 yield rate indicates the amount of ammonia produced per catalyst loading mass/area and unit time, which directly relates to the adsorption (N_2)/desorption (NH_3) properties of the electrocatalyst. Experimentally, the ammonia yield is measured by using chronoamperometry analysis for a period of time and evaluated through Eq. (6).

$$r_{NH_3} = \frac{[NH_4^+] \times V}{t \times A} \tag{6}$$

where $[NH_4^+]$ is the measured concentration of ammonia from UV−vis spectrometry and the calibration curves of the standard ammonia solution, V is the volume of the electrolyte, t is the reaction time, and A is the electrode surface area [53].

2.4.2 Calculation of Faradaic Efficiency (FE)

Faradaic efficiency (FE) is given by the ratio of the faradaic current used for the NRR to the total current supplied to the electrochemical system. This parameter determines the selectivity of the electrochemical process of the NRR over the competing HER. The FE of any catalyst surface can be obtained using Eq. (7).

$$\mathrm{FE}/(\%) = \frac{3F \times r_{NH_3}}{j} \tag{7}$$

where 3 is the number of electrons for producing one NH_3 molecule, F is the Faraday constant ($F = 96\,485.33$), and j is the current density measured for the corresponding ammonia yield r_{NH_3} [53].

2.4.3 Determination of Cell Voltage

Experimentally, the cell potential is calculated by determining the potential difference between the two electrodes (cathode and anode) and is expressed in volts (V), as shown in Eq. (8) [54].

$$E^\circ = E^\circ_{\mathrm{cathode}} - E^\circ_{\mathrm{anode}} \tag{8}$$

2.5 Determination and Analysis Techniques

Detecting and quantifying the produced ammonia, postsynthesis, is essential for reviewing the NRR activity of the electrocatalyst. The detection techniques are performed on the sampled electrolyte, and the methods for ammonia detection must be extremely delicate, dependable, precise, and reproducible. Ammonia quantification must be accurate because of various factors that contribute to overestimating ammonia, such as the time of quantification, the pH of the solution, foreign agents that produce ammonia-containing products other than the catalyst, and the nature of the electrolyte. Initially, ammonia detection is performed on the sampled electrolyte by the UV−vis spectrophotometric method, involving the colouring agents of –(N=N)–. Later, the quantification of the produced ammonia using $^{15}N_2$ feeding gas was observed to verify the source of nitrogen used in ammonia synthesis [55, 56].

2.5.1 Spectrophotometry Method

The spectrophotometry method, also known as the colourimetric method, is based on the Berthelot reaction, which involves the indophenol blue method to form a dye product with produced ammonia. This product can be observed under UV−vis spectroscopy to record the absorption spectrum at certain wavelengths corresponding to the above-mentioned methods. The indophenol blue method, because of its lower detection limit (0–0.6 mg NH_3–N L^{-1}), better reproducibility, and consistent colour development, is preferred. In this method, the sampled electrolyte is treated with a colouring solution of NaOH containing salicylic acid and sodium citrate. To this solution, a catalyst solution of sodium nitroprusside in DI water and oxidizing solution made of sodium hypochlorite (NaOCl) in NaOH is added [7, 57, 58]. The resulting solution is left undisturbed for an hour, and the UV−vis absorption spectra are recorded. The spectra reveal an absorption band at approximately 680 nm corresponding to the blue region, indicating the presence of ammonia. The higher the intensity of the absorption peak is, the higher the concentration of ammonia in the sample is. To calculate the concentration of the produced ammonia, concentration–calibration graphs are drawn for the standard solution of ammonia, and peak fitting gives the obtained ammonia concentration.

The peak fitting of the concentration–absorbance graph at the absorption peak maximum gives a linear equation $y = mx + c$. The straight-line equation is the linear relation between absorbance and the concentration of the standard ammonia solution, as shown in Eq. (9).

$$A = \varepsilon C + b \tag{9}$$

where A is the absorbance intensity, ε is the molar extinction coefficient (the slope) obtained from the concentration–calibration graph, C is the concentration of the ammonia in the sample, and b is the y-intercept of the concentration–calibration graph. The absorbance values for a particular voltage for an electrocatalyst are applied to the linear equation to calculate the concentration of the produced ammonia in the sample. Irrespective of the method used for ammonia

determination, a second procedure for quantifying ammonia is also needed to account for the source of produced ammonia.

2.5.2 Isotope Labelling Method

The isotope labelling procedure is followed to quantify the source of the produced ammonia, which is either N from the substrate or the N_2 feeding gas. The isotope labelling method for ammonia quantification uses $^{15}N_2$ as the feeding gas, whose chemical properties do not greatly differ from those of $^{14}N_2$. NRR experiments under $^{15}N_2$ feeding gas can be used to quantify the source of the produced ammonia. The sampled electrolyte after NRR experiments with $^{15}N_2$ feeding gas must contain only $^{15}NH_4^+$ ions; therefore, any other contaminants from the catalyst or impurities from the electrolyte can be easily neglected to determine the actual ammonia yield rate due to the NRR. For the $^{15}N_2$ feeding gas experiment, the amount of detected $^{15}NH_4^+$ must be greater than that of $^{14}NH_4^+$, and the total ammonia yields for the $^{15}N_2$ and $^{14}N_2$ feeding gases must be similar. The similar ammonia yield results corroborate that no external impurities or degradation of the catalyst contributed to the final ammonia yield [59]. Thus, determining and quantifying the produced ammonia are essential parameters of the NRR, and purified gas must be provided to avoid any contamination and false determination.

3 Electrocatalysts for Ammonia Production

Electrochemical NRR is a possible route for synthesizing ammonia under ambient conditions. The stable nonpolar bonds of N_2 make the molecule chemically inert, which inhibits N_2 bond cleavage in an ambient atmosphere. This problem outlines the need for an electrocatalyst with high selectivity towards N_2 adsorption and sufficient energy to activate the triple bonds. The electrocatalysts must offer a few amenities that promote N_2 adsorption and NH_3 desorption, thereby limiting the HER, which can be fabricated as an electrode in a metal-N_2 battery. The Sabatier principle states that "the binding energy between the catalyst and the reactant must be neither too strong nor too weak." This rule is the key aspect of designing any electrocatalyst and is of major concern when screening electrocatalytic materials that exhibit sustainability over cost [60].

Activity, selectivity, and stability are the three parameters that determine the performance of an electrocatalyst. For efficient activity, the catalyst must have many available active sites and sufficient pore sizes for the reactants to access the active sites. In selectivity, the material must have surface adsorption potentials that favour the electrochemical NRR by inhibiting the inimical HER. Finally, the catalyst must have a stable structure and tolerate corrosion to sustain long-term operation that eventually reduces the maintenance cost and achieves the efficient use of materials for designing electrocatalysts.

3.1 Screening Metals for NRR Electrocatalysis

An indispensable aspect of electrocatalytic material is selectivity for the valuable NRR over the hindering HER. Theoretically, the best electrocatalysts are transition metals, which were analysed by Skúlason et al. [35] for efficient NRR electrolysis and derived from a volcano plot. The plot sorts out the possibility of using d-metals as catalysts for their preferred activity and selectivity towards the NRR, as shown in Fig. 6a. The top of the diagram indicates that Rh, Ru, and Ir have the highest H adsorption energies, while Pd and Pt are at more negative energies, which indicate prime H adsorption. Moreover, transition metals such as Zr, Sc, Y, and Ti show more negative N adsorption energies, as observed from theoretical studies. Later, researchers used screening procedures to compile and engineer materials suitable for the requirements using simulations and experimental procedures. In addition, Dražević et al. [61] studied the N_2 binding energy parameters from experimental data and the limiting potentials from DFT studies. The study includes the results from Trasatti et al. [62], who calculated the possible HER reactivity of metals and derived a plot to demonstrate the binding energies of the M−H bond over various metals (Fig. 6b).

The result of the study of M−N binding energy was a volcano plot, as shown in Fig. 6c, d, which revealed Mn, Ga, and In as potential NRR candidates and unidentified elements on top of the plot. Combining the experimental HER exchange current densities and the Pourbaix diagrams, the author confirmed the preferable activity of Mn, Ga, and In towards the NRR in water over the HER. However, contrary to previous studies, Fe, Au, Cu, Bi, and Pd required smaller potentials to initiate the HER than the NRR. Similar studies have been performed to evaluate the selectivity for N_2 adsorption for efficient HER suppression and preferential NRR pathways over modified transition metal-incorporated carbon-based electrocatalysts [63, 64]. Thus, an effective screening of various metals helps experimentalists to design an electrocatalyst preferring the NRR over the HER with an appropriate choice of metals.

The electrocatalysts are primarily classified into three categories based on the materials used for their construction, viz., noble metal-based, nonnoble metal-based, and metal-free catalysts. Researchers have developed technologies for screening efficient metal and nonmetal surfaces by theoretical studies that indicate the redox potentials available on the

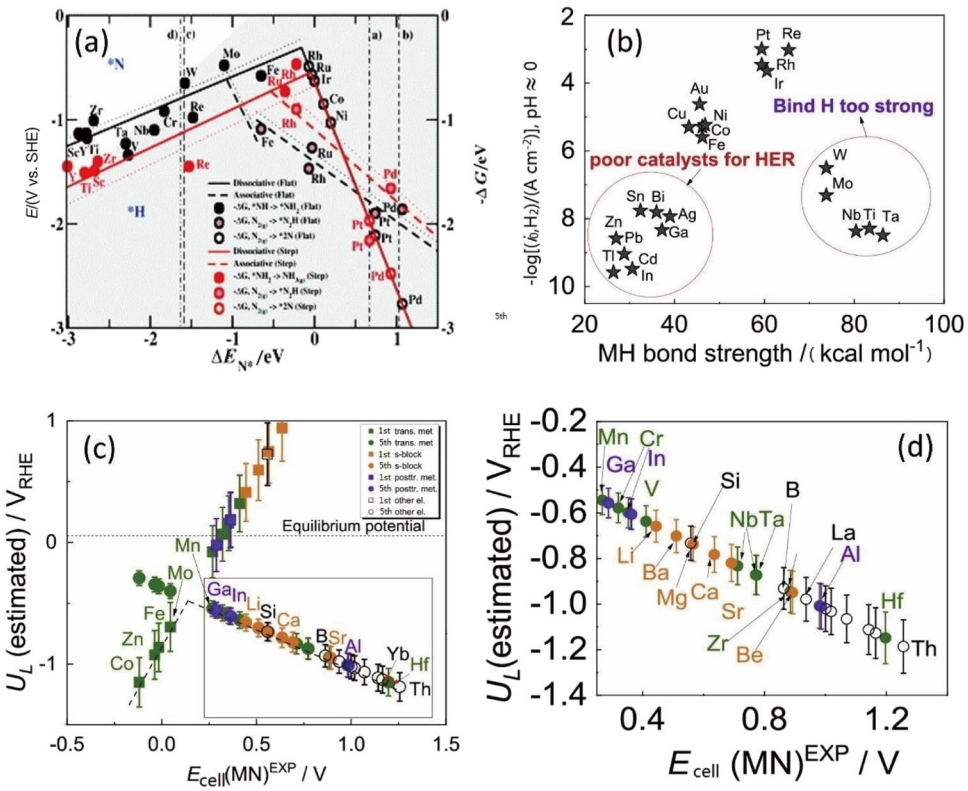

Fig. 6 **a** Volcano plot for the reduction of nitrogen on transition metal surfaces through dissociative and associative mechanisms. Reprinted with permission from Ref. [35]. Copyright © 2011, The Royal Society of Chemistry. **b** Volcano plots for the exchange current density of HER vs. MH bond strengths for different metals; 1 kcal mol^{-1} = 4 185.85 J mol^{-1}. **c** Volcano plots for 31 metals for the estimated limiting potentials of the first and fifth PCET vs. E_{cell} (MN) values. **d** Extended inset plot of (**c**) for the elements on the right leg of the volcano plot. Reprinted with permission from Ref. [61]. Copyright © 2020, Elsevier Ltd

electrocatalyst surface to estimate the catalytic activity for the noxious HER and the expected NRR [46]. To date, a large amount of work has concentrated on designing electrocatalysts to perform in aqueous electrolytes. Nonaqueous electrocatalysts, mostly gas diffusion electrodes, are made of Cu electrodes, stainless steel cloth, Mo foil, bare carbon cloth, and Au-coated carbon fibrous paper (Au/CP) [40, 43, 65-67]. They primarily target the adsorption of N_2, and the absence of protons in the electrolyte facilitates increased ammonia yield and higher FE. However, because of the unreliable, non-eco-friendly nature of nonaqueous systems, aqueous-based ammonia production techniques have gained increased attention.

3.2 Noble Metal-Based Catalysts

Various electrocatalysts have been reported for the NRR, including noble metal-based electrocatalysts, such as Pt [68], Pd [69], Au [70], Ru [71], and Rh [72]. Noble-metal SAC electrocatalysts exhibit excellent NRR activity with high NH_3 yield and considerable faradaic efficiency (FE), but they are susceptible to corrosion, and their lack of availability is also a detriment to efficient catalysis [73, 74]. Researchers have utilized noble metals to their fullest potential via strategies that enhance accessibility to metal active sites. Strategies such as designing a firm substrate for metal loadings, doping noble metals with transition metals, single-atom catalysts (SACs) and phase interface structures are followed to minimize the catalyst loading and extract the highest performance from the limited metal availability. To utilize noble metal atoms effectively, Yu et al. [75] adopted the SAC method. They developed a mesoporous Rh film with B- and S-doping on Ni foam (B, S-mRh/NF) to show the efficient NRR catalytic activity of noble metals and the effective utilization of scarce metals. B- and S-doping greatly enhances the catalytic activity by tuning the electronic density of Rh, which increases the N_2 adsorption ability, and S-doping maintains the selective hydrogenation of N_2 to NH_3. The synergistic effects of the noble metal with the heteroatoms for a selective function of the electrochemical NRR and an effective choice of a substrate directly influence the electrocatalytic activity.

Another strategy for the effective use of noble metal catalysts is through alloy engineering of either two noble metal atoms or a transition metal and a noble metal atom (Fig. 7b) [76]. On the basis of the alloy structures, Zhao et al. designed a bimetallic nanoalloy (NA) made of Ru and Rh, forming an fcc crystal lattice (Rh_xRu_{1-x} NA) [7]. The coupled effects of the Rh-Ru metal atoms induce electronic interactions between metals and the substrate with an ammonia yield of 57.75 μg h^{-1} mg_{cat}^{-1} and an FE of approximately 3.39%.

The interfacial activity of noble metals with modified transition metal substrates exhibits considerable NRR

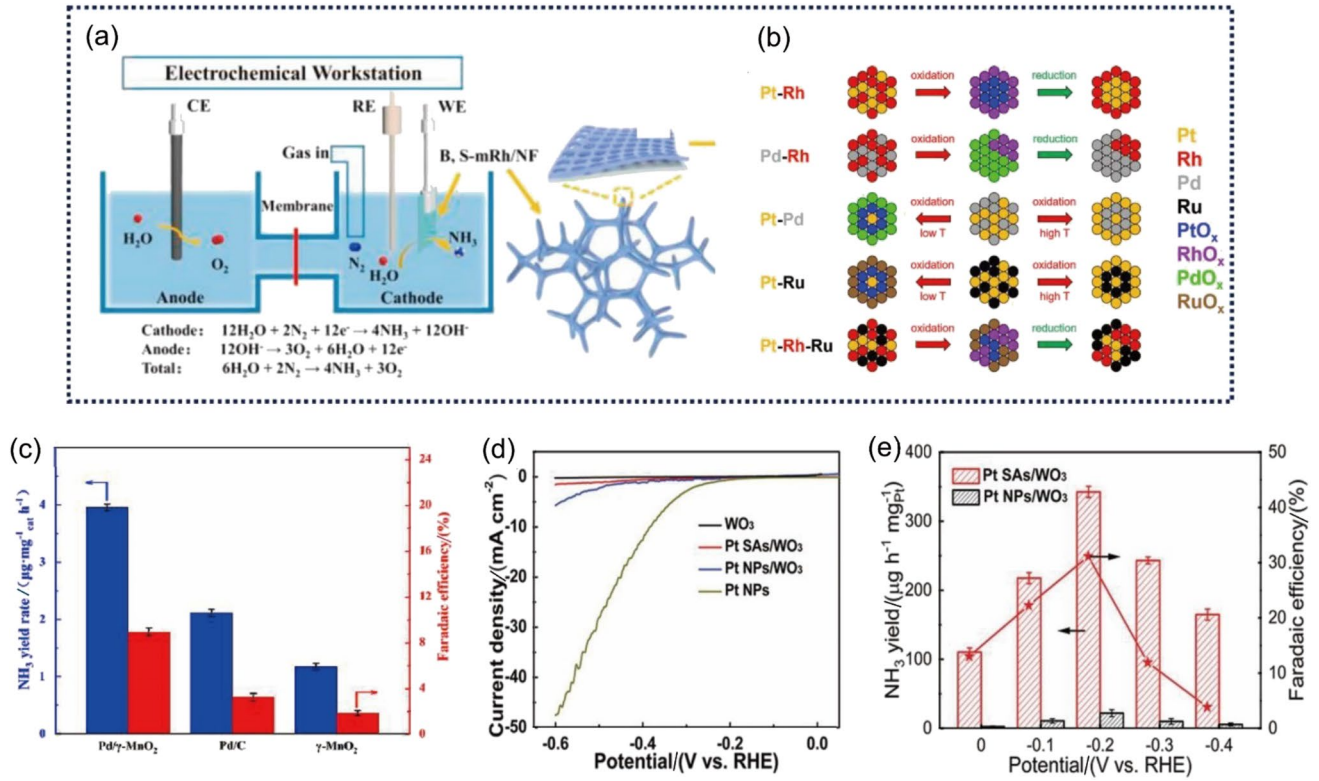

Fig. 7 **a** Schematic of the electrochemical cell with BS-mRh/NF as the cathode. Reprinted with permission from Ref. [75]. Copyright © 2021, Elsevier Ltd. **b** General strategies for alloy engineering of two noble metals. **c** Comparison of the ammonia yields and FE of Pd/α-MnO_2, Pd/β-MnO_2 and Pd/γ-MnO_2. Reprinted with permission from Ref. [77]. Copyright © 2020, MDPI. **d** LSV curves for WO_3 and single atoms and nanoparticle Pt atoms on WO_3 and Pt nanoparticles, respectively, in an Ar-saturated 0.1 M K_2SO_4 (1 M = 1 mol L^{-1}) electrolyte. **e** Comparison of the ammonia yield and FE of Pt SA/WO_3 and Pt NP/WO_3 for various applied voltages in 0.1 M K_2SO_4. Reprinted with permission from Ref. [68]. Copyright © 2020, John Wiley & Sons, Inc

performance. Sun et al. [77] reported that the phase interface of Pd/γ-MnO_2 was active for nitrogen reduction to ammonia. Additionally, this study suggested an increased activity of the γ-MnO_2 substrate compared with the α-MnO_2 and β-MnO_2 substrates. This increased activity can be attributed to the combined planar and pyramidal oxygen atoms on the γ-MnO_2 substrate (Fig. 7c) [78]. The Mn atoms initially adsorb N_2 on the surface because of their strong N_2 adsorption ability. Pd atoms then protonate the adsorbed N_2 by the Grotthuss-like proton hopping mechanism. Thus, utilizing the individual properties of different phases can enhance ammonia production because of the modified interfacial properties. Although Pt is a state-of-the-art electrocatalyst for the HER, single Pt atoms have been effectively implanted on suitable substrates to improve NRR performance and suppress the HER. Hao et al. [68] deposited isolated Pt atoms on a WO_3 nanoplate (Pt SAs/WO_3) substrate, which suppressed the HER and improved the NRR activity to deliver higher ammonia yields and FE. The observed NRR performances reveal that the single-atom Pt catalysts (Pt SA/WO_3) exhibit better NRR activity than the nanoparticle Pt catalysts (Pt NP/WO_3), as shown in Fig. 7d, e. Thus, the single-atom catalyst strategy is a worthy candidate for expressing higher yield and FE by noble metal-based NRR electrocatalysts. Thus, the appropriate use of a noble metal and a better substrate choice can enhance the electrocatalytic activity of the metal loadings and the doped heteroatoms, and despite its availability and cost, it delivers outstanding activities.

3.3 Transition Metal-Based Catalysts

Although noble metals are efficient electrocatalysts for the electrochemical NRR, their lack of availability in the Earth's crust and their high cost are detrimental to the cost-efficient NRR process. Transition metals are available in abundance and facilitate active sites for N_2 adsorption with their partially filled d-orbitals [79]. Transition metal derivatives such as oxides [53], nitrides [80], carbides [81], dichalcogenides [82-84], bimetallic alloys [85, 86], MXenes, and MBenes [87, 88], as well as metal–organic frameworks (MOFs) [70] and single-atom catalysts [89], provide a platform for incorporating more accessible active sites, improved reaction

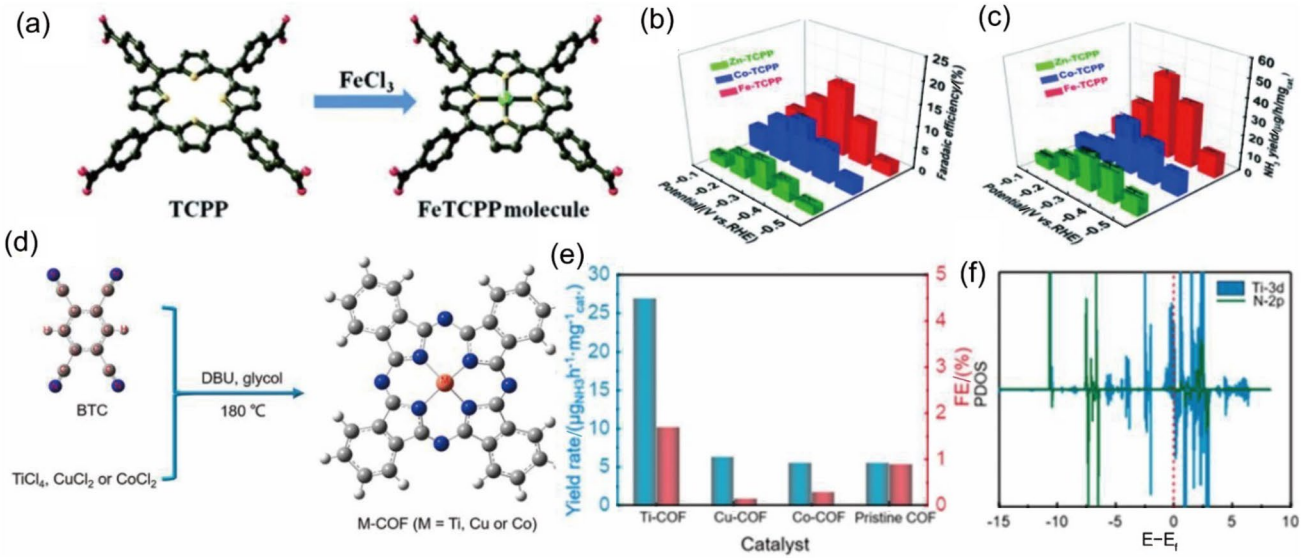

Fig. 8 **a** Schematic of the synthesis route of the Fe-TCPP MOF. **b** Comparison of the FEs of Fe-TCPP, Co-TCPP, and Zn-TCPP. **c** Comparison of the ammonia yields of Fe-TCPP, Co-TCPP, and Zn-TCPP. Reprinted with permission from Ref. [90]. Copyright © 2011, The Royal Society of Chemistry. **d** Illustration of the synthesis scheme of COF_{BTC}. **e** Comparison of the ammonia yields and FEs of Ti-COF, Cu-COF, Co-COF, and pristine COF. **f** PDOS after N_2 adsorption for Ti(3d) and $*N_2$ (2p) of Ti-COF. Reprinted with permission from Ref. [91]. Copyright © 2022, American Chemical Society

kinetics, selectivity for the NRR, and stability. Transition metal-based electrocatalysts adopt various design strategies and morphologies that substantially enhance the NRR.

3.3.1 Metal–Organic Framework Electrocatalysts

Researchers have been obsessed with designing an efficient structure capable of providing large pore sizes for mass transport, as well as an effective conducting path for electrons. In this context, Cong and his group synthesized porphyrin-based single-site MOFs with Fe (Fe-TCPP) nodal sites as the catalytic centres for artificial N_2 fixation (Fig. 8a) [90]. Among the Fe-, Co, and Zn-based TCPP MOFs, the Fe-TCPP MOFs play an important role in N_2 adsorption and conversion. The high adsorption activity of Fe-TCPP can be attributed to the longer Wiberg bond index (WBI), which can more readily activate N_2 than Co-TCPP and Zn-TCPP. The Fe-TCPP electrocatalyst exhibits an FE of nearly 16.23% and a maximum ammonia yield of approximately 44.77 μg h^{-1} mg^{-1}, as shown in Fig. 8b, c, respectively. This electrocatalyst exhibits a higher FE, which indicates selectivity towards the NRR over the HER on the Fe–N–C active sites.

Based on the literature suggestions, NRR mediation along with HER suppression can be effective over metal-coordinated N centres (M-N_x) [34]. Jiang et al. [91] reported a pyrolysis-free template strategy for constructing a 2D M-covalent organic framework (COF) using benzene-1,2,4,5-tetracarbonitrile (BTC) and metal chlorides ($TiCl_4$, $CuCl_2$, $CoCl_2$) (Fig. 8d). The N atoms form a linker bond with the metal sites that exhibit increased N_2 adsorption, thereby suppressing the HER. The COF_{BTC} electrocatalysts exhibit an enhanced NRR performance with higher ammonia yields (Fig. 8e) and FE compared to other framework electrocatalysts.

The partial density of states (PDOS) of Ti-COF after N_2 adsorption show the overlapping orbitals of Ti(3d) and $*N_2$(2p), indicating increased antibonding states above the Fermi level facilitating the adsorption of N_2 (Fig. 8f). Although a handful of theoretical works implement a COF into electrocatalysts, experimental insights into the same structures are most expected. These structures can possibly meet the requirements of electrode materials for air-battery applications, as well as flexible, rechargeable battery applications [92, 93]. The prominent nonnoble metal-based electrocatalysts are derivatives of transition metal complexes. They are made to tune the intrinsic electronic properties, and they are planted onto a substrate that enhances the electronic conductivity of the electrocatalysts.

3.3.2 Single-Atom Electrocatalysts

Single-atom catalysts as metallic electrocatalysts offer an efficient design strategy for metal species that are well distinguished by their mononuclear active sites.

The SAC strategy is adopted to effectively utilize the metal species and increase the specific activity of the electrocatalyst. SACs anchored on substrates exhibit higher

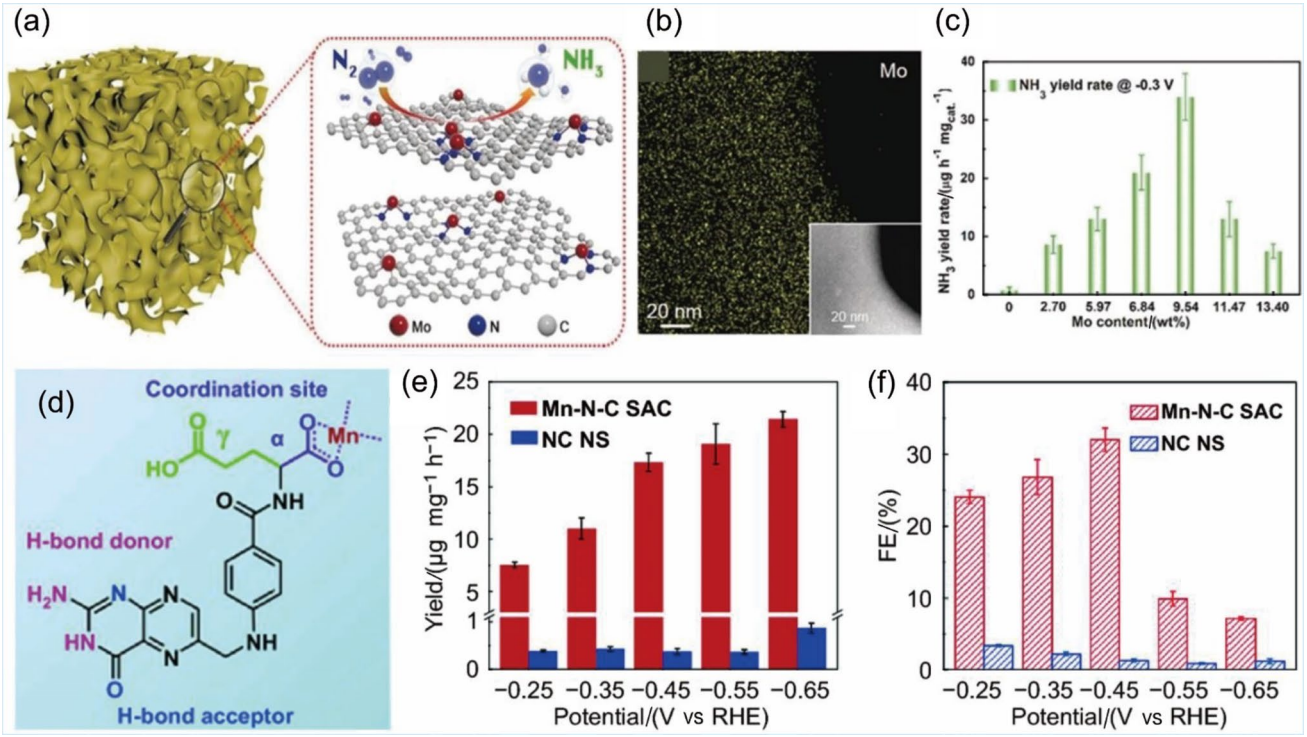

Fig. 9 **a** Illustration of SA-Mo/NPC and the respective atomic structure model. **b** EDS mapping of SA-Mo/NPC. **c** Ammonia yield for various Mo loading in SA-Mo/NPC Reprinted with permission from Ref. [94]. Copyright © 2019, John Wiley & Sons, Inc. **d** Scheme representing the active sites for N adsorption of the Mn–N–C SAC electrocatalyst. Comparison of the **e** ammonia yields and **f** faradaic efficiencies of the Mn–N–C single-atom catalyst and NC-nanosheets. Reprinted with permission from Ref. [95]. Copyright © 2021, Springer Nature Ltd

exposure to electrolytic ions, which enhance adsorption towards N_2. Similar to noble metal SACs, transition metals such as Mo [94], Mn [95], and Fe [96] were reported as SACs with mostly M–N–C coordinated sites, which expose more active sites for selective N_2 adsorption.

The M–N–C active sites can efficiently perform heterogeneous catalysis with their isolated single atoms dispersed along the substrate. For instance, Han et al. [94] reported single-atom catalysts (SACs) and nanoclusters (NCs) of Mo atoms embedded on nitrogen-doped porous carbon (SA-Mo/NPC) for the NRR (Fig. 9a-c). When Mo atoms form clusters, the activity is obvious, and their active site density is reduced compared to that of a single Mo atom. The improved activity of a SAC can be discerned through comparison with the NRR performance of its nanocluster counterpart. Additionally, the authors synthesized SA-Co/NPC, and their nanocluster assemblies exhibit superior activity for single-atom Co/NPC but not higher than SA-Mo/NPC.

Similarly, Wang et al. [95] developed a 2D Mn–N–C SAC via an acid self-assembly strategy that exposes Mn atoms for selective N_2 adsorption and higher active sites (Fig. 9d). The well-exposed Mn–N–C coordinated sites on the 2D matrix reveal a high ammonia yield of approximately 21.43 μg h^{-1} mg^{-1}_{cat} and an FE of nearly 32.02% (Fig. 9 e, f). The Mn–N–C coordinated sites show excellent selectivity towards the NRR over the HER, which contributes to the higher ammonia yield and FE. Therefore, studies have concluded the superior activity of SACs in the NRR. Thus, SACs are bound to exhibit excellent NRR electrocatalytic activity with their large active site density and maximized metal utilization [97].

3.3.3 Transition Metal Oxides

Transition metal oxides have ruled the electrocatalytic field for decades and have proven their superiority in almost all redox reactions owing to their defect modulation ability and electron affinity behaviour, which actively tunes the intrinsic electronic configuration of the electrocatalysts [98, 99]. Xiao et al. [100] synthesized nanoporous NiO/MoO_3 by incorporating abundant oxygen vacancies (V_O) into the catalyst for efficient NRR behaviour (Fig. 10a). These bimetal sites with V_O tune the electronic structure for the π-back-donation process, which reduces the hydrogenation character and promotes the NRR (Fig. 10b). This result is due to the improved conductivity, active N_2 adsorption and intrinsic performance of the metals. Thus, incorporating oxygen

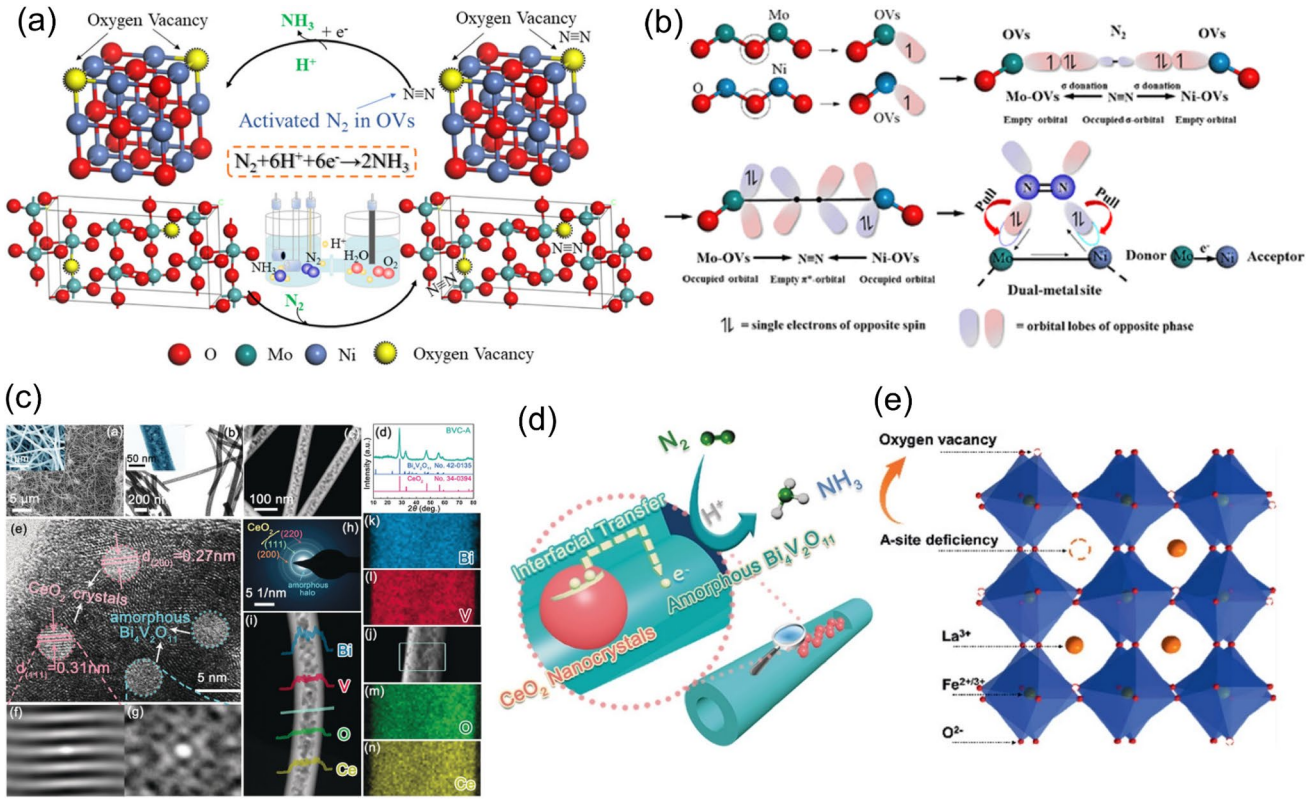

Fig. 10 **a** Scheme representing the NRR performance in oxygen-vacant nanoporous NiO/MoO_3. **b** Illustration of the donor–acceptor mechanism for N_2 adsorption on the nanoporous NiO/MoO_3 electrocatalyst. Reprinted with permission from Ref. [100]. Copyright © 2021, American Chemical Society **c** Material characterization studies of the $Bi_4V_2O_{11}$-CeO_2 interface and elemental distribution. **d** Scheme representing the interface of $Bi_4V_2O_{11}$-CeO_2 for the NRR and the electron transfer between $Bi_4V_2O_{11}$ and CeO_2 structures. Reprinted with permission from Ref. [103]. Copyright © 2018, John Wiley & Sons, Inc. **e** Illustration of the oxygen vacant sites and anion vacancies of $La_xFeO_{3-\delta}$ perovskite oxides, which are active for the NRR. Reprinted with permission from Ref. [104]. Copyright © 2021, John Wiley & Sons, Inc

vacancies into bimetallic complexes can improve the overall NRR performance.

Similarly, Wen et al. [101] synthesized oxygen vacancy-rich Zn-doped Co_3O_4 electrocatalysts derived from ZIF 67 and ZIF 8. The rich oxygen vacancies and the synergistic effects of Zn-doped Co_3O_4 reveal a higher NRR performance compared to pristine Co_3O_4. Additionally, considering the morphology engineering strategy, metal oxides can be incorporated into nanosheets [102], spinel structures [53], etc., to use the active sites. Apart from most crystalline and ordered materials that facilitate the NRR, Yu et al. [103] synthesized an amorphous–crystalline hybrid electrocatalyst that intrinsically includes large oxygen vacancies that act as active sites for nitrogen adsorption. The $Bi_4V_2O_{11}$-CeO_2 catalyst in the amorphous phase (BVC-A) has a high oxygen content compared to the crystalline counterpart (BVC-C). TEM images and the XRD patterns of BVC-A revealed a definite nanorod morphology with uniform distributions and the presence of partially amorphous structures, respectively (Fig. 10c). The HRTEM and SAED analyses showed the coexistence of the amorphous $Bi_4V_2O_{11}$ phase and the crystalline CeO_2 phase in the BVC-A samples. Because of the high valence of the Bi^{5+} defect, V_O and V^{4+} proceed through the π-back-donation process. This activity has not been observed in the crystalline form (BVC-C) and pristine (BVC) conditions. The improved activity indicates that the amorphous form of BVC facilitates more oxygen vacancies, which tunes the band alignment that increases the number of active sites in the material and leads to superior electron conductivity (Fig. 10d).

In addition, Chu et al. [104] reported deficiency-induced oxygen vacancies on $La_xFeO_{3-\delta}$ perovskite oxides with tunable oxygen vacancies, which are proportional to the deficiencies at the La site (Fig. 10e). For L_xF ($x = 1$, 0.95, 0.9), $L_{0.9}F$ exhibits improved NRR activities due to the La deficiency and oxygen vacancy. Additionally, $L_{0.9}F$ exhibited lower electronic resistance (R_{ct}), and the La d-orbital strongly adsorbed N_2 and the intermediates. $L_{0.9}F$ eventually exhibits an NH_3 yield rate of 22.1 μg h^{-1} mg_{cat}^{-1} and an FE of 25.6%, which are very high compared to pristine LF.

The $L_{0.9}F$ active sites show limited selectivity towards H^+ adsorption, which is attributed to the high ammonia yield and FE. Thus, enabling stable structures and increased oxygen vacancies enhances the rate of nitrogen adsorption and the protonation of the adsorbed N_2 molecule, which eventually produces more ammonia with better faradaic efficiency. Therefore, oxygen-vacant electrocatalysts are actively imparted into Zn-N_2 battery applications, where a stable architecture combined with a large active site density could be of actual use in the system [98, 105, 106].

3.3.4 Transition Metal Nitrides

The transition metal nitride, on the other hand, behaves as the unique structure of all the electrocatalysts, in which the catalyst itself participates in the reduction reaction via the MvK mechanism [87, 107]. Nitride surfaces guarantee their inactivity for HER in the MvK mechanism, yet using the TMN catalyst has a few drawbacks [108]. First, the experimental proof for NRR is laborious because the nitrogen atoms from the catalyst surface are reduced to form ammonia, where a quantitative study of the $^{15}NH_3$ formation is mandatory using the $^{15}N_2$ feeding gas. Second, the long-term stability of the nitride catalyst, which can be compromised by surface vacancy replenishment with feeding N_2 gas, occurs only when N vacancies are stable at the surface [46, 79].

Du et al. [109] observed the degradation of tetragonal Nb_4N_5, which produces ammonia simultaneously by reducing the surface nitrogen atoms, an irreversible process. However, the author proves the presence of small amounts of nitrogen in the electrocatalyst and the contribution of the contaminants in the previously reported VN electrocatalysts that show ammonia production with low turnover numbers (Fig. 11a) [110, 111].

In addition, Lv et al. [49] reported a VN nanodot supported on an ultrathin N, S codoped carbon substrate pyrolyzed at 900 °C (VN@NSC), which follows an MvK mechanism that exhibits high activity and offers pH independence for NRR (Fig. 11b). The real-time NRR mechanisms were observed by using in situ FTIR and revealed that the carbon substrate could also participate in NRR by an associative alternating pathway. However, ^1H NMR shows both the doublet ($^{15}NH_4^+$) and triplet peaks ($^{14}NH_4^+$) for the $^{15}N_2$ feeding gas, and the catalyst exhibits cycling stability for over six consecutive cycles for 24 h. The detection of the doublet and triplet peaks of NH_4^+ indicates the presence of surface-N protonated ammonia and the adsorbed N_2 transformed ammonia.

However, in contrast to the degradation of the electrocatalyst by the MvK mechanism, few reports have suggested the outstanding NRR performance of the electrocatalyst. Moreover, certain M-N_x coordinated active sites reveal lower selectivity for H^+ adsorption, resulting in a high FE and maximum ammonia yield. Therefore, fabricating metal nitrides is highly anticipated to achieve higher ammonia yields and suppressed HER. Consequently, Jin et al. [80] reported a nitrogen vacancy-rich W_2N_3 (NV-W_2N_3) electrocatalyst, which shows enhanced ammonia production performance by the associative distal pathway. Figure 11c reveals the lower limiting potential for NRR, resulting in a high ammonia yield and FE. In addition, the charge density difference calculations reveal the electronic structures of the NV-W_2N_3 electrocatalyst, which shows that the active adsorption sites of the electrocatalyst are electron-deficient nitrogen vacant sites (Fig. 11d). The UV−vis spectroscopic studies over the control samples exhibit no absorption peaks other than for the N_2-saturated electrolyte (Fig. 11e). The theoretical studies and the ^1H NMR results clearly explain the stability of the electrocatalyst over ammonia production by the electrocatalytic process and not by surface reconstruction (Fig. 11f). In addition, Yesudoss et al. [112] reported the one-step synthesis of γ-Mo_2N anchored on 2D h-BN sheets (γ-Mo_2N/h-BN), which exhibited a considerable FE of approximately 61.5% (Fig. 11g). The improved activity can be attributed to the interfacial engineering of the cubic γ-Mo_2N on the hexagonal BN sheets incorporated with numerous nitrogen vacancies (Fig. 11h). Thus, tuning the electronic structures of the electrocatalyst by vacancy engineering can modify the electrocatalytic properties that improve the NRR and effectively suppress the HER [113].

3.3.5 Transition Metal Carbides

The design for electrocatalysts is generally based on altering the d-bands of the electrocatalytic materials to increase the adsorption behaviour of the analyte [114-116]. Thus, altering the d-bands increases the density of states (DOS) near the Fermi level, which enhances electrocatalytic activities, as in noble metals [114]. Interestingly, transition metal carbides (TMCs) are observed to have similar electronic structures and electrocatalytic activities as noble metal catalysts [115]. Hence, TMCs are engineered as efficient electrocatalysts for NRR. As a result, Zhang et al. [81] reported vanadium carbides (V_8C_7) as NRR electrocatalysts, which reveal anionic vacancies as active sites for efficient N_2 adsorption (Fig. 12a). The tuned electronic structure due to the carbide vacancies enhanced the N_2 reduction performance, with a relatively high ammonia yield of 23.2 μg h^{-1} mg^{-1} and an FE of 18.3% (Fig. 12b, c).

Similarly, Ramaiyan et al. [117] prepared origami-like molybdenum carbides (Mo_2C) as NRR electrocatalysts. The catalyst revealed a low FE and a considerable ammonia yield due to the surface oxidation of the Mo_2C electrocatalysts. However, Mo_2C exhibited robust stability for 50 h of continuous electrolysis operation with negligible change. Hence,

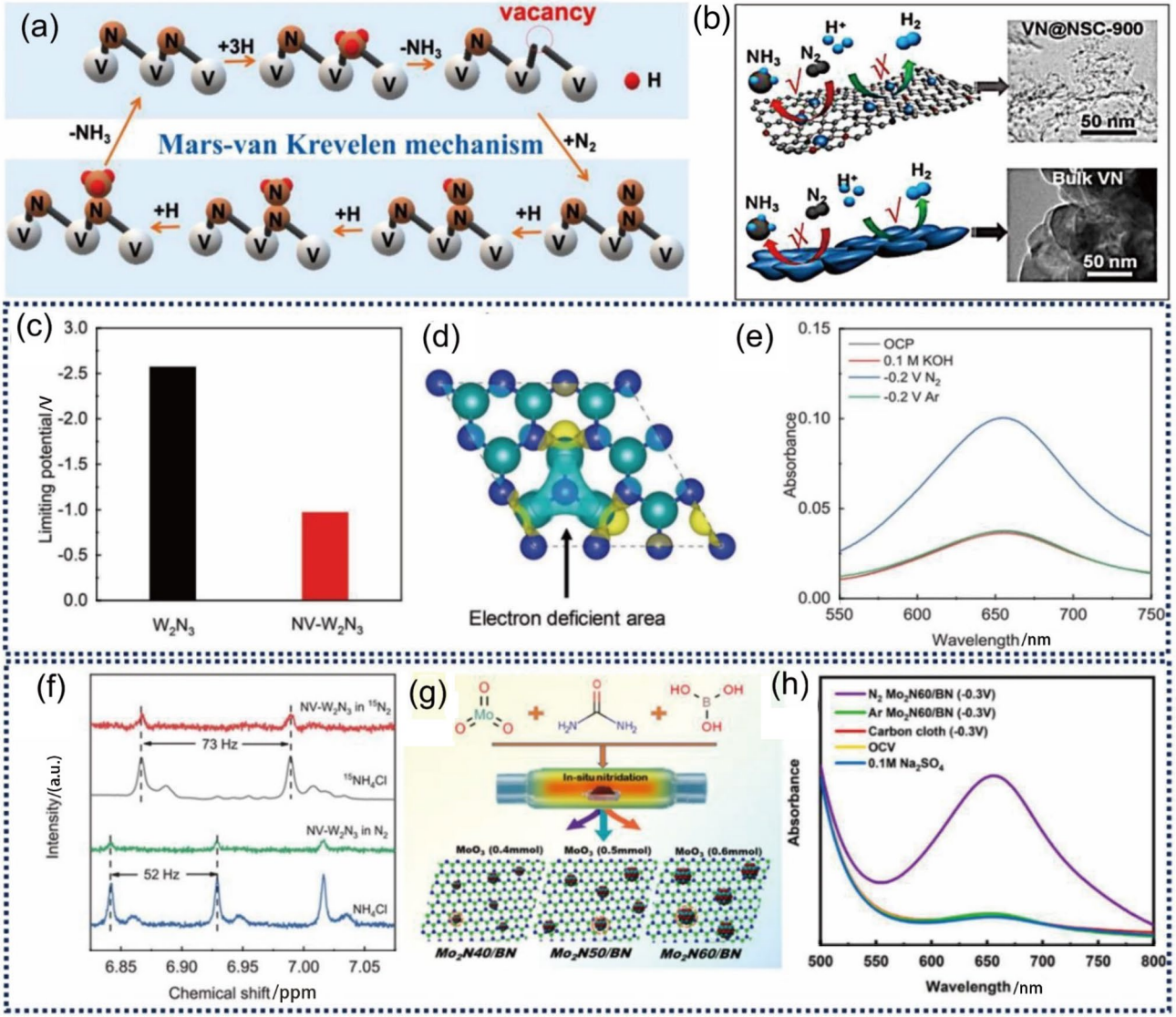

Fig. 11 **a** Schematic of the MvK mechanism on the VN surfaces. **b** Representation of the NRR activity on the surfaces of bulk VN and VN@NSC. Reprinted with permission from Ref. [49]. Copyright © 2021, Elsevier Ltd. **c** Comparison of the NRR activity of the nitrogen vacancy in the W_2N_3 electrocatalyst. **d** Charge density difference profiles for the NV-W_2N_3 electrocatalyst. **e** UV absorption profiles over a controlled environment for the NV-W_2N_3 electrocatalyst. **f** ^{1}H NMR results of NV-W_2N_3-catalysed ammonia production under $^{14}N_2$ and $^{15}N_2$ feeding gases. Reprinted with permission from Ref. [80]. Copyright © 2019, John Wiley & Sons, Inc. **g** Scheme representing the one-step synthesis route for γ-Mo_2N/h-BN sheets. **h** UV absorption profiles for γ-Mo_2N/h-BN control samples. Reprinted with permission from Ref. [112]. Copyright © 2021, Elsevier Ltd

the carbides were reported to exhibit enhanced NRR performances due to the tunable electronic structures and show better electrochemical stability. Interestingly, several reports have used Fe_3C@C [118], Mo_2C/C nanodots [119], and TiC/C [120] as structurally modified NRR electrocatalysts to achieve better NRR performances with robust stability.

3.3.6 Transition Metal Dichalcogenides

Transition metal dichalcogenides (TMDCs), such as sulfides, selenides, and tellurides, have been explored as efficient electrocatalysts for NRR because of their unique electronic structures and high specific surface areas [121]. Several strategies, such as defect engineering and morphological engineering, were followed to increase NRR activity [83, 122]. Transition metal sulfides are the most studied candidates for dichalcogenide materials, which show tunable

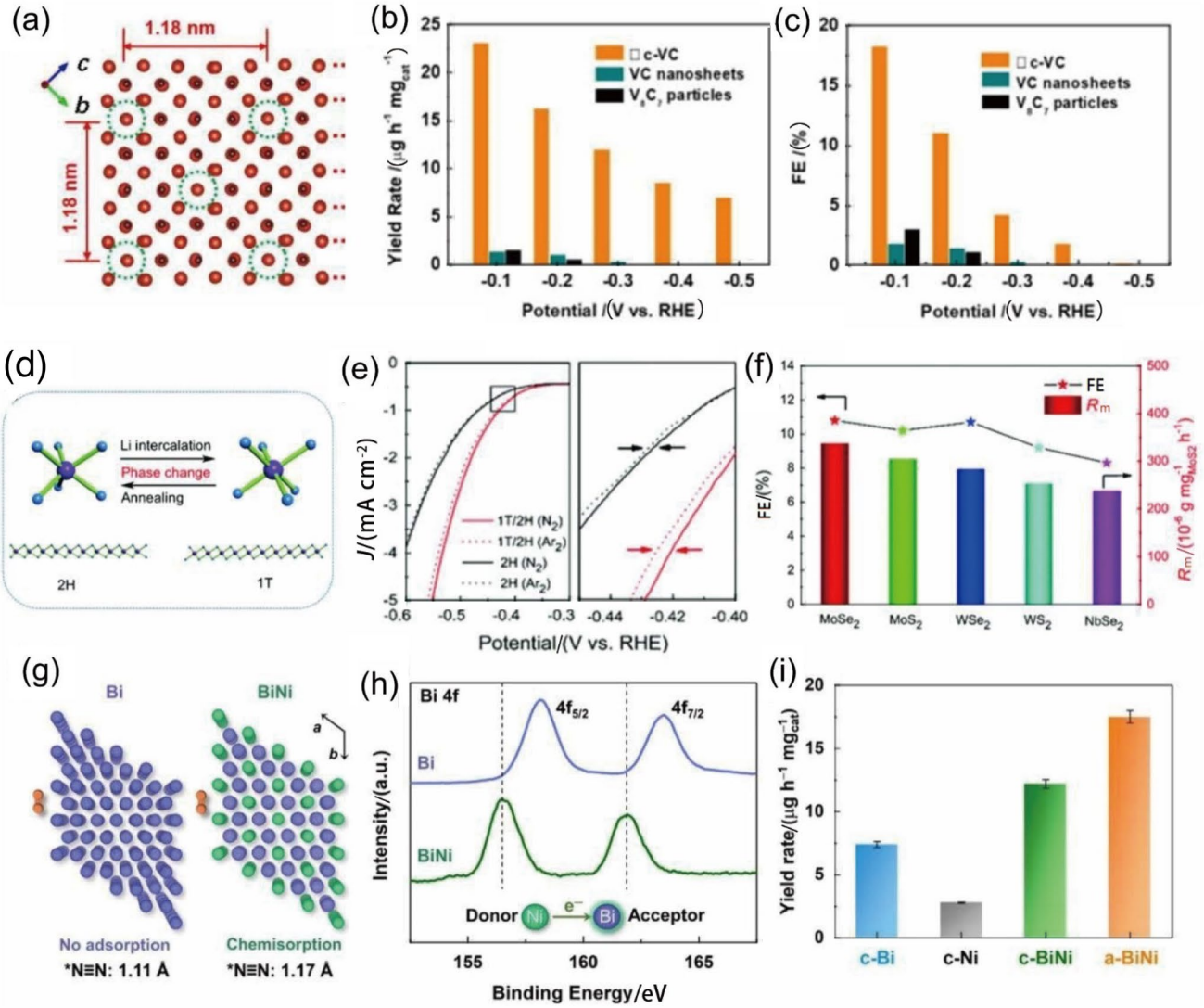

Fig. 12 **a** Illustration of the carbide vacancies in the V_8C_7 electrocatalyst. **b** Ammonia yield and **c** FE of the V_8C_7 electrocatalysts. Reprinted with permission from Ref. [81]. Copyright © 2020, Elsevier Ltd. **d** Scheme representing the phase change of $MoSe_2$ from 2H to 1T. **e** LSV polarization curves of the $MoSe_2$ electrocatalyst under N_2 and Ar saturation. **f** Comparison of the FE and ammonia yields of various prepared electrocatalysts. Reprinted with permission from Ref. [83]. Copyright © 2020, The Royal Society of Chemistry. **g** Illustration of the Bi-Ni bimetallic alloys for N_2 chemisorption. **h** Bi 4f XPS spectra (the inset: scheme representing ligand effects between Bi and Ni). **i** Comparison of the ammonia yields of the Bi-Ni prepared electrocatalysts. Reprinted with permission from Ref. [125]. Copyright © 2021, John Wiley & Sons, Inc

electronic structures and active sites for improved NRR performance [122]. In addition to sulfides, selenides and tellurides have also been studied as low-cost NRR electrocatalysts that provide considerable NRR performance [121]. As a first report for TMDC as an NRR electrocatalyst, MoS_2 was analysed, which revealed a low FE and ammonia yield due to its inactive edge and basal planes [82]. Notably, the 2D TMDC exhibits poor electrocatalytic performance due to the inactive basal planes and edge sites [122]. Hence, Zhao et al. [123] designed VS_2 electrocatalysts by shearing the sulfur edges by a defect engineering strategy, which increased the N_2 adsorption towards V metal sites. This strategy has modified the electronic structure, which enhances the DOS near the Fermi level of VS_2, improving ammonia productivity. Morphology engineering strategies have an important role in enhancing the active sites and tuning the active phase for redox reactions in an electrocatalyst. For instance, Zhang et al. [83] reported $MoSe_2$ quantum dots with an effective ultrathin morphology to achieve better NRR performance after a phase change from the 2H to 1T phase (Fig. 12d). The 1T-$MoSe_2$ electrocatalyst exhibits better N_2 reduction performance than the 2H phase and other prepared electrocatalysts (Fig. 12e, f). The ultrasmall layers of $MoSe_2$ QDs exhibit higher electrocatalytic active sites

with abundant defects and edges, which tune the electronic structure for selective N_2 adsorption. Therefore, based on previous reports and studies, TMDCs can be effectively tuned by morphology, defect, and dopant engineering strategies to alter their electronic structure and achieve higher NRR performances.

3.3.7 Heterogeneous Alloy Electrocatalysts

Recently, heterogeneous alloys have been reported to achieve higher NRR performances due to the synergistic activity of transition metals. Heterogeneous alloys can enhance electrocatalytic activities by tailoring structural, compositional, and electronic effects [124]. Recently, Fang et al. [125] reported that amorphous Bi-Ni bimetallic alloys promote N_2 adsorption and activation by synergistic effects between p-block Bi and d-block Ni elements (Fig. 12g). The ligand effect between Ni and Bi imposes lower limiting potentials for N_2 chemisorption and ammonia formation (Fig. 12h). Moreover, Bi-Ni bimetallic alloys in the amorphous phase exhibit a relatively high ammonia yield rate and high surface area for electrocatalytic reactions compared to the other prepared electrocatalysts (Fig. 12i). Similarly, Li et al. [126] reported Co_3Fe-MOFs as efficient NRR electrocatalysts because of the coupling effects of Fe and Co atoms. In addition, bimetallic alloys were also supported on N-doped carbon substrates, which enhanced the NRR electrocatalytic activity and conductivity [86]. Therefore, heterogeneous alloys with tunable structural, compositional, and electronic properties are inspired as efficient NRR electrocatalysts.

3.3.8 Main Group Metal-Based Electrocatalysts

Other than the abovementioned electrocatalysts, researchers have explored the main group metals that hold potential abilities to suppress the HER and enhance NRR performance. The main group metals, viz., s block (Li, K) and p block (Al, Ga, Sn, In, Bi, Sb)-based electrocatalysts, are effective in suppressing the HER due to the limited availability of electrons in their valence orbitals [127], unlike transition metals. For instance, Sebastian et al. [128] reported $K_3Ti_8O_{17}$ nanorods as NRR electrocatalysts, which achieved a higher ammonia yield and considerable FE (Fig. 13a). The repulsive effect of K^+ ions on H^+ ions reduces proton adsorption over the electrocatalyst, which suppresses the HER. Similar studies involving the Li incorporation strategy in electrocatalysts have shown relatively higher ammonia selectivity over the HER [129, 130].

Among the p-block elements, Bi exhibits poor HER performance, which reveals the efficient electrocatalytic property of Bi-based NRR electrocatalysts [131]. Li et al. [132] fabricated 2D mosaic Bi nanosheets with a high surface area and optimum electrocatalytic activities (Fig. 13b). The reduced Bi-Bi interlayer distance and the electronic structure of 2D mosaic nanosheets along with the delocalized electrons in the p-orbital of Bi atoms near the edge sites impose abundant active sites for N_2 adsorption and activation. The 2D Bi-NS reveal a high ammonia yield and FE compared to the Bi nanoparticles (Fig. 13c).

In addition, a comparison study of the metal tellurides $MeTe_x$ (Me = Sb, Co, Cd, Bi) revealed $SbTe_3$ hexagonal plates as efficient NRR electrocatalysts that exhibit a high ammonia yield rate of approximately 13.8 μg h^{-1} cm^{-2} and 27.7% FE [84]. The higher NRR performance can be ascribed to the selectivity of the electrocatalyst for N_2 adsorption over HER and a higher DOS near the Fermi level. Theoretical studies reveal lower H binding energies for Ga, Sn, In, and Bi, which can be potential elements for NRR electrocatalysts [61]. Several main group element-based electrocatalysts have been widely studied, revealing promising ammonia yields and FEs by inhibiting the inimical HER.

3.3.9 MXenes and MBenes

On the other hand, 2D MXenes are widely studied as a part of transition metal nitrides and carbides, as their structure is represented as $M_{n+1}X_nT_x$ ($n = 1, 2, 3$). M shows the $n+1$ layers of transition metals, X represents the n-interleaved carbon (C) or nitrogen (N) elements with transition metals, and T_x represents the terminal molecules on the MX surface (O, OH, F and/or Cl) that are bonded to other M layers [133]. Wei et al. [134] synthesized Ti_3C_2 MXene nanosheets (Ti_3C_2-MNS) and nanoribbons (Ti_3C_2-MNR) and observed a skyrocketing ammonia yield for Ti_3C_2-MNR, which is 5 times that of Ti_3C_2-MNS (Fig. 13d). The FE was also observed to increase by 2%, and a stable current density was observed for all the samples. Thus, a structural transformation from a 2D MXene to a 3D MXene has been proven to increase the catalytic active sites that eventually improve the NRR. In addition, Kong et al. [135] reported a sandwich-like structure that separates the $Ti_3C_3T_x$ layers and forms a hybrid heterostructure material for NRR. Moreover, the heterostructure formation of MXene with MnO_2 (MnO_2-$Ti_3C_2T_x$) is found to exhibit enhanced ammonia yield performance. With Mn being the adsorption site for N_2 adsorption and MXenes being the electron conductive region, ammonia production can be substantially increased. The NRR activity of the MnO_2-$Ti_3C_2T_x$ hybrid structures can be verified by control experiments (Fig. 13e) and deformed charge density plots (Fig. 13f).

MBenes are the boride forms of MXenes that possess the same monolayer-heterolayer structures that form stable architectures with high thermal and electrical conductivities. They are already used in the field of energy storage as anodes for Li/Na ions [136]. However, experimental methods for MBenes have yet to be explored in the case of NRR.

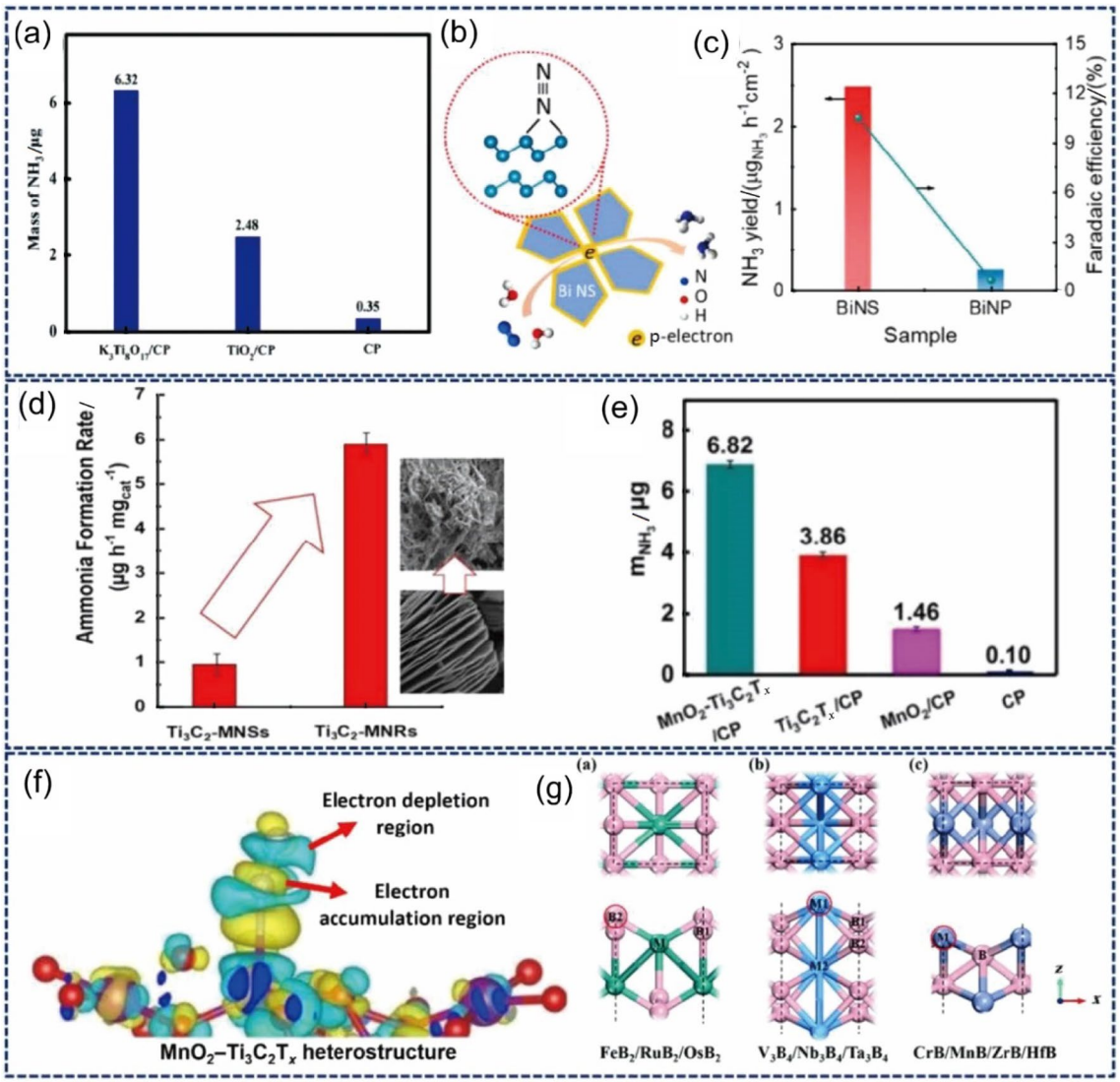

Fig. 13 **a** Comparison of the ammonia yields of prepared $K_3Ti_8O_{17}$ electrocatalysts. Reprinted with permission from Ref. [128]. Copyright © 2022, The Royal Society of Chemistry. **b** Schematic of N_2 adsorption over 2D mosaic Bi NS electrocatalysts. **c** Comparison of the ammonia yield and FE of the prepared Bi NS and Bi NP electrocatalysts. Reprinted with permission from Ref. [132]. Copyright © 2019, American Chemical Society. **d** Comparison of the ammonia production of Ti_3C_2-MNS and Ti_3C_2-MNR. Reprinted with permission from Ref. [134]. Copyright © 2020, John Wiley & Sons, Inc. **e** Comparison of the ammonia yields of the MnO_2-supported $Ti_3C_2T_x$ and pristine samples. **f** Distributed charge density diagram of the MnO_2-$Ti_3C_2T_x$ heterostructure adsorbing a N_2 molecule. Reprinted with permission from Ref. [135]. Copyright © 2019, The Royal Society of Chemistry. **g** Schematic of the MBene structures over various transition metals for the electrocatalytic NRR. Reprinted with permission from Ref. [137]. Copyright © 2020, The Royal Society of Chemistry

Theoretical studies have been satisfying for the application of NRR, where Yang et al. [137] considered 10 compositions of MBenes and computed to report the excellent stability of the catalysts in aqueous solutions that show high NRR preference over the inimical HER (Fig. 13 g). Fu et al. [138] studied MoAlB as an NRR electrocatalyst, which revealed a high selectivity for N_2 adsorption due to the stronger bonding interactions between the p-orbitals of Al and nitrogen absorbers. The partially occupied p-orbitals, the ability of the surface B sites to adapt electrons and the N_2 adsorption properties make MBenes a viable choice for the NRR electrocatalyst. Thus, TMB can be considered an efficient option for NRR electrolysis that can be modulated for intrinsic electronic properties and stable structure formations that can be used in energy storage and conversion applications.

3.3.10 Other Transition Metal-Based Electrocatalysts

Other transition metal-derived NRR electrocatalysts include transition metal fluorides and transition metal phosphides.

Transition metal fluorides (TMFs) have been studied as electrocatalysts that are observed to alter the d-bands of transition metals to achieve better performances in specified applications [139]. Therefore, Li et al. [140] studied lanthanum fluoride (LaF_3) as an NRR electrocatalyst that inhibits the HER compared to La_2O_3. The 2D platelet-like structures reveal a high surface area for N_2 adsorption and activation, with a high ammonia yield of approximately 55.9 μg h^{-1} mg_{cat}^{-1} in 0.5 M $LiClO_4$ with a considerable 16% FE. The fluorides are studied to express excellent durability and cycling performances. In addition, transition metal phosphides (TMP) are also studied as electrocatalysts for NRR because of their high conductivity, controllable elements, and unique physicochemical properties. P bonding to transition metals regulates the internal electronic structure of the active sites to improve NRR catalytic activity [141]. Guo et al. [142] studied cobalt phosphide hollow nanocages (CoP HNC) as NRR electrocatalysts. The CoP HNC exhibits a lower kinetic barrier for the HER but shows higher selectivity for ammonia, inhibiting hydrazine formation.

3.4 Metal-Free Electrocatalysts

The design of electrocatalysts based on metal-free materials has reduced the production cost of electrocatalysts, supplemented tunable pore sizes, and enhanced surface adsorption properties. Metal-free electrocatalysts increase selectivity for NRR [143], improve mass transport [144] and electronic conductivity [145, 146]. Several design strategies, including heteroatom dopant engineering and vacancy engineering methods, and utilizing various metal-free materials, such as graphitic-carbon nitride (g-C_3N_4), graphene, boron nitride (BN), black phosphorous (BP), and organic frameworks (MOF/COFs), have been successful in achieving efficient NRR electrocatalysts. Dopant engineering involves the doping of heteroatoms (B, N, S, P) into carbonaceous materials, which modulate the electronic structures of the materials to achieve higher NRR performances [147-150]. Boron-based electrocatalysts have been found to exhibit enhanced NRR performance due to their electron deficiency nature and inactivity towards the HER [151].

As an example of a doping strategy, Yu et al. [148] reported boron-doped graphene (BC_3) as an NRR electrocatalyst that exhibits excellent NRR properties at the B site, enhancing the N_2 binding capability (Fig. 14a). The HOMO–LUMO plots and the charge density difference diagrams reveal the charge-deficient regions for possible N adsorption sites (Fig. 14b, c). Hence, this work highlights the potential ability of the boron-doped metal-free matrix for efficient NRR. The carbon framework provides structural stability and enhanced electron conductivity, as well as mass transport, which provides the added advantage of choosing a framework for electrocatalytic applications. Similarly, Song et al. [149] engineered N, P-codoped MOF-5 carbon (NP-C-MOF-5), exhibiting an ammonia yield of nearly 1.08 μg h^{-1} mg_{cat}^{-1} with considerable evolution of N_2H_4. Likewise, Tian et al. [150] reported N, S codoped graphene (NSG) as a durable NRR electrocatalyst that exhibited a high ammonia yield of nearly 7.7 μg h^{-1} mg^{-1} with a high selectivity towards NRR. Heteroatom doping in carbonaceous materials has been studied to generate charge distributions in the carbon matrix that enhance electron conductivity [146], tune the selectivity towards NRR [152], promote N_2 adsorption [153], and create more defective sites for effective NRR performance.

As metal-free noncarbonaceous NRR electrocatalysts, boron nitride (BN) has been anticipated to achieve better selectivity towards NRR, and its layered structure provides highly accessible active sites. For instance, Zhao et al. [154] designed mesoporous boron nitride (MBN) electrocatalysts that show a large surface area and highly accessible active sites due to their mesoporous structure. Compared to the bulk BN, a high ammonia yield can be observed in the MBN electrocatalysts. In addition, black phosphorous has also been observed to exhibit excellent NRR activity due to its anisotropic structure and abundant edge sites that enhance ammonia productivity. Zhang et al. [155] reported exfoliated black phosphorous (FL-BP) nanosheets that were observed to produce high ammonia yields and FE on the zigzag edges of FL-BP (Fig. 14e, f).

Similar to MOFs, Liu et al. [145] reported a facile synthesis procedure for 2D boron-rich COF materials that are electrochemically excited (Eex-COF/NC) to exhibit better NRR performances and suppress HER over the B-active sites (Fig. 14g, h). The COF structures linked by boroxine rings (B_3O_3), boronate esters (C_2O_2B), amide and imide connecting structures are addressed to be Lewis acid sites that can efficiently adsorb a weak Lewis base, such as the N_2 molecule. Importantly, these framework structures exhibit poor electron conductivities despite the boron rings that actuate electrochemical NRR. To overcome these difficulties, the authors embedded these COFs on a nitrogen-doped carbon template to offer external electron conductivity and a stable substrate. Thus, metal-free electrocatalysts play a crucial role in NRR electrocatalysis by inhibiting the HER by electronic modifications in a carbon matrix and incorporating more accessible active sites, increasing the specific activity.

3.5 Bifunctional Electrocatalysts for NRR and OER

In the case of aqueous metal-N_2 batteries, the bifunctional NRR and OER performances during discharging and charging reactions become an essential aspect [32]. The electrocatalyst for NRR must exhibit a high ammonia yield rate and suppressed HER for a higher FE. Similarly, for the OER, the

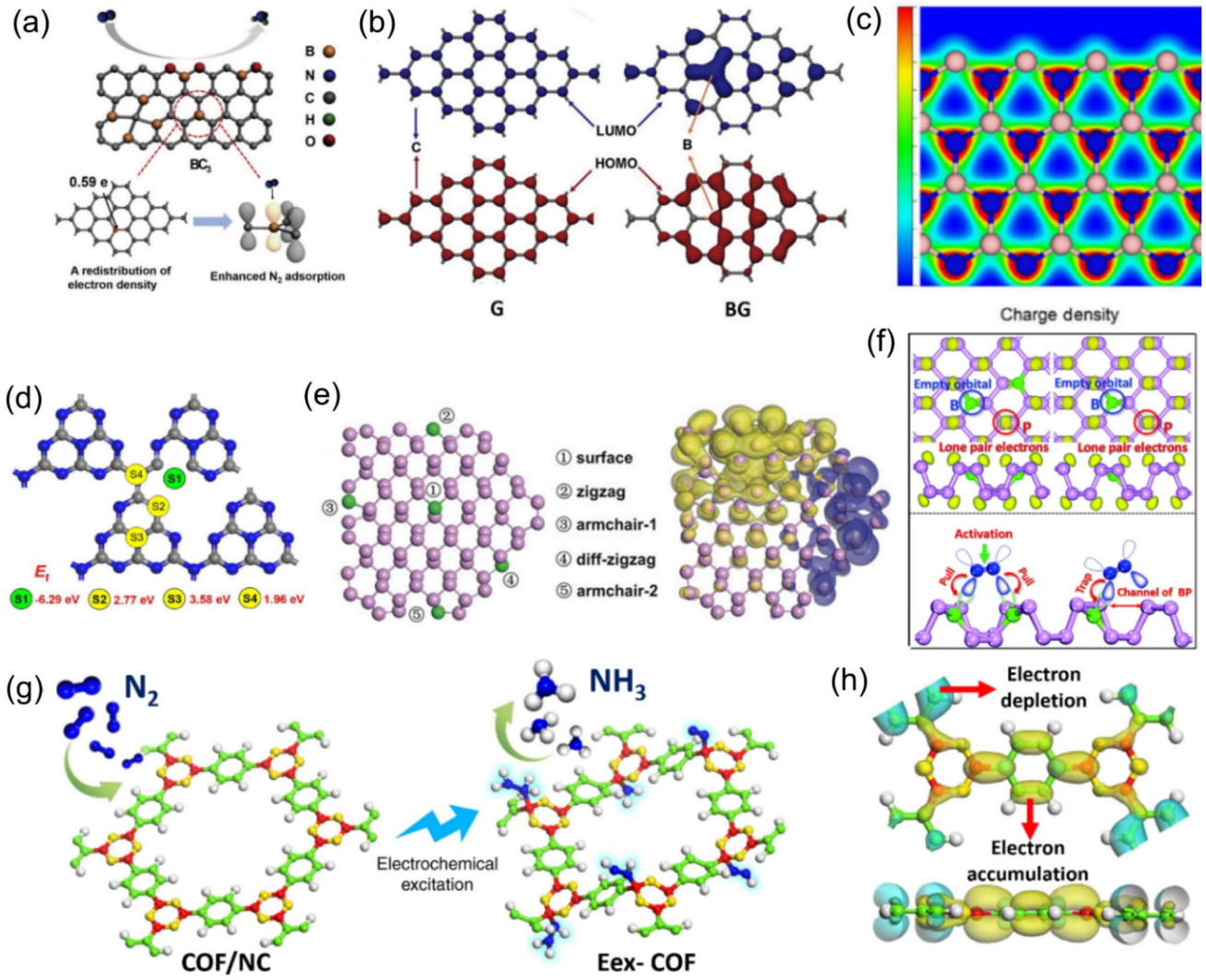

Fig. 14 **a** Illustration of NRR on boron-doped carbon graphene sheets with N_2 adsorption activity. **b** Diagram representing the HOMO–LUMO of BC_3 sheets. **c** Modified charge density distribution on the BC_3 nanosheets. Reprinted with permission from Ref. [148]. Copyright © 2018, Elsevier Ltd. **d** Representation of the S dopant position in the graphene sheets for NRR. Reprinted with permission from Ref. [164]. Copyright © 2020, Elsevier Ltd. **e** Illustration of exfoliated black phosphorous sheets with different charge densities around various positions. Reprinted with permission from Ref. [155]. Copyright © 2019, John Wiley & Sons, Inc. **f** Representation of boron-doped black phosphorous nanosheets showing the NRR mechanism. Reprinted with permission from Ref. [151]. Copyright © 2019, Royal Society of Chemistry. **g** Illustration of the synthesis route for Eex-COF in a N_2 atmosphere. **h** Modified charge distribution on the COF substrate after electrochemical excitation. Reprinted with permission from Ref. [145]. Copyright © 2019, Springer Nature Ltd

electrocatalyst must exhibit a low overpotential and faster reaction kinetics for effective performance [116]. Previous studies show better OER performances with low overpotentials and lower Tafel slope values and reveal improved NRR performances of the electrocatalyst. For instance, Li et al. [126] synthesized Co_xFe-MOF as an effective NRR and OER electrocatalyst because of the presence of abundant active sites and the positive synergistic effect of Co-Fe metals. Co_xFe-MOF exhibits a very low Tafel slope of 38 mV dec^{-1} and a lower overpotential of 280 mV @ 10 mA cm^{-2} for the OER. The electrocatalysts also reveal a high ammonia yield and FE of 25.64% at a very low potential (− 0.2 V vs. RHE), which hold prospects for a metal-N_2 battery. Similarly, Sun et al. [156] designed 2D NiFe nanomesh arrays on nickel foam, which imposes the combined effects of Ni–Fe and the hierarchical porosity from arranged nanolayers for higher OER/NRR performance. The electrocatalyst exhibits an even lower OER overpotential of approximately 191 mV and a considerably lower Tafel slope of approximately 43 mV dec^{-1}. The electrocatalyst delivers better NRR performance with a considerable yield and an FE of approximately 9.8%. Therefore, the electrocatalysts must hold efficient electrocatalytic activity for NRR and OER,

Table 1 Comparison of the NRR performances of the previously reported electrocatalysts

S. no	Electrocatalyst	Design	Electrolyte	Ammonia yield	FE/(%)	References
1	Au SAs/C_3N_4	Nanosheets	0.05 M H_2SO_4	1 305 μg h^{-1} mg_{Au}^{-1}	11.1	[73]
2	Ru SAs/N-C	Nitrogen-doped carbon	0.05 M H_2SO_4	120.9 μg h^{-1} mg_{cat}^{-1}	29.6	[157]
3	B, S-mRh	Mesoporous Rh film on Ni foam	0.1 M Na_2SO_4	11.88 μg h^{-1} cm^{-2}	28.89	[7]
4	$Rh_{1-x}Ru$/NF	Fusiform Rh_xRu_{1-x} film on Ni foam	0.1 M Na_2SO_4	30.28 μg h^{-1} mg_{cat}^{-1}	28.33	[7]
5	Pt SAs/WO_3	Nanoplate arrays	0.1 M K_2SO_4	342.4 μg h^{-1} mg_{Pt}^{-1}	31.1	[68]
6	Pd/γ-MnO_2	Phase interface by polyol reduction method	0.1 M KOH	19.72 μg h^{-1} mg_{Pd}^{-1}	8.4	[77]
7	Zn-doped Co_3O_4	O-vacancy engineering	0.1 M HCl	22.71 μg h^{-1} mg_{cat}^{-1}	11.9	[101]
8	M-COF_{BTC}	π-conjugated phthalocyanine	0.05 M HCl	$1.56\times10-11$ mol cm^{-2} s^{-1}	4.51	[91]
9	HT Au@MOF composite	Hydrophobic MOF shell with nitrogen concentration	0.1 M Na_2SO_4	49.5 μg h^{-1} mg_{cat}^{-1}	60.9	[70]
10	Fe_2O_3@MoS_2	MoS_2 nanoflowers on MOF template	0.1 M Na_2SO_4	112.15 μg h^{-1} mg_{cat}^{-1}	8.62	[158]
11	Eex-COF/NC	Salt template approach	0.1 M KOH	12.53 μg h^{-1} mg^{-1}	45.43	[145]
12	CeO_2/RuO_2/VG	Layered structures on graphene@ Ni foam	0.1 M KOH	50.56 μg h^{-1} mg_{cat}^{-1}	2.96	[159]
13	Mn-N–C SAC	Isolated manganese atomic sites on ultrathin carbon nanosheets	0.1 M HCl	21.43 μg h^{-1} mg_{cat}^{-1}	32.02	[89]
14	SA-Mo/NPC	Mo atoms anchored on N-doped porous carbon	1.0 M KOH	34 μg h^{-1} mg_{cat}^{-1}	14.6	[94]
15	2D A-MoO_{3-x}	2D Amorphous MoO_x monolayers for increasing Anderson localization	0.1 M KOH	35.83 μg h^{-1} mg_{cat}^{-1}	12.01	[160]
16	$La_xFeO_{3-\delta}$	Perovskite oxides with tunable V_o	Aq. 0.1 M Li_2SO_4	22.1 μg h^{-1} mg_{cat}^{-1}	25.6	[104]
17	$K_3Ti_8O_{17}$	Titanate-based mixed metal oxide	0.1 M HCl	31.6 μg h^{-1} mg_{cat}^{-1}	15	[128]
18	np-OVs NiO/MoO_3	Oxygen vacancy modulation via two-step dealloying and solid-state reaction	0.1 M PBS	35.4 μg h^{-1} mg_{cat}^{-1}	10.3	[100]
19	NiO	Hollow spherical structures	0.1 M Na_2SO_4	3.21 μg h^{-1} mg_{cat}^{-1}	1.37	[161]
20	NiO	Sea urchin-shaped morphology	0.1 M Na_2SO_4	1.66 μg h^{-1} mg_{cat}^{-1}	1.08	[161]
21	NiO	Cubic block structure	0.1 M Na_2SO_4	1.32 μg h^{-1} mg_{cat}^{-1}	0.81	[161]
22	NiO	Rod-like morphology	0.1 M Na_2SO_4	1.8 μg h^{-1} mg_{cat}^{-1}	1.17	[161]
23	Nb_2O_5-NCF	Anodization fabrication of Nb_2O_5 film with rich oxygen vacancies	0.1 M Na_2SO_4	2.52×10^{-10} mol cm^{-2} s^{-1}	9.81	[89]
24	$La_{0.5}Sr_{0.5}FeO_{3-\delta}$ ceramic oxide	Sr as dopant inducing agent in La–Fe–O	0.1 M Na_2SO_4	11.51 μg h^{-1} mg_{cat}^{-1}	0.54	[162]
25	Ti_2NT_x MXene	delaminated single-layer Ti_2N red-coloured material	0.1 M HCl	11.33 μg h^{-1} cm^{-2}	19.85	[87]
26	$VN_{0.7}O_{0.45}$ nanoparticles (gas flow reactor)	N sites adjacent to O as the active sites for NRR	1 M H_2SO_4 (soaked) 85 °C	3.3×10^{-10} mol cm^{-2} s^{-1}	1.6	[108]
27	Tetragonal Mo_2N	Urea glass synthesis route with better activity in acidic and neutral electrolyte	0.1 M HCl	1.99 μg h^{-1} mg_{cat}^{-1}	42.3	[147]
28	Defect rich γ-Mo_2N/h-BN	Interfacial engineering	0.1 M Na_2SO_4	58.5 μg h^{-1} mg_{cat}^{-1}	61.5	[112]
29	VN/Carbon Cloth	Well-coated nanowire arrays	0.1 M HCl	2.48×10^{-10} mol^{-1} s^{-1} cm^{-2}	3.58	[110]
30	2D NV-W_2N_3	Nitrogen vacancies posing major active sites	0.1 M KOH	11.6 μg h^{-1} mg_{cat}^{-1}	11.67	[80]

Table 1 (continued)

S. no	Electrocatalyst	Design	Electrolyte	Ammonia yield	FE/(%)	References
31	MXene/FeOOH	MXene sheets supported by FeOOH pillars	-	4.72 μg h^{-1} mg_{cat}^{-1}	1.44	[163]
32	MnO_2-$Ti_3C_2T_x$	Heterointerface between two structures	0.1 M HCl	34.12 μg h^{-1} mg_{cat}^{-1}	11.39	[135]
33	N-doped nanoporous Carbon Membranes (NCM)	N-dopant engineering between graphitic layers	0.1 M HCl	0.08 g m^{-2} h^{-1}	5.2	[144]
34	S-NV-C_3N_4	S-dopants with N-vacancies on graphitic layers	0.5 M $LiClO_4$	32.7 μg h^{-1} mg_{cat}^{-1}	14.1	[164]
35	FL-BP NSs	Exfoliated black phosphorous with a similar electronic configuration of P and N	0.01 M HCl	31.37 μg h^{-1} mg_{cat}^{-1}	5.07	[155]
36	CoP hollow nanocage	Two-step solvothermal conversion of LDH and phosphorization	1.0 M KOH	10.78 μg h^{-1} $mg_{cat.}^{-1}$	7.36	[142]
37	Fe–N/C-CNTs	MOF-derived catalyst with Fe-N_3 catalytic active sites	0.1 M KOH	34.83 μg h^{-1} $mg_{cat.}^{-1}$	9.28	[165]
38	$Pd_{0.2}Cu_{0.8}$/rGO	2D graphene sheets utilized to prevent aggregation of alloying NP	0.1 M KOH	2.8 μg h^{-1} $mg_{cat.}^{-1}$	~4.5	[166]
39	B/N-CNF	Effective utilization of boron-doped NCNF for high metal-free catalytic activity	0.1 M KOH	20.0 μg h^{-1} $mg_{cat.}^{-1}$	13.2	[147]
40	NV-W_2N_3	Nitrogen vacancy-enriched W_2N_3 with enhanced stability over the MvK mechanism	0.1 M KOH	11.7 μg h^{-1} $mg_{cat.}^{-1}$	11.7	[80]
41	FeS@MoS_2/CFC	FeS dotted MoS_2 nanosheets	0.1 M KOH	2.46 μg h^{-1} $mg_{cat.}^{-1}$	0.067	[167]
42	PdO/Pd/CNTs	Heterojunctions fabricated by UV-laser irradiation	0.1 M NaOH	18.2 μg h^{-1} $mg_{cat.}^{-1}$	11.5	[168]
43	Au@TiO_2	Enriched oxygen vacancy and electron donation by TiO_2	0.1 M HCl	64.6 μg h^{-1} $mg_{cat.}^{-1}$	29.5	[47]

Data are from different referenced resources

which reduces the required charging potential and increases the discharge cell voltage, respectively (Table 1).

Thus, electrocatalysts can be designed with various strategies that effectively promote the NRR and suppress the HER. Electrocatalysts for nonaqueous-based systems have not attracted interest because of the high maintenance and instability of electrocatalysts in nonaqueous media. However, research on electrocatalysts has been targeted for aqueous-based systems for which the kinetics has been sluggish but shows promising results. Moreover, the bifunctional performances of the electrocatalysts are highly anticipated to achieve efficient rechargeability of aqueous metal-N_2 batteries. Metal-N_2 batteries can be fabricated with electrocatalysts having a stable architecture, increased active site density, large surface areas, selective adsorption towards N_2, and prominent HER mitigation.

4 Electrolytes for NRR

Electrocatalysts are the most studied entity in the NRR process. However, electrolytes form the environment for efficient NRR electrocatalysis, which plays a major role in determining the better performance of the electrocatalyst and the metal-N_2 battery. They are found to actively inhibit the progress of the HER and supply protons to the surface of the electrocatalyst [14]. Designing the appropriate electrolyte for better NRR performance is as essential as designing the electrocatalyst because the kinetic regulation of the protons and nitrogen is processed by the electrolytes. One important property of the electrolyte is the solubility of N_2 for feasible transport to the active site [169]. The pH of the electrolyte, the nature of the electrolyte and the counterions determine nitrogen and proton migration to the surface of the electrode. Researchers have presented various electrolytic strategies to overcome the HER through the electrolyte configuration by limiting proton availability and proton migration and creating a swift pathway for the N_2 species.

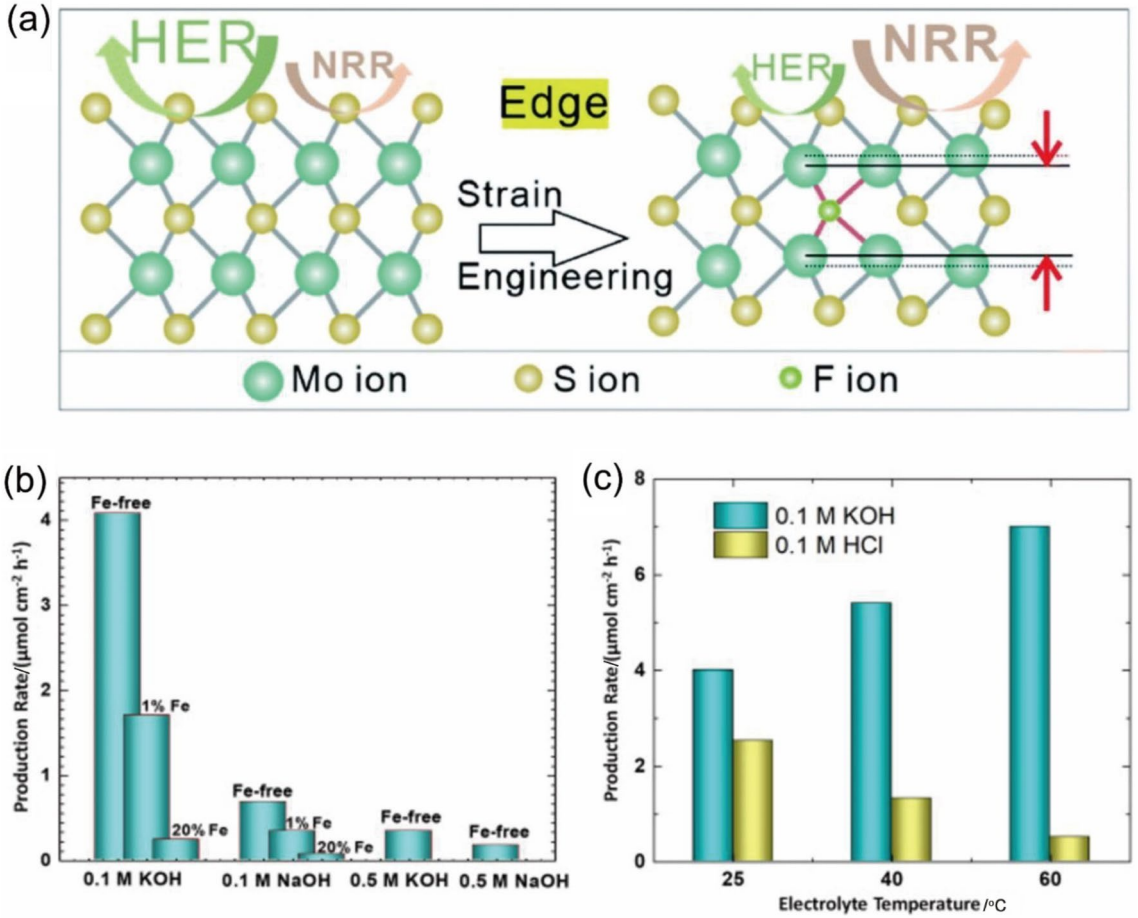

Fig. 15 **a** Scheme representing strain engineering by F doping of the MoS_2 structure for higher NRR performance in acidic electrolytes. Reprinted with permission from Ref. [171]. Copyright © 2019, Royal Society of Chemistry. **b** Comparison of the ammonia production of the C-ZIF-1000–1 h catalyst under various electrolytes. **c** Ammonia production performance in acidic and alkaline electrolytes at various temperatures. Reprinted with permission from Ref. [172]. Copyright © 2020, Elsevier Ltd

From the electrolyte perspective, N_2 electroreduction can be classified into two major categories: the direct pathway and the mediated pathway. The direct pathway producing ammonia directly from NRR experiments is again classified as nonaqueous and aqueous pathways. The mediated pathway involves intermediate formation and is obviously nonaqueous. The intermediates are usually nitrides, which can be further hydrolyzed to produce ammonia.

Aqueous electrolytes are generally termed water-based electrolytes that contain deionized H_2O as the solvent and are applied to electrochemical cells for redox reactions. They are further classified as acidic (0.1 M HCl, 0.1 M H_2SO_4), alkaline (0.1 M KOH, 0.1 M NaOH) and neutral (PBS, 0.1 M Na_2SO_4) electrolytes that exhibit the activity of their own kind. The deviation of the pH values will be larger near the electrode surface than in the bulk of the electrolyte because of the protonation of N_2 that affects the yield rate and FE. NRR in acidic electrolytes is slightly sluggish even with the best electrocatalyst, and HER occurs feasibly and rapidly in the presence of hydronium (H_3O^+) ions, which are abundant in aqueous acidic electrolytes [170]. The DFT studies suggest that Mo atoms in MoS_2 hold a more positive charge that provides sites for nitrogen adsorption and are more susceptible to NRR, but they exhibit a low ammonia yield and a minimum faradaic efficiency of 0.096% in 0.1 M HCl [82]. This result is ascribed to the strong hydrogen production in the acidic medium that is inferior to that of the 0.1 M Na_2SO_4 electrolyte. However, very few reports suggest increased ammonia production over the HER in acidic electrolytes. For example, Liang et al. [171] improvised MoS_2 sheets through F-doped strain engineering, which suppressed the HER and enhanced the NRR selectivity (Fig. 15a). The smaller size and great electronegativity of the F atom create strain in the MoS_2 lattice, making it defective, exhibiting an FE of approximately 20.6% in 0.05 M H_2SO_4 electrolyte**.** However, acidic electrolytes with lower pH values, i.e., increased H^+ concentrations, surprisingly facilitate NRR over HER.

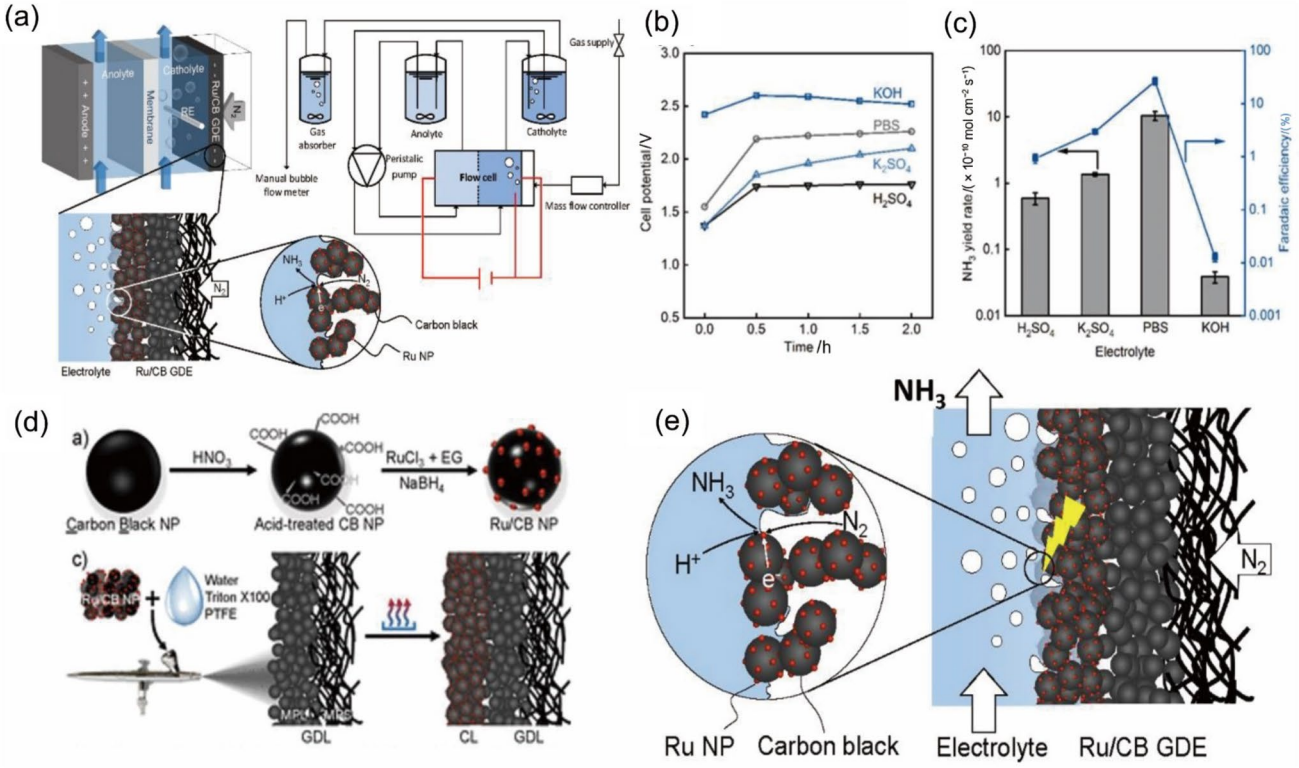

Fig. 16 **a** Scheme representing ammonia production on the GDL embedded with Ru NP under a flow reactor. **b** Comparison of the cell potential of the flow reactor for NRR under various electrolytes. **c** Comparison of the ammonia yields and FE under various electrolytes. **d** Illustration of the synthesis route of Ru/CB NPs and their fabrication onto the GDL. **e** Scheme representing ammonia production in the GDL embedded with Ru NPs in a flow reactor. Reprinted with permission from Ref. [15]. Copyright © 2021, American Chemical Society

Despite acidic electrolytes being the prime proton donors for the HER in aqueous solution, they can catalyse ammonia production in a controlled environment. However, the long-term stability of electrocatalysts in an acidic electrolyte poses a serious threat. Additionally, the evolution of hydrogen from the excess protons can lead to a higher HER than the expected NRR. Alkaline electrolytes tackling all the abovementioned issues of proton migration are found to suppress the intrinsic HER.

Alkaline electrolytes are the most preferred medium for most nitrogen reduction experiments. They are inexpensive, easy to handle, do not corrode the electrochemical cell and provide sufficient H^+ ions for protonation. Mukherjee et al. [172] studied ZIF-8 frameworks for electrocatalytic NRR for various pyrolysis temperatures, varied concentrations of Fe doping and different electrolytes (0.1 M KOH, 0.1 M NaOH and 0.1 M HCl). For the C-ZIF-1000–1 h catalyst, the electrolytes KOH and NaOH with varied cations are examined, which indicates a higher ammonia yield (Fig. 15b, c). Including the concentration effects, it is observed that the NaOH electrolyte is always one order behind the KOH electrolyte, indicating feasible K^+ ion transport in the electrolyte, suggesting favourable NRR kinetics in the KOH electrolyte.

In addition to acidic and alkaline electrolytes, neutral electrolytes play an efficient role in electrochemical N_2 reduction. Notably, phosphate buffer saline (PBS) electrolytes have found importance in the NRR by suppressing the HER and exhibiting better catalytic activity than NaOH and H_2SO_4 electrolytes. For example, Wei et al. [15] extensively studied the flow reactor for ammonia synthesis and electrolytes of varied pH (H_2SO_4, K_2SO_4, PBS and KOH) (Fig. 16a). The study finds effective HER suppression in the neutral electrolyte initially, followed by the alkaline electrolyte (PBS > K_2SO_4 > KOH > H_2SO_4) (Fig. 16b, c). The buffer effects of H_2SO_4/PBS, where PBS is a neutral medium, effectively reduce the proton concentration, which increases the pH of the electrolyte. Hence, the electrocatalytic surfaces are limited to adsorbing protons, and relatively high N_2 species are adsorbed on the active sites. However, protonation of the adsorbed nitrogen is essential for forming ammonia, where the limited proton availability enhances the ammonia production rate and suppresses the HER. Therefore, increasing the pH of the electrolyte suppresses the HER, and the limited proton availability is facilitated to enhance the NRR. Additionally, the PTFE (polytetrafluoroethylene)-coated gas diffusion layer (GDL) prevents the electrode from becoming

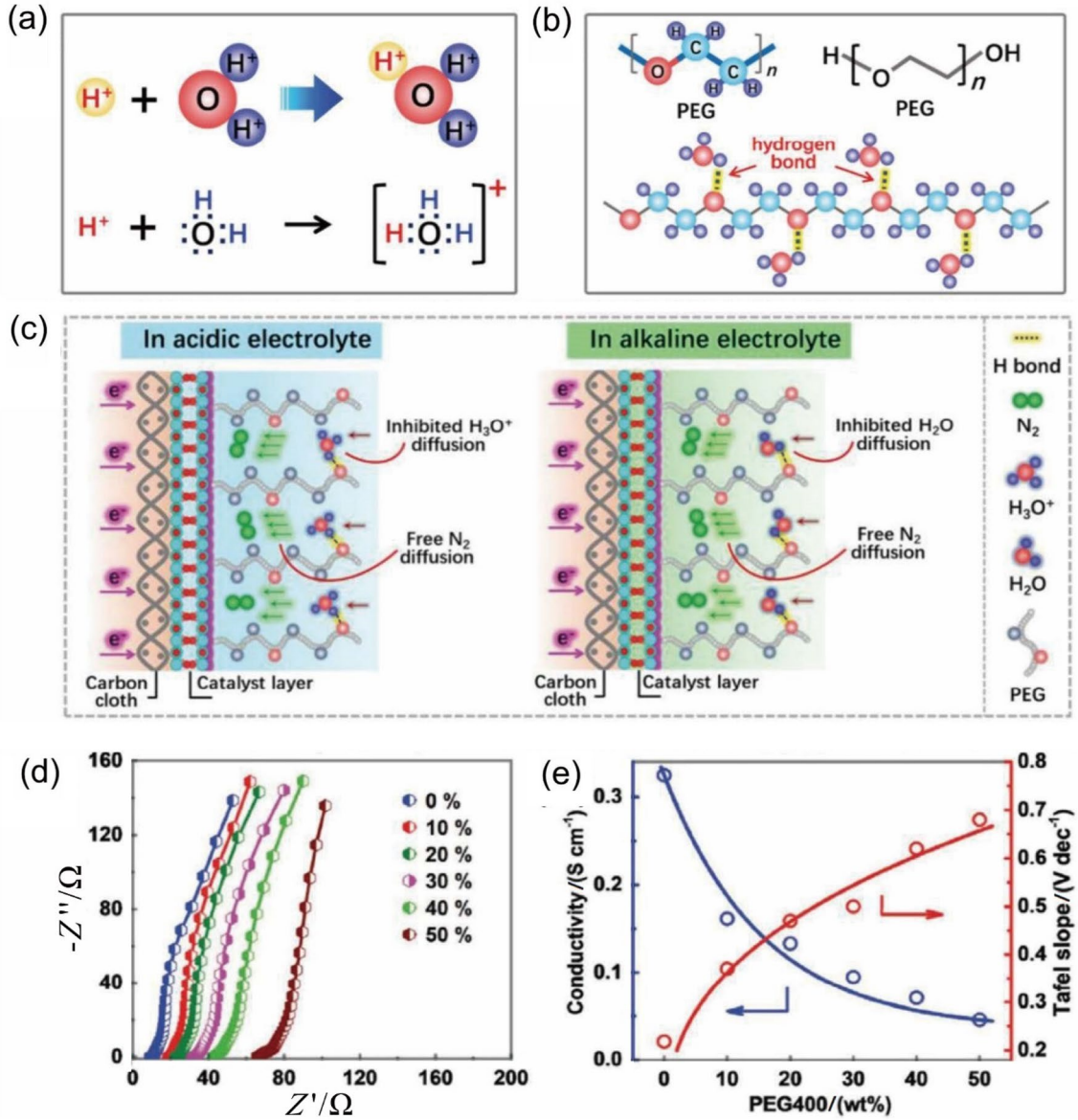

Fig. 17 **a** Representation of the hydronium ions in the acidic electrolyte. **b** PEG-400 showing the interactive sites for hydronium ion interaction through hydrogen bonding. **c** Scheme showing the water molecule interaction with PEG-400 under acidic and alkaline electrolytes and free N_2 mobility. **d** Nyquist plots for the PEG400-containing electrolytes. **e** Plots depicting the variation in conductivity and Tafel slopes with increasing PEG400 concentration in the electrolyte. Reprinted with permission from Ref. [16]. Copyright © 2021, John Wiley & Sons, Inc

wettable, which increases N_2 diffusion and inhibits hydrogen production in the flow cell (Fig. 16d, e).

In addition to the reported electrolytes, a noteworthy strategy is used to suppress the HER by limiting proton migration and improving feasible N_2 movement into the electrolyte. This novel scenario involves using an additive in the electrolyte that effectively limits proton migration into the electrolyte.

The molecular crowding effect observed in living cells restricts water activity by hydrogen bonding interactions between water molecules and long-chain macromolecules (Fig. 17a, b) [173-176]. Inspired by this mechanism of restricting water molecule mobility, Guo et al. [16] utilized PEG400 (polyethylene glycol), a long-chain polymer, to effectively suppress the ion flow in the aqueous electrolyte by hydrogen bonds. PEG additives increase the electrochemical stability window for water electrolysis inhibiting the HER. Because of the suppression in ion flow, the electrolyte supplies sufficient protons to protonate the adsorbed N_2, which effectively inhibits the HER, as represented in Fig. 17c. Consequently, an increase in the solution resistance (Fig. 17d) and a decrease in the ionic conductivity

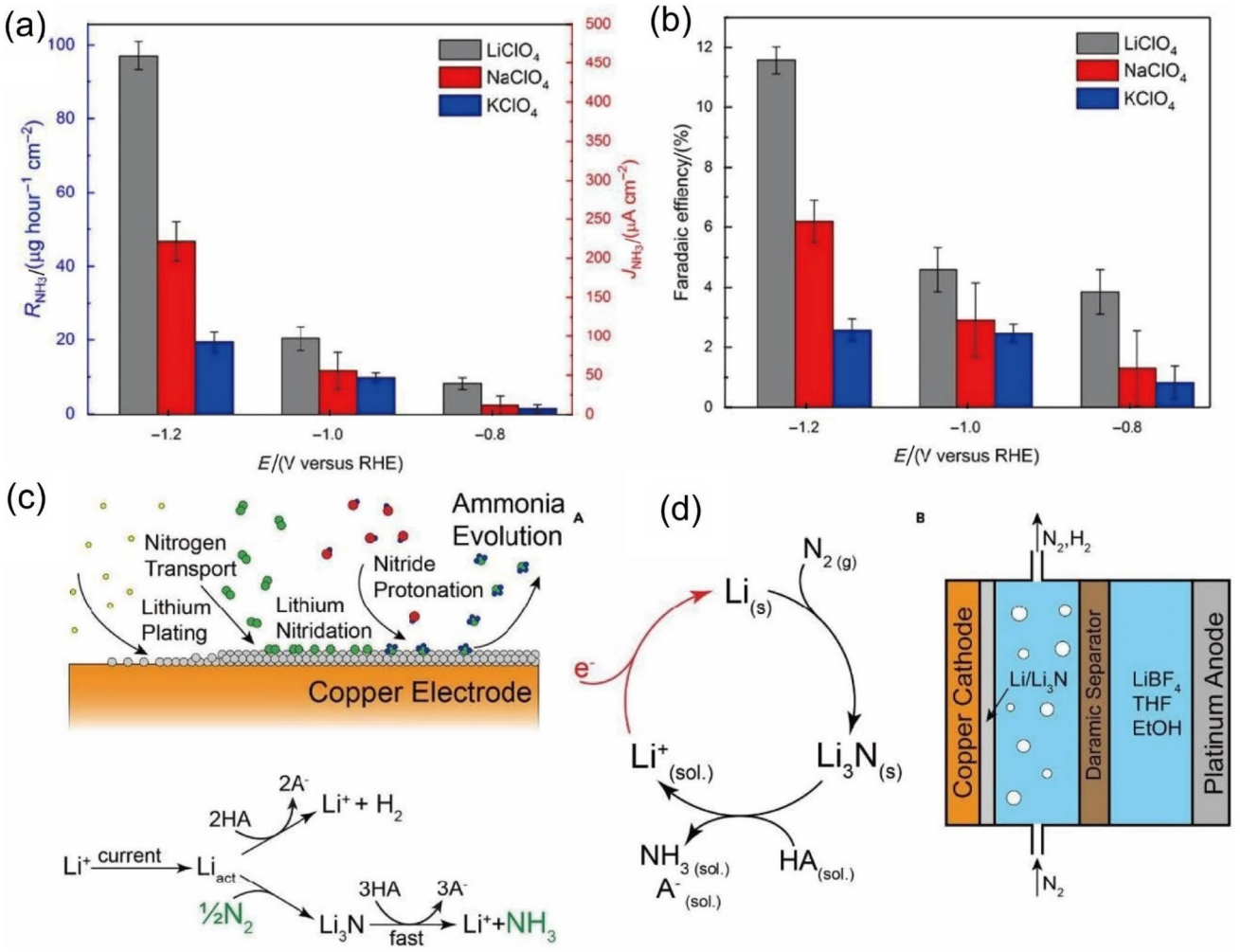

Fig. 18 NRR performances under the influence of Li^+, Na^+, and K^+ counterions. **a** ammonia yields and **b** faradaic efficiency. Reprinted with permission from Ref. [178]. Copyright © 2018, American Association for the Advancement of Science. **c** Schematic of LiMEAS on Cu electrode surfaces and the mechanism of Li nitridation. **d** Diagram showing the Li cycling for LiMEAS in the electrolyte mixture of $LiBF_4$, THF and EtOH. Reprinted with permission from Ref. [43]. Copyright © 2019, Elsevier Ltd

(Fig. 17e) of the electrolyte were observed with increasing PEG400 concentration. Therefore, an optimum 20 wt% (wt% means the weight percentage) PEG400 concentration was adopted to achieve a higher FE of approximately 32.13% in acidic electrolytes, indicating excellent HER suppression performance. Similar effects of lower conductivity and high solution resistance with an increase in concentration and longer chains of PEG are observed in previous studies [177]. In addition, the neutral and basic solutions reveal similar activity under PEG400 additive concentrations. Hence, the presence of additives in the electrolyte to suppress HER decreases the conductivity of the electrolyte but manages to improve the NRR performance.

One important effect that determines the electrolytic effect in NRR is the effect of counter ions in the medium. For instance, Song et al. [178] examined the effects of counter ions (Li^+) in the electrolyte with the corresponding perchlorate solutions ($LiClO_4$) diluted in deionized water. The ions form a Stern layer across the electrode that effectively mediates N_2 adsorption and repels H^+ from the electrode. The study included other perchlorate solutions as a control experiment with Na^+ and K^+ ions from their perchlorate solutions ($NaClO_4$ and $KClO_4$). Higher ammonia production rates and faradaic efficiency can be observed from the Li^+ ion-mediated electrolyte due to the steric effects between the counter ions and N_2 (Fig. 18a, b). Additionally, the rates are found to decrease with an increasing ionic radius ($Li^+ < Na^+ < K^+$). Thus, Li^+ counterions in the electrolyte enrich the electrodes electrostatically, which increases the N_2 concentration on the electrode surface compared to that in the electrolyte medium.

Nonaqueous electrolytes can be employed to effectively suppress the HER and increase N_2 solubility in an electrolytic medium. Recently, organic and ionic liquids have

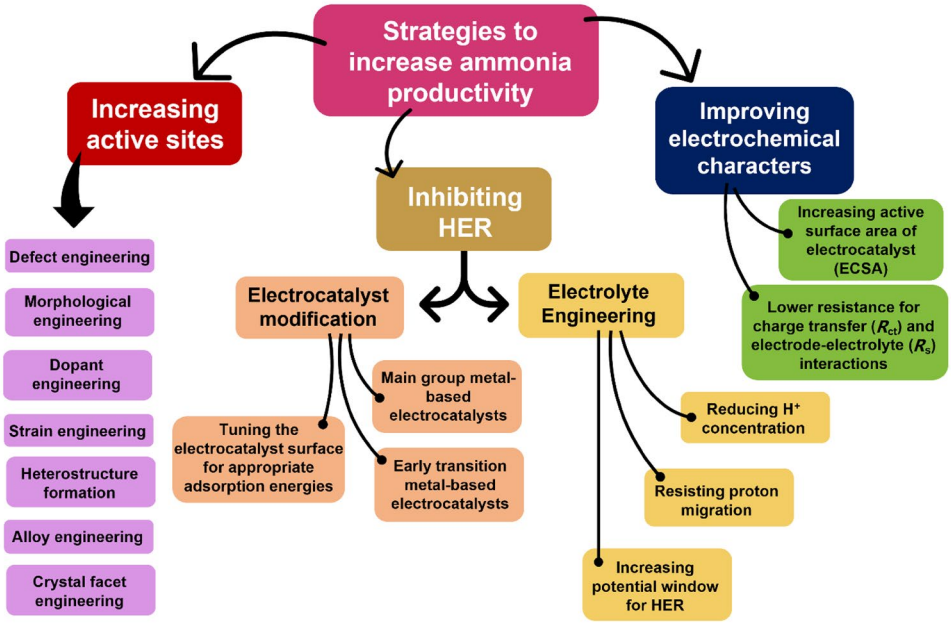

Fig. 19 Schematic representation of the general strategies for increasing NRR performance in aqueous environments

attracted interest owing to the steric effects of the ions and the N_2 gas in the electrolyte. A novel strategy for suppressing HER with higher ammonia production is by adopting the Li-mediated electrochemical ammonia synthesis (LiMEAS) technique under organic electrolytes with proton sources for ammonia production [40, 41, 179]. Lazouski et al. [43] reported the LiMEAS procedure with lithium tetrafluoroborate ($LiBF_4$) mixed with sieve-dried THF and varying EtOH concentrations as the proton source (Fig. 18c, d). With Li counterions in the electrolyte, faster reaction kinetics and feasible product (Li_3N) formation are observed, which upon protonation with sufficient ethanol concentrations is converted to ammonia. In addition, the author calculated the effects of nitrogen and proton carrier concentration on the formation of ammonia. It is also found that even smaller amounts of water in the electrolyte drastically affect ammonia formation and produce hydrogen at a very fast rate. Thus, an organic liquid (THF) is used as the electrolyte, and its stability in LiMEAS must be analysed. Hence, Sažinas et al. [180] analysed three organic liquids (DG, THF, DME) and reported the compatibility of THF, which is applicable to the novel LiMEAS approach. In nonaqueous conditions, proton sources are necessary to protonate the adsorbed N species for ammonia production. Because of the feasible H-donating property of ethanol, it is widely used as a sacrificial proton source in LiMEAS to form LiOEt [43]. Other than ethanol, ammonia production in LiMEAS is facilitated by using tetraalkyl phosphonium salt, which undergoes cycles of deprotonation–reprotonation, additionally improving the ionic conductivity [181]. Further, the hydrogen oxidation reaction (HOR) is used as the proton source to produce ammonia from the LiMEAS procedure with high yield and FE [182]. Therefore, sacrificial proton sources and H_2 oxidation reactions are adopted to protonate the adsorbed N_2, resulting in ammonia formation through LiMEAS. However, the stability of the ionic electrolytes, controlled environment and frequent maintenance pose a serious threat and involve high cost and labour to stabilize the system for practical use. Thus, metal-N_2 batteries can be envisioned to work more efficiently under low maintenance in aqueous electrolytes than under ionic electrolytes.

5 Summary of the Strategies for Improving Ammonia Productivity

The major aspects to achieve higher ammonia productivity are (i) increasing the available number of active sites, (ii) suppressing the HER, and (iii) improving the electrochemical characteristics of the electrocatalysts. A schematic representation of the strategies for improving NRR performance in aqueous environments by electrocatalyst and electrolyte engineering is presented in Fig. 19.

First, improving the number of active sites is achieved through electrocatalyst engineering by tailoring the structural, morphological, and electronic effects of various metals. Modifications include defect engineering [81], morphological engineering [161], dopant engineering [75], strain engineering [171], heterostructure formation [183], alloy engineering [125], and crystal facet regulation [184], which improve the structural and electronic effects in electrocatalysts, achieving superior performances. Structural and morphological engineering incorporates highly accessible active sites and the stability of the structures. Electronic

modifications alter the conduction and valence bands of metals near the Fermi level, resulting in higher activity and selectivity towards NRR [185]. Studies have shown promising improvement in ammonia yield by tuning the electrocatalyst for a higher number of active sites.

Second, competitive side reactions such as the HER must be preferably suppressed to increase the selectivity for N_2 adsorption, resulting in higher ammonia yields and FE. HER can be effectively suppressed by electrocatalyst modification by appropriately tuning the electronic structures of the active sites [37], adopting early transition metal-based electrocatalysts [35], and main group metal-based electrocatalysts [127]. Additionally, the HER can be suppressed by a reliable electrolyte engineering strategy. Reducing the proton concentration [15], resisting proton migration [16], and increasing the potential window for electrolysis [17] are proven to be effective strategies for inhibiting the HER in aqueous electrolytes. Adopting nonaqueous electrolytes with various proton sources is also an effective route to generate better NRR performance and inhibit the HER [43].

Third, the intrinsic electrochemical characteristics, such as conductivity and electrochemical active surface area (ECSA), of the electrocatalyst are improved [186, 187]. The electrocatalyst must exhibit lower charge transfer resistances and electrode–electrolyte resistances to achieve faster electronic conductivity and faster reaction kinetics. The electrocatalysts are incorporated on a N-doped carbon matrix, which can be designed by several methods to achieve faster conductivity due to the highly polarized electronically tuned substrates [188]. Moreover, increasing the ECSA of the electrocatalyst incorporates higher exposure of active sites for N_2 adsorption and electrolytic ions. Hence, the abovementioned strategies can be followed to achieve higher ammonia yield and FE and to exhibit better electrochemical performances for the electrocatalyst.

Nevertheless, there is a high risk of overestimating or underestimating the ammonia yield due to the low sensitivity of detection methods, the nitrogenous contents of the electrode and the presence of impurities in the electrolyte, membrane/separators and analyte gas contents [59]. Proper purification procedures and careful observation of the contents of electrocatalysts and electrolytes are mandatory while performing NRR studies.

6 Development of Metal-N_2 Batteries

The abovementioned, recently reported electrocatalysts are observed to exhibit outstanding activity, selective adsorption towards N_2 and considerable stability towards NRR. These features of electrocatalysts with different morphologies and varied spans of activity can be incorporated into a metal N_2 battery system to provide overall battery performance. Different metal-N_2 battery systems with various anode materials (Li, Na, Al, Zn) have been reported, and their performances are analysed. Metal N_2 batteries can be differentiated based on their mechanisms in nonaqueous and aqueous electrolytes. The Li-N_2 battery, Na-N_2 battery and Al-N_2 battery have been demonstrated under nonaqueous electrolytes, which form nitrides at the cathode. The Zn-N_2 battery and Al-N_2 battery have been demonstrated under aqueous alkaline electrolytes, which follow the NRR as the cathodic reaction during discharge. Various metal-N_2 batteries and their reaction schemes in nonaqueous and aqueous environments are explained in the following sections.

6.1 Nonaqueous Metal-N_2 Batteries

Nonaqueous metal-N_2 batteries perform under aprotic electrolytes, which form nitrides as intermediates at the cathode. Ammonia production involves a two-step process in aprotic metal-N_2 batteries. Li-based batteries are the first reported metal-N_2 batteries that perform in aprotic electrolytes (Fig. 20a) [20]. During discharge, the adsorbed N_2 on the cathode is reduced by the positive Li ions from the electrolyte to form a Li_3N intermediate on the cathode. During charging, the intermediate on the cathode is oxidized to release N_2 gas and the Li ions solvate to the metal electrode for deposition. The Li-N_2 battery, as reported by Zhang et al. [20], has the FE of approximately 59% in ether-based organic electrolytes. This Li-N_2 battery with bare carbon cloth (CC) as the GDE exhibited maximum FE at − 1.08 V, additionally, with a charging FE of nearly 51%. Cyclic voltammetry curves for the Li-N_2 battery under Ar- and N_2-saturated electrolytes exhibit Li intercalation and N_2 fixation on the cathode, respectively (Fig. 20b). In the case of the charging cycle, almost 87% of the Li_3N product decomposed back to N_2 and was quantified by colourimetric assays that show the charge−discharge cycle of Li-N_2, proving its efficiency (Fig. 20c).

Later, Zhou et al. [189] studied the Li_3N intermediate for stability and its water-absorbing tendency after testing for 30 days in TEGDME, which showed considerable stability. Later, Na-N_2 batteries were reported under a similar organic electrolyte, and the N_2 fixation performance was analysed with CC/α-MnO_2 as the cathode (Fig. 20d) [29]. The charge−discharge mechanisms were similar to those of Li-N_2 batteries with nitride formation at the cathode. The Na-N_2 battery with the CC/α-MnO_2 cathode exhibited an FE of approximately 26%, which indicated poor catalytic activity. The first charge−discharge curves of the Na-N_2 battery reveal a constant potential density for higher specific capacity values of the battery under various current densities (Fig. 20e). However, the Na-N_2 battery was demonstrated in simulated actual air conditions (NAA-80% N_2 and 20% O_2), which show that the Na-N_2 batteries can deliver a specific

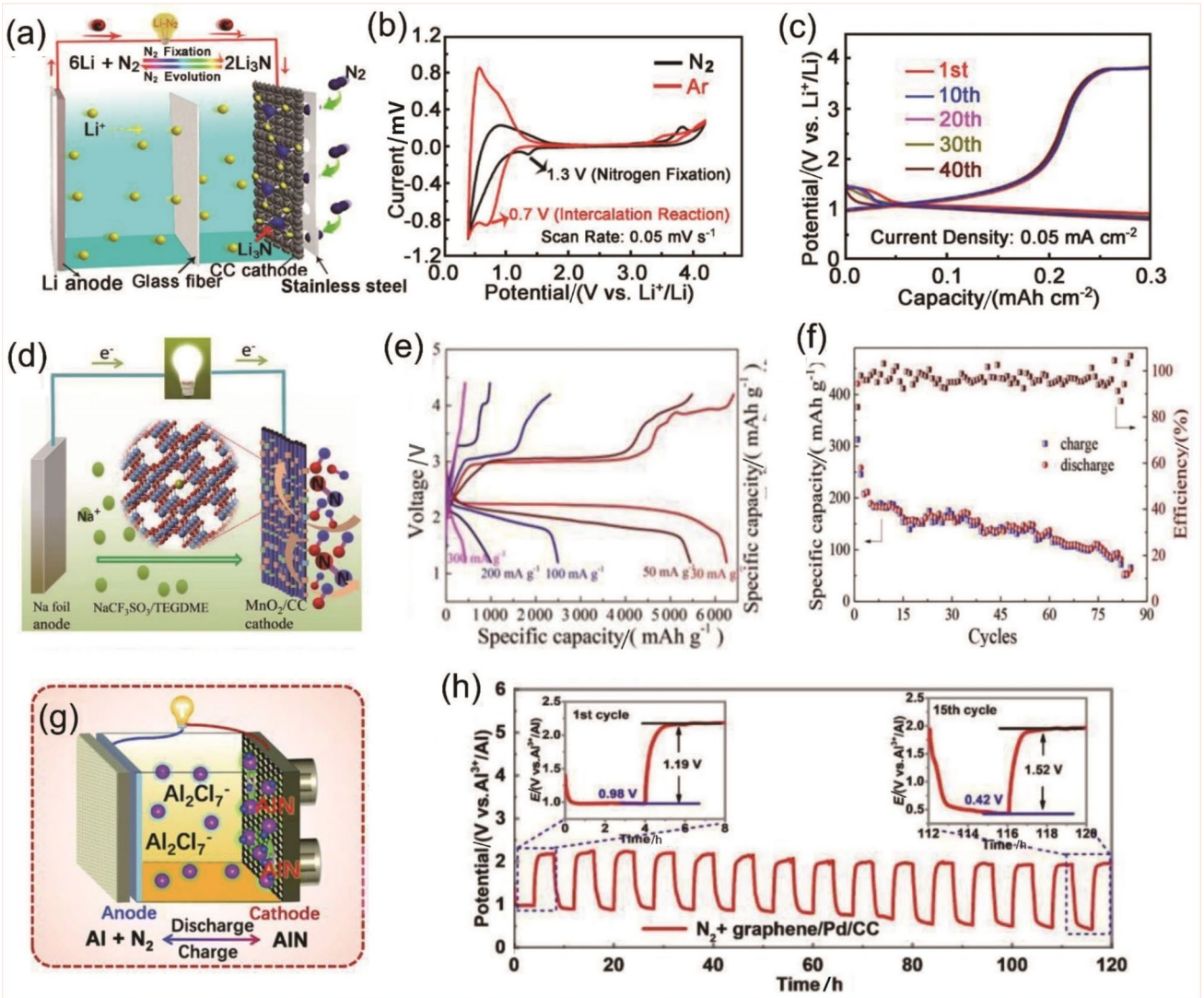

Fig. 20 **a** Schematic of the Li-N_2 battery with the CC cathode in an organic electrolyte. **b** CV curves for the Li-N_2 battery under Ar and N_2 atmospheres. **c** Charge−discharge curves for various cycles for the Li-N_2 battery at 0.05 mA cm^{-2}. Reprinted with permission from Ref. [20]. Copyright © 2018, Elsevier Ltd. **d** Schematic of the Na-N_2 battery with the MnO_2/CC cathode in an organic electrolyte. **e** Comparison of the first charge−discharge curves of the CC/α-MnO_2 samples at various current densities. **f** Cycling performances of NAA batteries at 50 mA g^{-1}. Reprinted with permission from Ref. [29]. Copyright © 2019, Elsevier Ltd. **g** Illustration of the Al-N_2 battery with the graphene/Pd/CC cathode in an ionic electrolyte. **h** Cycling performances of the Al-N_2 battery at 0.05 mA cm^{-2} with graphene/Pd/CC as the air cathode. Reprinted with permission from Ref. [47]. Copyright © 2020, Royal Society of Chemistry

capacity that retains at least 10 mAh g^{-1} at 50 mA g^{-1} even after 70 cycles. The NAA experiments reveal the promising activity of the Na-N_2 battery that can be cycled at ambient atmospheres in the future (Fig. 20f).

Following the Na-N_2 battery, the Al-N_2 battery was fabricated with the ionic electrolyte and exhibited a maximum FE of approximately 51.2% in an open circuit voltage of 1.55 V (Fig. 20g) [47]. The deposited discharge product was further hydrolysed to produce ammonia or recycled during the charging process. The Al-N_2 battery fabricated with graphene/Pd/CC as the air cathode reveals a modest change in the charge−discharge curves for 120 h at 0.05 mA cm^{-2}, which reveals the promising activities of this battery (Fig. 20h). One major advantage of the aprotic electrolyte is the suppression of proton migration in the electrolyte, which increases the efficiency of the metal-N_2 battery and ensures nitride formation at the cathode. Moreover, the nitrides formed during discharge can be hydrolysed to produce ammonia [20, 29]. However, the controlled environment, availability and cost of the electrolytes, instability, and high maintenance pose a major drawback in designing a metal-N_2 battery for scalable applications in nonaqueous electrolytes.

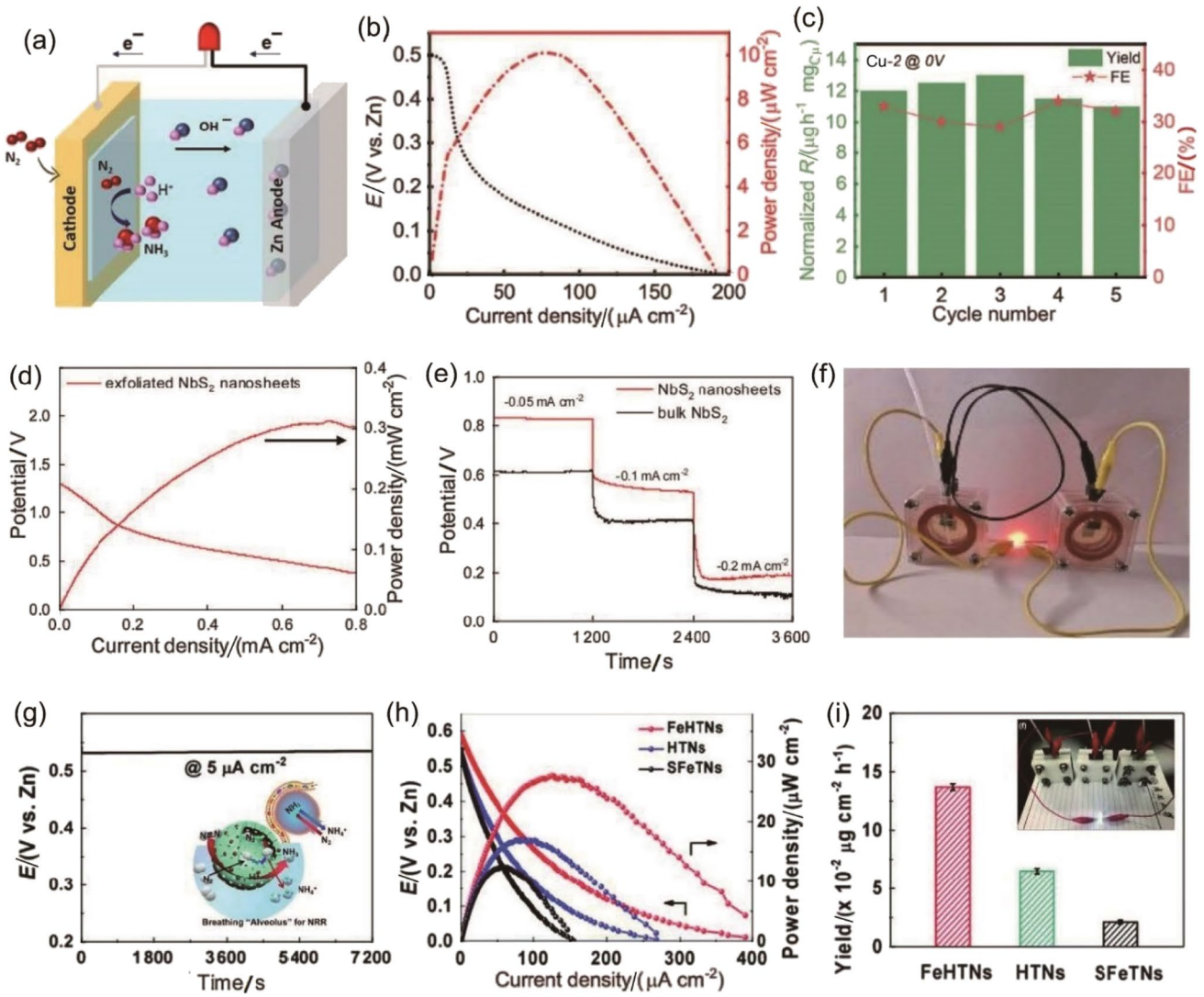

Fig. 21 **a** Illustration of the Zn-N_2 battery at the discharge cycle. **b** Polarization curves and power density plots of the aqueous Zn-N_2 battery with the Cu/CP cathode. **c** Cycling tests of the Zn-N_2 battery with the Cu/CP cathode. Reprinted with permission from Ref. [50]. Copyright © 2019, Royal Society of Chemistry. **d** Polarization and power density plots for the Zn-N_2 battery fabricated with NbS_2 NS as the air cathode. **e** Potentials at various discharging current densities for the NbS_2-fabricated Zn-N_2 battery. **f** Optical photograph of the coupled Zn-N_2 battery with the NbS_2 cathode. Reprinted with permission from Ref. [30]. Copyright © 2020, Elsevier Ltd. **g** Discharge curves of the Zn-N_2 battery with the Fe-HTN cathode (the inset: hollow FeHTN catalysts mimicking the human alveolus). **h** Polarization curves and power density plots for the FeHTN-fabricated Zn-N_2 battery. **i** Comparison of the ammonia yield for various samples from the Zn-N_2 battery. Reprinted with permission from Ref. [31]. Copyright © 2021, Royal Society of Chemistry

6.2 Aqueous Metal-N_2 Batteries

Using aprotic liquids as electrolytes has disadvantages with the sustainability of the battery and is obviously not environmentally friendly. To overcome the limitations of ionic electrolytes, aqueous metal-N_2 batteries were fabricated. The first reported alkaline metal-N_2 battery was fabricated by Du et al. [50], as shown in Fig. 21a.

The reported Zn-N_2 battery was constructed with Cu nanoparticle-deposited carbon paper (Cu/CP) as the cathode, Zn metal as the anode and 1.0 M KOH as the electrolyte. The Zn-N_2 battery delivered a maximum power density of approximately 10.1 μW cm^{-2} and a striking FE of nearly 59% (Fig. 21b, c). In aqueous metal-N_2 batteries, discharge occurs with NRR, as in Eq. (10), and charging occurs with the OER, as in Eq. (11). The work widened the scope for aqueous metal-N_2 batteries and then started to amass several aqueous-based Zn-N_2 battery systems with different cathode designs.

The general discharge−charge mechanism for aqueous alkaline electrolytes occurring at the cathode is as follows.

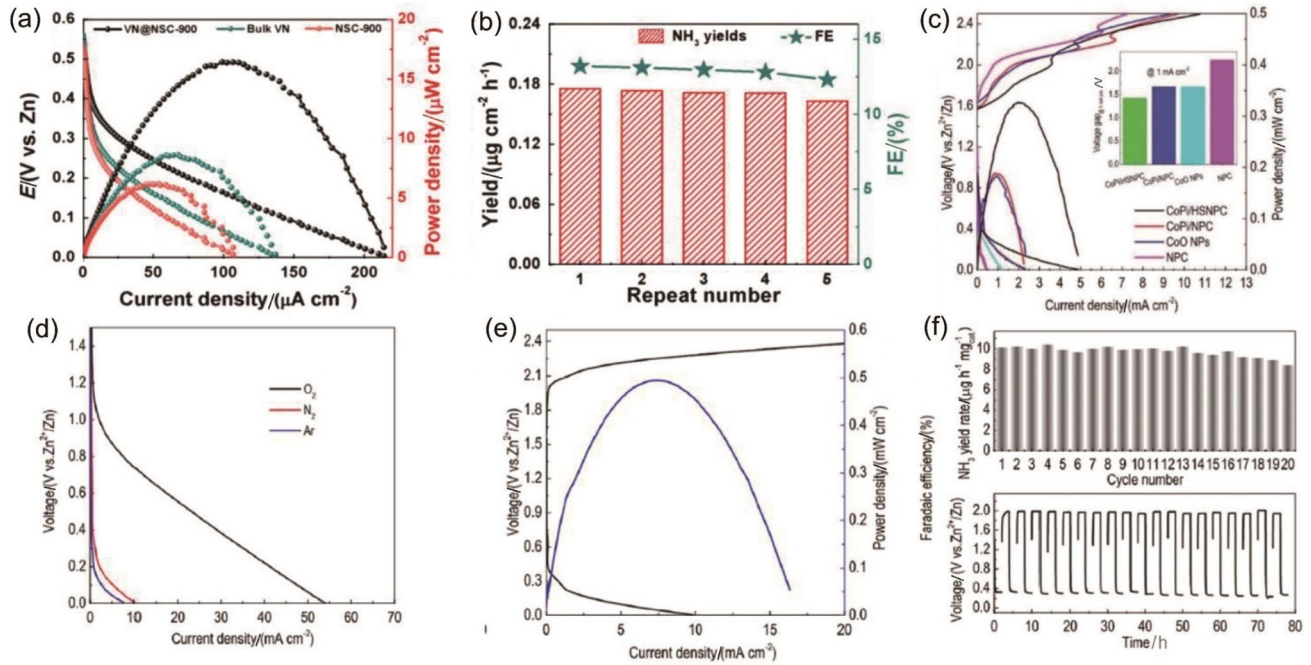

Fig. 22 **a** Polarization curves and power density plots for the VN@NSC-incorporated Zn-N_2 battery. **b** Cycling performance of the Zn-N_2 battery with the VN@NSC cathode. Reprinted with permission from Ref. [49]. Copyright © 2020, Elsevier Ltd. **c** Polarization and power density plots for the Zn-N_2 battery with the CoPi/HSNPC cathode. **d** Polarization curves for the Zn-N_2 battery with the CoPi/HSNPC cathode under different atmospheres. Reprinted with permission from Ref. [32]. Copyright © 2021, Royal Society of Chemistry. **e** Charge−discharge curves and power density plots for the Zn-N_2 battery with the CoPi/NPCS cathode. **f** Cycling performance of the Zn-N_2 battery with the CoPi/NPCS cathode. Reprinted with permission from Ref. [27]. Copyright © 2021, American Chemical Society

$$\text{Discharging (NRR)}: 6H_2O + N_2 + 6e^- \rightarrow 2NH_3 + 6OH^- \quad (10)$$

$$\text{Charging (OER)}: 4OH^- \rightarrow O_2 + H_2O + 4e^- \quad (11)$$

After addressing the drawbacks of nonaqueous Li-N_2, Na-N_2 and Al-N_2 batteries, Wang et al. [30] designed a Zn-N_2 battery with exfoliated niobium disulfide nanosheets (NbS_2 NSs), which showed a promising peak power density of 0.31 mW cm^{-2} in 1.0 M KOH electrolyte (Fig. 21d). In addition, the Zn-N_2 battery with the NbS_2 cathode delivered a stable current density at various potentials, which shows the reliability of the battery performance (Fig. 21e). The coupled Zn-N_2 battery was demonstrated to light up a red LED under a constant N_2 supply, which displays prospects for potential applications (Fig. 21f). Following exfoliated metal dichalcogenides, a novel electrocatalyst design with iron-doped hollow titanium oxide nanospheres (FeHTN) was synthesized as the cathode material for a Zn-N_2 battery [31]. The mechanism of the FeHTN electrocatalyst was similar to that of the human alveolus because the negative pressure of the produced ammonia sucks in the nitrogen gas for further reduction (Fig. 21g). The nanospheres increase the time of stay of the nitrogen molecules in the electrocatalyst, which increases the ammonia yield. The FeHTN-fabricated Zn-N_2 battery exhibited a maximum power density of approximately 27.65 μW cm^{-2} in a 0.1 M KOH electrolyte (Fig. 21h). After coupling three Zn-N_2 batteries, it could light up a white LED, which shows the potential applicability of FeHTN for Zn-N_2 batteries (Fig. 21i).

Incorporating a heterostructure strategy to combine the specific activity of two phases is highly anticipated to achieve boosted electrocatalytic activity. Because of the importance of the heterostructure strategy, Lv et al. [49] synthesized a vanadium nitride nanodot-anchored ultrathin N, S-doped carbon matrix (VN@NSC) and employed it as a cathode for a Zn-N_2 battery. The VN@NSC electrocatalyst performs as a dual-engine mechanism where VN acts as the "capturer" and NSC with defect sites acts as the "converter" for ammonia synthesis. The VN@NSC-fabricated Zn-N_2 batteries exhibited a power density of approximately 16.42 μW cm^{-2} in a 0.1 M KOH electrolyte (Fig. 22a, b).

Consecutively, the group investigated the performance of cobalt phosphate nanospheres (CoPi/HSNPC), which capture N_2 inside their spheres, increasing the chances of reduction [32]. The Zn-N_2 battery with CoPi/HSNPC exhibits a maximum power density of approximately 0.15 mW cm^{-2} and a cell potential of approximately 0.6 V (Fig. 22c, d).CoPi/HSNPC was also evaluated for OER performance, which shows promising applications in the rechargeability of the electrocatalyst. The activity is obviously due to the Co^{2+}

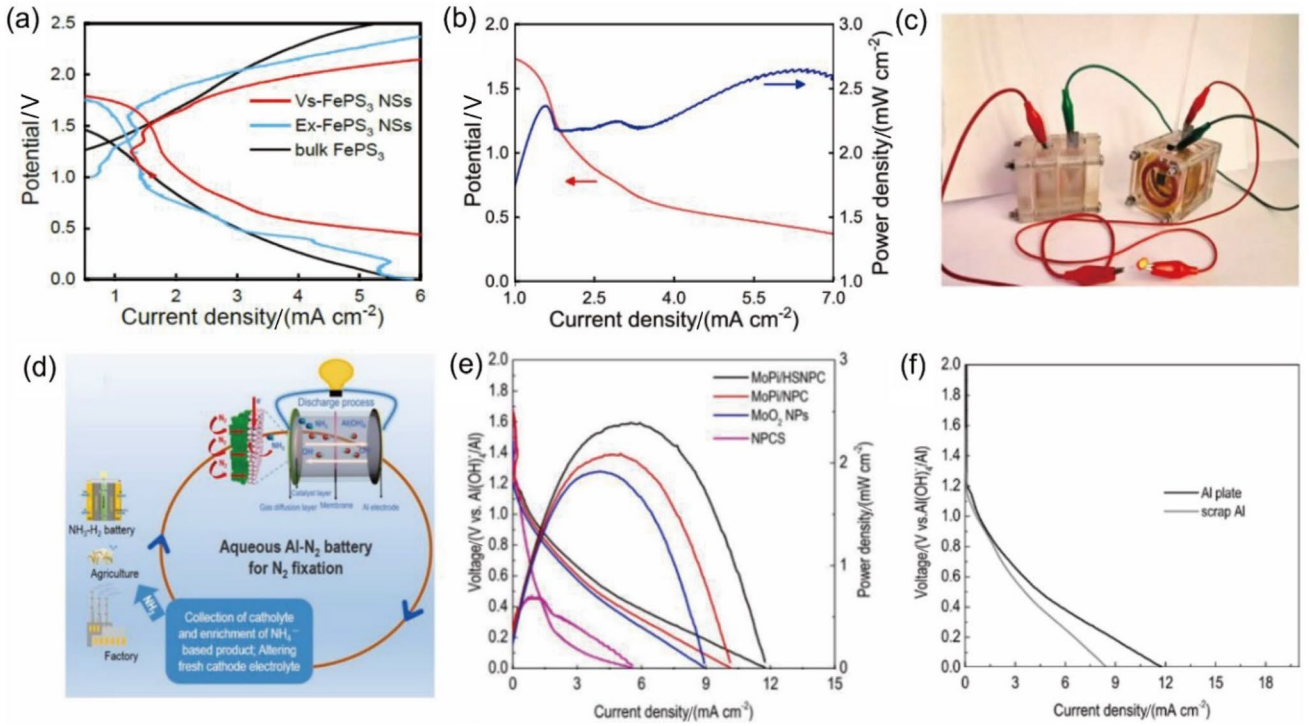

Fig. 23 **a** Charge−discharge curves of the Zn-N_2 battery with the $FePS_3$ electrocatalyst. **b** Polarization and power density plots for the Zn-N_2 battery with the $FePS_3$ catalyst. **c** Optical photograph of the coupled $FePS_3$-fabricated Zn-N_2 battery powering a red LED. Reprinted with permission from Ref. [48]. Copyright © 2020, Elsevier Ltd. **d** Schematic of the aqueous Al-N_2 battery. **e** Polarization curves and power density plots for the Al-N_2 battery with the MoPi/HSNPC cathode. **f** Discharge polarization curves for the Al-N_2 battery with scrap Al metal. Reprinted with permission from Ref. [26]. Copyright © 2021, Elsevier Ltd

redox site that selectively adsorbs N_2 and the phosphorous atom that enhances the electronic conductivity of the electrocatalyst. The spheres efficiently support the mass transfer of the ions that form intermediates during the discharge cycle.

In addition, cobalt phosphate anchored on N-doped carbon nanosheets (CoPi/NPCS) achieves a higher surface area for the interaction of N_2 with the active sites [27]. The CoPi/NPCS-incorporated Zn-N_2 battery in the flow configuration achieved a maximum power density of approximately 0.49 mW cm^{-2} and a cell potential of nearly 0.6 V (Fig. 22e). The battery can withstand a stable current density for longer periods (Fig. 22f). However, the battery under an O_2 atmosphere is found to reduce O_2 more preferably than N_2. The OER performance highlights the potential of the Zn-N_2 battery for rechargeable applications.

To analyse the performance of 2D structures as electrocatalysts, Lv et al. [48] studied 2D porous exfoliated $FePS_3$ nanosheets with rich sulfur vacancies (V_s-$FePS_3$ NS), which exhibit a higher NRR performance. The 2D structure imparts a high surface area for catalytic activity. The Zn-N_2 battery fabricated with V_s-$FePS_3$ NSs exhibits a power density of approximately 2.6 mW cm^{-2} in a 1.0 M KOH electrolyte (Fig. 23a, b).

The Zn-N_2 battery delivers a constant current density for a longer period of time with insignificant changes. The coupled Zn-N_2 battery was used to light a red LED, exhibiting the potential prospects of the Zn-N_2 battery with the $FePS_3$ cathode (Fig. 23c). Following aqueous alkaline Zn-N_2 batteries with various cathode materials, Ren et al. [26] fabricated an alkaline Al-N_2 battery with molybdenum phosphide spheres (MoPi/HSNPC) as the cathode in a 1.0 M KOH electrolyte (Fig. 23d). Previous reports suggest Al corrosion during discharge in alkaline electrolytes, which was overcome by the corrosion-inhibiting anolyte additives of 2 mM Na_2SnO_3, 0.1 mM $In(OH)_3$ and 1.5 mM ZnO. The Al-N_2 battery uses the flow reactor model with a gas diffusion electrode forming a three-phase interface for N_2 reduction. The Al-N_2 battery delivers a peak power density of approximately 2.37 mW cm^{-2} and an FE of approximately 5.06% (Fig. 23e). The Al-N_2 battery finds marvellous applications due to the large availability and lightweight property of the metal. This study also includes an Al-N_2 battery fabricated with anode scrap Al metal, which shows the promising sustainability of the Al-N_2 battery for the future. The battery performance was almost similar, with a current density of nearly 8.46 mA cm^{-2} at 0 V vs. $Al(OH)_4^-$/Al for scrap Al metal (Fig. 23f).

Table 2 Comparison table for various metal-N_2 battery systems. Data are from different referenced resources

S. no	Metal-N_2	Anode	Cathode	Electrolyte	Cell voltage/V	Energy/Power density (mW cm^{-2})	FE/ (%)	References
1	Li-N_2	Li foil	Carbon cloth (CC)	1 M $LiCF_3SO_3$ in tetraethylene glycol dimethyl ether (TEGDME)	1.08	1 248 Wh kg^{-1}	59	[20]
2	Na-N_2	Na metal	α-MnO_2 nanowire	1 M $NaCF_3SO_3$/ TEGDME solution	~2.47	4 900 Wh kg^{-1}	26	[29]
3	Al-N_2	Al metal	Graphene/Pd/CC	AlCl/1-butyl-3-methyl imidazolium chloride	1.46	–	51.2	[47]
4	Zn-N_2	Zn metal	Cu NP	1.0 M KOH	~0.925	0.01	59	[50]
5	Zn-N_2	Zn metal	NbS_2 Nanosheets	1.0 M KOH	2.4	0.31	4.03	[30]
6	Zn-N_2	Zn metal	FeHTN	0.1 M KOH	–	0.027	–	[31]
7	Zn-N_2	Zn metal	VN@ NSC	0.1 M KOH	~0.525	0.016 4	8.6	[49]
8	Zn-N_2	Zn metal	CoPi/HSNPC	1.0 M KOH	0.6	0.15	24.4	[32]
9	Zn-N_2	Zn metal	vs.-$FePS_3$	1.0 M KOH	–	2.6	–	[48]
10	Al-N_2	Al metal	MoPi/HSNPC	1.0 M KOH	1.0	2.37	5.06	[26]
11	Zn-N_2	Zn metal	CoPi/NPCS	1.0 M KOH	0.6	0.49	16.3	[27]

Thus, after serious consideration of various metal-N_2 batteries, Zn-N_2 batteries were considered a reliable and rechargeable aqueous metal-N_2 battery choice. Research was then focused on improving the efficiency of Zn-N_2 batteries by incorporating various electrocatalyst designs as cathode materials, with the electrolyte commonly being alkaline KOH. The Zn-N_2 battery can be fabricated and maintained at ambient temperatures and pressures with very little maintenance and low operational costs. Zn metal is the fourth most abundant element in the Earth's crust and can sufficiently meet the large metal demands for anodes and the prospects of Zn-N_2 batteries in alkaline environments. However, the battery efficiency and stability rely on the type of electrocatalyst used for the Zn-N_2 battery. Moreover, the rechargeability of metal-N_2 batteries has been targeted and shows promising applications in alkaline Zn-N_2 batteries. However, metal-N_2 batteries in aprotic electrolytes exhibit a higher FE than the reported alkaline metal-N_2 batteries, but their scalable application poses a major risk. Al-N_2 batteries exhibit better performance under alkaline environments, but their corrosion under alkaline environments is inevitable and requires corrosion-inhibiting additives [190, 191]. The Zn-N_2 batteries reveal insignificant changes in the charge−discharge cycling performances for nearly 80 h [32] and exhibit stable discharge potential over 2 h [30-32, 48]. Zn-N_2 batteries exhibit relatively low power densities, yet they show potential prospects for development [49, 50]. Considering the performances of metal-N_2 batteries, promising applications of rechargeable aqueous Zn-N_2 batteries for a sustainable future are proposed. Crafting a suitable electrocatalyst with exceptional NRR performance and increased stability can improve Zn-N_2 battery efficiency in the future (Table 2).

7 Conclusion and Perspectives

Developing green ammonia synthesis has a considerable impact on sustainable future energy technologies. Green ammonia synthesis from the electrochemical NRR has convincing applications in various fields, particularly in the future hydrogen economy. Ammonia production by aqueous electrochemical NRR uses water and electricity from renewable resources that are facilitated by electrocatalysts. With the multitude of works relating to the electrochemical NRR, there have not been any state-of-the-art electrocatalysts that set a goal for industrial ammonia synthesis. However, the performance of electrocatalysts is limited by their activity, selectivity, and stability towards efficient electrochemical NRR. Many electrocatalysts have been observed to prefer HER over NRR, and the adsorption of N_2 on some electrocatalysts has been sluggish. Some electrocatalysts even produce N_2H_4, an intermediate product, which sabotages ammonia production.

Research has adopted various strategies by modifying various parameters of the electrochemical NRR cell that are expected to produce ammonia efficiently. The important strategies for increasing ammonia production are (i) increasing the available number of active sites, (ii) suppressing the HER, and (iii) enhancing the conductivity of electrocatalysts. These strategies can be incorporated by engineering the electrocatalysts, modifying the nature of the electrolytes and adopting the LiMEAS procedures to achieve high commercial yields. Recently, novel metal-N_2 batteries have been demonstrated and have found promising applications in the field. However, stability, activity and the controlled environment have been considerable problems to be addressed duly. It is desirable to make

great efforts to increase the activity of electrocatalysts to achieve sustainable and commercial ammonia synthesis and metal-N_2 batteries under ambient conditions. In this review, we summarize some of the current challenges and future directions for the commercialization of NRR and metal-N_2 batteries.

1. *Improving Electrocatalyst Design.* The electrocatalyst in the first case must express long-term stability that provides unperturbed activity and nondegradation of the electrode for long battery cycles. Additionally, the intermediate intercalation or settlements on the surface of the electrocatalysts must be considered, as they may block the active sites for N≡N activation and resist ion flow across the electrode. Modifying the electrocatalysts with vacancies, heterostructure formations, core–shell structures, alloying metals, tuning the morphology and size effects, and electronic modifications by heteroatom dopants are potential strategies for increasing the activity of the electrocatalysts. The electrocatalyst must be sensitive to N_2 adsorption and provide a remarkable activity with maximum FE under NRR electrocatalysis. The electrocatalysts should impose high porosity, increased electronic conductivity, and a nonreactant to the electrolyte that can be incorporated as an electrode to provide faster kinetics and notable efficiency. In addition, the electrocatalysts must be highly conductive to make the active sites readily available for electrons, which may influence the efficient charge−discharge profiles of the metal-N_2 battery later. Thus, high-performance electrocatalysts can be fabricated as bifunctional electrodes in a metal-N_2 battery. The electrocatalyst must be compatible with a longer cycle life and bifunctional activity for rechargeability.
2. *Electrolyte effect.* The electrolytes and the intermediate formation must also be considered to push the working efficiency of the metal-N_2 battery system beyond limits. Tactful control of the N_2 selectivity over protons by modifying the nature of the electrolyte has been a potential route to increasing ammonia yield. The molecular crowding effect, inspired by living cells, has been employed to suppress water molecule migration to the electrode surface. The novel molecular crowding approach is compatible with alkaline, acidic, and neutral solutions. The metal-N_2 battery fabricated with organic/ionic electrolytes has shown promising higher FE and charge−discharge performance. However, because of the operational costs, instability of the electrolytes, and impractical scalability, nonaqueous metal-N_2 batteries are still in their infancy. Metal-N_2 batteries operating in aqueous electrolytes have been the desired application for the current energy-demanding society. Zn-N_2 batteries and Al-N_2 batteries have been fabricated under aqueous electrolytes, which show promising applications for a sustainable future. However, Al metal is corrosive under alkaline environments, which requires corrosion-inhibiting additives to retain the activity. Nevertheless, the Zn-N_2 battery has been the most studied and provides promising applications in the future of rechargeable metal-N_2 batteries under alkaline environments. Metal-N_2 batteries have been found to produce lower ammonia yields, which can be investigated further by electrolyte engineering strategies to enable sustained ammonia synthesis with higher charge−discharge efficiencies.
3. *Metal-N_2 batteries.* Metal-N_2 batteries are still in their infancy and need further improvements for commercial-level battery fabrication. The battery type and its mechanism vary based on the nature of the electrolytes used. Li-N_2, Na-N_2, and Al-N_2 batteries have been reported under aprotic electrolytes and exhibited a higher FE, but the maintenance and operational costs make them less favourable for sustainable application. However, alkaline metal-N_2 batteries in Zn-N_2 and Al-N_2 have shown promising efficiency and considerable power density, which can be further improved to achieve commercialized metal-N_2 batteries. Moreover, Na-N_2 batteries have been used under ambient conditions (NAA performance), which shows promising results for futuristic battery fabrication technology. Detailed studies on Zn-N_2 batteries show better charge−discharge performances with a stable discharge voltage in an aqueous environment. Moreover, Li metal and Na metal cannot be handled in an ambient atmosphere, which shows the tedious fabrication process of the corresponding metal-N_2 batteries. Therefore, it can be inferred that Zn-N_2 batteries with an appropriate electrocatalyst hold more prospects for industrial-scale applications than other candidates.
4. *Rechargeability.* The amount of importance given to the electrocatalyst for NRR during discharge must also be given to the rechargeability of the metal-N_2 batteries. The charging process in an aqueous metal-N_2 battery evolves O_2 following OER by the adsorption of four OH^- ions at the cathode surface. Hence, the counterreaction must also be equally assisted in providing efficient rechargeability of the battery and maintaining long-term cycling. Additionally, the intermediate stability of the electrocatalyst in nonaqueous metal-N_2 batteries and electrolyte media must also be evaluated for long-term storage applications. In addition, aqueous Zn-N_2 batteries show better rechargeable performances than Al-N_2 batteries because of the higher oxidation behaviour of Al ($Al^{3+}/Al = -1.66$ V) compared to Zn metal ($Zn^{2+}/Zn = -0.76$ V). Hence, the Zn-N_2 battery shows promising advantages over other candidates for rechargeability

in ambient aqueous conditions and minimum maintenance, elucidating the versatility of the Zn-N_2 battery in energy storage.

5. *Future study developments.* It is of utmost importance to analyse the catalytic reactions and the side reactions that pose unfavourable conditions in the electrochemical cell. In situ electrochemical and characterization studies and theoretical/simulation studies of the metal-N_2 battery can provide a better understanding of the kinetics of the electrochemical reactions and the transformation of the electrocatalyst surface with respect to time. This understanding can provide a better formulation strategy for the metal-N_2 battery system. Aqueous metal-N_2 batteries have gained attention due to their easy fabrication, corrosion-free environment, and extended battery life. With metal-air batteries gaining substantial updates, it is envisioned that metal-N_2 batteries will be commercialized. To date, metal-N_2 batteries have been tested under a controlled N_2 environment, and future studies must fabricate electrocatalysts tuned to uptake N_2 conversion over O_2 in the ambient atmosphere.

Acknowledgements This work was supported by the National Research Foundation of Korea (NRF) grant funded by the Korean government (MSIT) (No. 2022R1A2C1012419). And this study was supported by the Korea Institute of Energy Technology Evaluation and Planning (KETEP) grant funded by the Korea government (MOTIE) (No. RS-2023-00242227, Clean Hydrogen and Ammonia Innovation Research Center).

Declarations

Conflict of interest All authors declare that there are no competing interests.

Ethical approval Not applicable.

Informed consent Not required.

Statement of human rights Not applicable.

Statement on the welfare of animals Not applicable.

References

1. Roser, M., Ritchie, H., Ortiz-Ospina, E., et al.: World population growth. Our World in Data. https://ourworldindata.org/world-population-growth (2013). Accessed 6 Mar 2023
2. Guo, X.X., Du, H.T., Qu, F.L., et al.: Recent progress in electrocatalytic nitrogen reduction. J. Mater. Chem. A **7**, 3531–3543 (2019). https://doi.org/10.1039/c8ta11201k
3. Laursen, A.B., Varela, A.S., Dionigi, F., et al.: Electrochemical hydrogen evolution: Sabatier's principle and the volcano plot. J. Chem. Educ. **89**, 1595–1599 (2012). https://doi.org/10.1021/ed200818t
4. Lee, K.R., Lee, K.U., Lee, J.W., et al.: Electrochemical oxygen reduction on nitrogen doped graphene sheets in acid media. Electrochem. Commun. **12**, 1052–1055 (2010). https://doi.org/10.1016/j.elecom.2010.05.023
5. Nitopi, S., Bertheussen, E., Scott, S.B., et al.: Progress and perspectives of electrochemical CO_2 reduction on copper in aqueous electrolyte. Chem. Rev. **119**, 7610–7672 (2019). https://doi.org/10.1021/acs.chemrev.8b00705
6. Irabien, A., Alvarez-Guerra, M., Albo, J., et al.: Electrochemical conversion of CO_2 to value-added products. In: Electrochemical Water and Wastewater Treatment, pp. 29–59. Elsevier, Amsterdam (2018), Edited by Martínez-Huitle, C. A., Rodrigo, M. A., Scialdone, O. https://doi.org/10.1016/b978-0-12-813160-2.00002-x
7. Li, W.Y., Li, K., Ye, Y.X., et al.: Efficient electrocatalytic nitrogen reduction to ammonia with aqueous silver nanodots. Commun. Chem. **4**, 10 (2021). https://doi.org/10.1038/s42004-021-00449-7
8. Ghavam, S., Vahdati, M., Grant Wilson, I.A., et al.: Sustainable ammonia production processes. Front. Energy Res. **9**, 580808 (2021). https://doi.org/10.3389/fenrg.2021.580808
9. Hasan, M.H., Mahlia, T.M.I., Mofijur, M., et al.: A comprehensive review on the recent development of ammonia as a renewable energy carrier. Energies **14**, 3732 (2021). https://doi.org/10.3390/en14133732
10. Hinnemann, B., Nørskov, J.K.: Catalysis by enzymes: the biological ammonia synthesis. Top. Catal. **37**, 55–70 (2006). https://doi.org/10.1007/s11244-006-0002-0
11. Wan, Y.C., Xu, J.C., Lv, R.T.: Heterogeneous electrocatalysts design for nitrogen reduction reaction under ambient conditions. Mater. Today **27**, 69–90 (2019). https://doi.org/10.1016/j.mattod.2019.03.002
12. Montoya, J.H., Tsai, C., Vojvodic, A., et al.: The challenge of electrochemical ammonia synthesis: a new perspective on the role of nitrogen scaling relations. Chemsuschem **8**, 2180–2186 (2015). https://doi.org/10.1002/cssc.201500322
13. Singh, A.R., Rohr, B.A., Schwalbe, J.A., et al.: Electrochemical ammonia synthesis: the selectivity challenge. ACS Catal. **7**, 706–709 (2017). https://doi.org/10.1021/acscatal.6b03035
14. Liu, Y.Y., Han, M.M., Xiong, Q.Z., et al.: Ambient ammonia electrosynthesis: dramatically enhanced ambient ammonia electrosynthesis performance by in-operando created Li–S interactions on MoS_2 electrocatalyst. Adv. Energy Mater. **9**, 1970042 (2019). https://doi.org/10.1002/aenm.201970042
15. Wei, X., Pu, M.H., Jin, Y.M., et al.: Efficient electrocatalytic N_2 reduction on three-phase interface coupled in a three-compartment flow reactor for the ambient NH_3 synthesis. ACS Appl. Mater. Interfaces **13**, 21411–21425 (2021). https://doi.org/10.1021/acsami.1c03698
16. Guo, Y., Gu, J.X., Zhang, R., et al.: Molecular crowding effect in aqueous electrolytes to suppress hydrogen reduction reaction and enhance electrochemical nitrogen reduction. Adv. Energy Mater. **11**, 2101699 (2021). https://doi.org/10.1002/aenm.202101699

17. Shen, P., Li, X.C., Luo, Y.J., et al.: High-efficiency N_2 electroreduction enabled by Se-vacancy-rich WSe_{2-x} in water-in-salt electrolytes. ACS Nano **16**, 7915–7925 (2022). https://doi.org/10.1021/acsnano.2c00596
18. Verma, S., Mishra, S., Gaur, A., et al.: A comprehensive review on energy storage in hybrid electric vehicle. J. Traffic Transp. Eng. Engl. Ed. **8**, 621–637 (2021). https://doi.org/10.1016/j.jtte.2021.09.001
19. Kolokotsa, D., Kampelis, N., Mavrigiannaki, A., et al.: On the integration of the energy storage in smart grids: technologies and applications. Energy Storage **1**, e50 (2019). https://doi.org/10.1002/est2.50
20. Ma, J.L., Bao, D., Shi, M.M., et al.: Reversible nitrogen fixation based on a rechargeable lithium-nitrogen battery for energy storage. Chem **2**, 525–532 (2017). https://doi.org/10.1016/j.chempr.2017.03.016
21. Ma, W.Q., Liu, X.Z., Li, C., et al.: Rechargeable Al-CO_2 batteries for reversible utilization of CO_2. Adv. Mater. **30**, 1801152 (2018). https://doi.org/10.1002/adma.201801152
22. Sun, X.Y., Hou, Z.P., He, P., et al.: Recent advances in rechargeable Li-CO_2 batteries. Energy Fuels **35**, 9165–9186 (2021). https://doi.org/10.1021/acs.energyfuels.1c00635
23. Park, H., Lim, H.D., Lim, H.K., et al.: High-efficiency and high-power rechargeable lithium–sulfur dioxide batteries exploiting conventional carbonate-based electrolytes. Nat. Commun. **8**, 14989 (2017). https://doi.org/10.1038/ncomms14989
24. Tong, Z.Z., Wang, S.B., Fang, M.H., et al.: Na-CO_2 battery with NASICON-structured solid-state electrolyte. Nano Energy **85**, 105972 (2021). https://doi.org/10.1016/j.nanoen.2021.105972
25. Kwak, W.J., Rosy, Sharon, D., et al.: Lithium-oxygen batteries and related systems: potential, status, and future. Chem. Rev. **120**, 6626–6683 (2020). https://doi.org/10.1021/acs.chemrev.9b00609
26. Ren, J.T., Chen, L., Wang, H.Y., et al.: Aqueous Al-N_2 battery assembled by hollow molybdenum phosphate microspheres for simultaneous NH_3 production and power generation. Chem. Eng. J. **418**, 129447 (2021). https://doi.org/10.1016/j.cej.2021.129447
27. Ren, J.T., Chen, L., Wang, H.Y., et al.: Aqueous rechargeable Zn-N_2 battery assembled by bifunctional cobalt phosphate nanocrystals-loaded carbon nanosheets for simultaneous NH_3 production and power generation. ACS Appl. Mater. Interfaces **13**, 12106–12117 (2021). https://doi.org/10.1021/acsami.1c00570
28. Li, Y.G., Dai, H.J.: Recent advances in zinc-air batteries. Chem. Soc. Rev. **43**, 5257–5275 (2014). https://doi.org/10.1039/c4cs00015c
29. Ge, B.C., Wang, Y.Y., Sun, Y., et al.: A proof-of-concept of Na-N_2 rechargeable battery. Energy Storage Mater. **23**, 733–740 (2019). https://doi.org/10.1016/j.ensm.2019.02.018
30. Wang, H., Si, J.C., Zhang, T.Y., et al.: Exfoliated metallic niobium disulfate nanosheets for enhanced electrochemical ammonia synthesis and Zn-N_2 battery. Appl. Catal. B Environ. **270**, 118892 (2020). https://doi.org/10.1016/j.apcatb.2020.118892
31. Lv, X.W., Liu, X.L., Gao, L.J., et al.: Iron-doped titanium dioxide hollow nanospheres for efficient nitrogen fixation and Zn-N_2 aqueous batteries. J. Mater. Chem. A **9**, 4026–4035 (2021). https://doi.org/10.1039/d0ta11244e
32. Ren, J.T., Chen, L., Liu, Y.P., et al.: Hollow cobalt phosphate microspheres for sustainable electrochemical ammonia production through rechargeable Zn-N_2 batteries. J. Mater. Chem. A **9**, 11370–11380 (2021). https://doi.org/10.1039/d1ta01144h
33. Zhai, P.L., Xia, M.Y., Wu, Y.Z., et al.: Engineering single-atomic ruthenium catalytic sites on defective nickel-iron layered double hydroxide for overall water splitting. Nat. Commun. **12**, 4587 (2021). https://doi.org/10.1038/s41467-021-24828-9
34. Choi, C., Back, S., Kim, N.Y., et al.: Suppression of hydrogen evolution reaction in electrochemical N_2 reduction using single-atom catalysts: a computational guideline. ACS Catal. **8**, 7517–7525 (2018). https://doi.org/10.1021/acscatal.8b00905
35. Skúlason, E., Bligaard, T., Gudmundsdóttir, S., et al.: A theoretical evaluation of possible transition metal electro-catalysts for N_2 reduction. Phys. Chem. Chem. Phys. **14**, 1235–1245 (2012). https://doi.org/10.1039/c1cp22271f
36. Fu, C.H., Luo, L.X., Yang, L.J., et al.: Theoretical exploration of the thermodynamic process competition between NRR and HER on transition-metal-doped CoP (101) facets. J. Phys. Chem. C **125**, 17051–17057 (2021). https://doi.org/10.1021/acs.jpcc.1c04420
37. Yuan, M.L., Bai, Y.L., Zhang, J.X., et al.: Work function regulation of nitrogen-doped carbon nanotubes triggered by metal nanoparticles for efficient electrocatalytic nitrogen fixation. J. Mater. Chem. A **8**, 26066–26074 (2020). https://doi.org/10.1039/d0ta08914a
38. Katayama, A., Inomata, T., Ozawa, T., et al.: Electrochemical conversion of dinitrogen to ammonia induced by a metal complex–supported ionic liquid. Electrochem. Commun. **67**, 6–10 (2016). https://doi.org/10.1016/j.elecom.2016.03.001
39. Pappenfus, T.M., Lee, K.M., Thoma, L.M., et al.: Wind to ammonia: electrochemical processes in room temperature ionic liquids. ECS Trans. **16**, 89–93 (2009). https://doi.org/10.1149/1.3159311
40. Cai, X.Y., Fu, C.H., Iriawan, H., et al.: Lithium-mediated electrochemical nitrogen reduction: mechanistic insights to enhance performance. iScience **24**, 103105 (2021). https://doi.org/10.1016/j.isci.2021.103105
41. Schwalbe, J.A., Statt, M.J., Chosy, C., et al.: A combined theory-experiment analysis of the surface species in lithium-mediated NH_3 electrosynthesis. ChemElectroChem **7**, 1542–1549 (2020). https://doi.org/10.1002/celc.201902124
42. Zhou, F.L., Azofra, L.M., Ali, M., et al.: Electro-synthesis of ammonia from nitrogen at ambient temperature and pressure in ionic liquids. Energy Environ. Sci. **10**, 2516–2520 (2017). https://doi.org/10.1039/c7ee02716h
43. Lazouski, N., Schiffer, Z.J., Williams, K., et al.: Understanding continuous lithium-mediated electrochemical nitrogen reduction. Joule **3**, 1127–1139 (2019). https://doi.org/10.1016/j.joule.2019.02.003
44. Hu, C.Y., Chen, X., Jin, J.B., et al.: Surface plasmon enabling nitrogen fixation in pure water through a dissociative mechanism under mild conditions. J. Am. Chem. Soc. **141**, 7807–7814 (2019). https://doi.org/10.1021/jacs.9b01375
45. John, J., Lee, D.K., Sim, U.: Photocatalytic and electrocatalytic approaches towards atmospheric nitrogen reduction to ammonia under ambient conditions. Nano Convergence **6**, 1–16 (2019). https://doi.org/10.1186/s40580-019-0182-5
46. Abghoui, Y., Garden, A.L., Hlynsson, V.F., et al.: Enabling electrochemical reduction of nitrogen to ammonia at ambient conditions through rational catalyst design. Phys. Chem. Chem. Phys. **17**, 4909–4918 (2015). https://doi.org/10.1039/c4cp04838e
47. Guo, Y., Yang, Q., Wang, D.H., et al.: A rechargeable Al-N_2 battery for energy storage and highly efficient N_2 fixation. Energy Environ. Sci. **13**, 2888–2895 (2020). https://doi.org/10.1039/d0ee01241f
48. Wang, H., Li, Z.J., Li, Y., et al.: An exfoliated iron phosphorus trisulfide nanosheet with rich sulfur vacancy for efficient dinitrogen fixation and Zn-N_2 battery. Nano Energy **81**, 105613 (2021). https://doi.org/10.1016/j.nanoen.2020.105613
49. Lv, X.W., Liu, Y.P., Wang, Y.S., et al.: Encapsulating vanadium nitride nanodots into N, S-codoped graphitized carbon for synergistic electrocatalytic nitrogen reduction and aqueous Zn-N_2

battery. Appl. Catal. B Environ. **280**, 119434 (2021). https://doi.org/10.1016/j.apcatb.2020.119434
50. Du, C., Gao, Y.J., Wang, J.G., et al.: Achieving 59% faradaic efficiency of the N_2 electroreduction reaction in an aqueous Zn-N_2 battery by facilely regulating the surface mass transport on metallic copper. Chem. Commun. **55**, 12801–12804 (2019). https://doi.org/10.1039/c9cc05978d
51. Janani, G., Chae, Y.J., Surendran, S., et al.: Rational design of spinel oxide nanocomposites with tailored electrochemical oxygen evolution and reduction reactions for zinc-air batteries. Appl. Sci. **10**, 3165 (2020). https://doi.org/10.3390/app10093165
52. Fabbri, E., Schmidt, T.J.: Oxygen evolution reaction: the enigma in water electrolysis. ACS Catal. **8**, 9765–9774 (2018). https://doi.org/10.1021/acscatal.8b02712
53. Kim, D., Surendran, S., Lim, Y., et al.: Spinel-type Ni_2GeO_4 electrocatalyst for electrochemical ammonia synthesis via nitrogen reduction reaction under ambient conditions. Int. J. Energy Res. **46**, 4119–4129 (2022). https://doi.org/10.1002/er.7414
54. Carmo, M., Stolten, D.: Energy storage using hydrogen produced from excess renewable electricity. In: Science and Engineering of Hydrogen-Based Energy Technologies, pp. 165–199, Elsevier, Amsterdam (2019), Edited by Paulo Emilio V. de Miranda. https://doi.org/10.1016/b978-0-12-814251-6.00004-6
55. Suryanto, B.H.R., Du, H.L., Wang, D.B., et al.: Challenges and prospects in the catalysis of electroreduction of nitrogen to ammonia. Nat. Catal. **2**, 290–296 (2019). https://doi.org/10.1038/s41929-019-0252-4
56. Khalil, I.E., Xue, C., Liu, W.J., et al.: The role of defects in metal-organic frameworks for nitrogen reduction reaction: when defects switch to features. Adv. Funct. Mater. **31**, 2010052 (2021). https://doi.org/10.1002/adfm.202010052
57. Chanda, D., Xing, R.M., Xu, T., et al.: Electrochemical nitrogen reduction: recent progress and prospects. Chem. Commun. **57**, 7335–7349 (2021). https://doi.org/10.1039/d1cc01451j
58. Zhao, X., Yang, Z.Q., Kuklin, A.V., et al.: Potassium ions promote electrochemical nitrogen reduction on nano-Au catalysts triggered by bifunctional boron supramolecular assembly. J. Mater. Chem. A **8**, 13086–13094 (2020). https://doi.org/10.1039/d0ta04580b
59. Liu, H.M., Guijarro, N., Luo, J.S.: The pitfalls in electrocatalytic nitrogen reduction for ammonia synthesis. J. Energy Chem. **61**, 149–154 (2021). https://doi.org/10.1016/j.jechem.2021.01.039
60. Ooka, H., Huang, J., Exner, K.S.: The Sabatier principle in electrocatalysis: basics, limitations, and extensions. Front. Energy Res. **9**, 654460 (2021). https://doi.org/10.3389/fenrg.2021.654460
61. Dražević, E., Skúlason, E.: Are there any overlooked catalysts for electrochemical NH_3 synthesis: new insights from analysis of thermochemical data. Science **23**, 101803 (2020). https://doi.org/10.1016/j.isci.2020.101803
62. Trasatti, S.: Work function, electronegativity, and electrochemical behaviour of metals. J. Electroanal. Chem. Interfacial Electrochem. **39**, 163–184 (1972). https://doi.org/10.1016/s0022-0728(72)80485-6
63. Wei, Z.X., Feng, Y.Z., Ma, J.M.: Co-doped graphene edge for enhanced N_2-to-NH_3 conversion. J. Energy Chem. **48**, 322–327 (2020). https://doi.org/10.1016/j.jechem.2020.02.014
64. Wei, Z.X., He, J., Yang, Y.L., et al.: Fe, V-co-doped C_2N for electrocatalytic N_2-to-NH_3 conversion. J. Energy Chem. **53**, 303–308 (2021). https://doi.org/10.1016/j.jechem.2020.04.014
65. Lazouski, N., Chung, M., Williams, K., et al.: Non-aqueous gas diffusion electrodes for rapid ammonia synthesis from nitrogen and water-splitting-derived hydrogen. Nat. Catal. **3**, 463–469 (2020). https://doi.org/10.1038/s41929-020-0455-8
66. Andersen, S.Z., Statt, M.J., Bukas, V.J., et al.: Increasing stability, efficiency, and fundamental understanding of lithium-mediated electrochemical nitrogen reduction. Energy Environ. Sci. **13**, 4291–4300 (2020). https://doi.org/10.1039/d0ee02246b
67. Gao, L.F., Cao, Y., Wang, C., et al.: Domino effect: gold electrocatalyzing lithium reduction to accelerate nitrogen fixation. Angewandte Chemie Int. Ed. **60**, 5257–5261 (2021). https://doi.org/10.1002/anie.202015496
68. Hao, R., Sun, W.M., Liu, Q., et al.: Efficient electrochemical nitrogen fixation over isolated Pt sites. Small **16**, 2000015 (2020). https://doi.org/10.1002/smll.202000015
69. Wang, X.J., Luo, M., Lan, J., et al.: Nanoporous intermetallic Pd_3Bi for efficient electrochemical nitrogen reduction. Adv. Mater. **33**, 2007733 (2021). https://doi.org/10.1002/adma.202007733
70. He, H.M., Zhu, Q.Q., Yan, Y., et al.: Metal-organic framework supported Au nanoparticles with organosilicone coating for high-efficiency electrocatalytic N_2 reduction to NH_3. Appl. Catal. B Environ. **302**, 120840 (2022). https://doi.org/10.1016/j.apcatb.2021.120840
71. Zhang, J., Ji, Y.J., Wang, P.T., et al.: Adsorbing and activating N_2 on heterogeneous Au–Fe_3O_4 nanoparticles for N_2 fixation. Adv. Funct. Mater. **30**, 1906579 (2020). https://doi.org/10.1002/adfm.201906579
72. Liu, H.M., Han, S.H., Zhao, Y., et al.: Surfactant-free atomically ultrathin rhodium nanosheet nanoassemblies for efficient nitrogen electroreduction. J. Mater. Chem. A **6**, 3211–3217 (2018). https://doi.org/10.1039/c7ta10866d
73. Wang, X.Q., Wang, W.Y., Qiao, M., et al.: Atomically dispersed Au_1 catalyst towards efficient electrochemical synthesis of ammonia. Sci. Bull. **63**, 1246–1253 (2018). https://doi.org/10.1016/j.scib.2018.07.005
74. Geng, Z.G., Liu, Y., Kong, X.D., et al.: Achieving a record-high yield rate of 120.9 $\mu g_{NH_3}\ mg_{cat.}^{-1}\ h^{-1}$ for N_2 electrochemical reduction over Ru single-atom catalysts. Adv. Mater. **30**, 1803498 (2018). https://doi.org/10.1002/adma.201803498
75. Yu, H., Wang, Z., Tian, W., et al.: Boosting electrochemical nitrogen fixation by mesoporous Rh film with boron and sulfur co-doping. Mater. Today Energy **20**, 100681 (2021). https://doi.org/10.1016/j.mtener.2021.100681
76. Li, G.J., Zhang, W.S., Luo, N., et al.: Bimetallic nanocrystals: Structure, controllable synthesis and applications in catalysis, energy and sensing. Nanomaterials **11**, 1926 (2021). https://doi.org/10.3390/nano11081926
77. Sun, C., Mu, Y.X., Wang, Y.X.: A Pd/MnO_2 electrocatalyst for nitrogen reduction to ammonia under ambient conditions. Catalysts **10**, 802 (2020). https://doi.org/10.3390/catal10070802
78. Hill, J.R., Freeman, C.M., Rossouw, M.H.: Understanding γ-MnO_2 by molecular modeling. J. Solid State Chem. **177**, 165–175 (2004). https://doi.org/10.1016/S0022-4596(03)00393-1
79. Ologunagba, D., Kattel, S.: Transition metal oxynitride catalysts for electrochemical reduction of nitrogen to ammonia. Mater. Adv. **2**, 1263–1270 (2021). https://doi.org/10.1039/d0ma00849d
80. Jin, H.Y., Li, L.Q., Liu, X., et al.: Nitrogen vacancies on 2D layered W_2N_3: a stable and efficient active site for nitrogen reduction reaction. Adv. Mater. **31**, 1902709 (2019). https://doi.org/10.1002/adma.201902709
81. Zhang, C., Wang, D., Wan, Y.C., et al.: Vanadium carbide with periodic anionic vacancies for effective electrocatalytic nitrogen reduction. Mater. Today **40**, 18–25 (2020). https://doi.org/10.1016/j.mattod.2020.04.031
82. Zhang, L., Ji, X.Q., Ren, X., et al.: Electrochemical ammonia synthesis via nitrogen reduction reaction on a MoS_2 catalyst: theoretical and experimental studies. Adv. Mater. **30**, 1800191 (2018). https://doi.org/10.1002/adma.201800191
83. Zhang, J., Ling, C.Y., Zang, W.J., et al.: Boosted electrochemical ammonia synthesis by high-percentage metallic transition

metal dichalcogenide quantum dots. Nanoscale **12**, 10964–10971 (2020). https://doi.org/10.1039/d0nr01409e
84. Han, Y., Cai, W.W., Wu, X.K., et al.: Electrocatalytic nitrogen fixation on metal tellurides boosted by multiple promoted-synergetic effects of telluride. Cell Rep. Phys. Sci. **1**, 100232 (2020). https://doi.org/10.1016/j.xcrp.2020.100232
85. Zhao, L., Liu, X.J., Zhang, S., et al.: Rational design of bimetallic $Rh_{0.6}Ru_{0.4}$ nanoalloys for enhanced nitrogen reduction electrocatalysis under mild conditions. J. Mater. Chem. A **9**, 259–263 (2021). https://doi.org/10.1039/d0ta09099a
86. Zhang, Y.Z., Hu, J., Zhang, C.X., et al.: Bimetallic Mo–Co nanoparticles anchored on nitrogen-doped carbon for enhanced electrochemical nitrogen fixation. J. Mater. Chem. A **8**, 9091–9098 (2020). https://doi.org/10.1039/d0ta01565b
87. Johnson, D., Hunter, B., Christie, J., et al.: Ti_2N nitride MXene evokes the Mars-van Krevelen mechanism to achieve high selectivity for nitrogen reduction reaction. Sci. Rep. **12**, 657 (2022). https://doi.org/10.1038/s41598-021-04640-7
88. Qi, S.Y., Fan, Y.C., Zhao, L.L., et al.: Two-dimensional transition metal borides as highly efficient N_2 fixation catalysts. Appl. Surf. Sci. **536**, 147742 (2021). https://doi.org/10.1016/j.apsusc.2020.147742
89. Wang, J.L., Kang, S.H., Zhu, X.G., et al.: Highly ordered Nb_2O_5 nanochannel film with rich oxygen vacancies for electrocatalytic N_2 reduction: inactivation and regeneration of electrode. Chin. Chem. Lett. **32**, 2833–2836 (2021). https://doi.org/10.1016/j.cclet.2021.01.020
90. Cong, M.Y., Chen, X.Y., Xia, K., et al.: Selective nitrogen reduction to ammonia on iron porphyrin-based single-site metal-organic frameworks. J. Mater. Chem. A **9**, 4673–4678 (2021). https://doi.org/10.1039/d0ta08741f
91. Jiang, M.H., Han, L.K., Peng, P., et al.: Quasi-phthalocyanine conjugated covalent organic frameworks with nitrogen-coordinated transition metal centers for high-efficiency electrocatalytic ammonia synthesis. Nano Lett. **22**, 372–379 (2022). https://doi.org/10.1021/acs.nanolett.1c04009
92. Li, B.Q., Zhang, S.Y., Wang, B., et al.: A porphyrin covalent organic framework cathode for flexible Zn-air batteries. Energy Environ. Sci. **11**, 1723–1729 (2018). https://doi.org/10.1039/c8ee00977e
93. Zhang, Y.C., Wu, Y., Liu, Y.P., et al.: Flexible and freestanding heterostructures based on COF-derived N-doped porous carbon and two-dimensional MXene for all-solid-state lithium-sulfur batteries. Chem. Eng. J. **428**, 131040 (2022). https://doi.org/10.1016/j.cej.2021.131040
94. Han, L.L., Liu, X.J., Chen, J.P., et al.: Atomically dispersed molybdenum catalysts for efficient ambient nitrogen fixation. Angew. Chem. Int. Ed. **58**, 2321–2325 (2019). https://doi.org/10.1002/anie.201811728
95. Wang, X., Wu, D., Liu, S., et al.: Folic acid self-assembly enabling manganese single-atom electrocatalyst for selective nitrogen reduction to ammonia. Nano-Micro Lett. **13**, 125 (2021). https://doi.org/10.1007/s40820-021-00651-1
96. Wu, Z.Y., Karamad, M., Yong, X., et al.: Electrochemical ammonia synthesis via nitrate reduction on Fe single atom catalyst. Nat. Commun. **12**, 2870 (2021). https://doi.org/10.1038/s41467-021-23115-x
97. Yan, H., Su, C.L., He, J., et al.: Single-atom catalysts and their applications in organic chemistry. J. Mater. Chem. A **6**, 8793–8814 (2018). https://doi.org/10.1039/c8ta01940a
98. Ao, K.L., Shi, J.H., Zhang, X.Y., et al.: Tuning oxygen vacancies in spinel nanosheets for binder-free oxygen cathodes with superior catalytic activity in zinc-air batteries. J. Power Sources **521**, 230918 (2022). https://doi.org/10.1016/j.jpowsour.2021.230918
99. Chen, X.Y., Li, K., Yang, X.X., et al.: Oxygen vacancy engineering of calcium cobaltate: a nitrogen fixation electrocatalyst at ambient condition in neutral electrolyte. Nano Res. **14**, 501–506 (2021). https://doi.org/10.1007/s12274-020-3043-y
100. Xiao, L., Zhu, S.L., Liang, Y.Q., et al.: Nanoporous nickel–molybdenum oxide with an oxygen vacancy for electrocatalytic nitrogen fixation under ambient conditions. ACS Appl. Mater. Interfaces **13**, 30722–30730 (2021). https://doi.org/10.1021/acsami.1c07613
101. Wen, L.L., Li, X.Y., Zhang, R., et al.: Oxygen vacancy engineering of MOF-derived Zn-doped Co_3O_4 nanopolyhedrons for enhanced electrochemical nitrogen fixation. ACS Appl. Mater. Interfaces **13**, 14181–14188 (2021). https://doi.org/10.1021/acsami.0c22767
102. Cheng, S., Gao, Y.J., Yan, Y.L., et al.: Oxygen vacancy enhancing mechanism of nitrogen reduction reaction property in Ru/TiO_2. J. Energy Chem. **39**, 144–151 (2019). https://doi.org/10.1016/j.jechem.2019.01.020
103. Lv, C.D., Yan, C.S., Chen, G., et al.: An amorphous noble-metal-free electrocatalyst that enables nitrogen fixation under ambient conditions. Angew. Chem. Int. Ed. **57**, 6073–6076 (2018). https://doi.org/10.1002/anie.201801538
104. Chu, K.B., Liu, F.Z., Zhu, J.W., et al.: A general strategy to boost electrocatalytic nitrogen reduction on perovskite oxides via the oxygen vacancies derived from A-site deficiency. Adv. Energy Mater. **11**, 2003799 (2021). https://doi.org/10.1002/aenm.202003799
105. Liu, W.J., Bao, J., Xu, L., et al.: $NiCo_2O_4$ ultrathin nanosheets with oxygen vacancies as bifunctional electrocatalysts for Zn-air battery. Appl. Surf. Sci. **478**, 552–559 (2019). https://doi.org/10.1016/j.apsusc.2019.01.243
106. Qi, Z.C., Xiong, T., Chen, T., et al.: Harnessing oxygen vacancy in V_2O_5 as high performing aqueous zinc-ion battery cathode. J. Alloys Compd. **870**, 159403 (2021). https://doi.org/10.1016/j.jallcom.2021.159403
107. Guo, W.H., Liang, Z.B., Tang, Y.Q., et al.: Understanding the lattice nitrogen stability and deactivation pathways of cubic CrN nanoparticles in the electrochemical nitrogen reduction reaction. J. Mater. Chem. A **9**, 8568–8575 (2021). https://doi.org/10.1039/d0ta11727g
108. Yang, X., Nash, J., Anibal, J., et al.: Mechanistic insights into electrochemical nitrogen reduction reaction on vanadium nitride nanoparticles. J. Am. Chem. Soc. **140**, 13387–13391 (2018). https://doi.org/10.1021/jacs.8b08379
109. Du, H.L., Gengenbach, T.R., Hodgetts, R., et al.: Critical assessment of the electrocatalytic activity of vanadium and niobium nitrides toward dinitrogen reduction to ammonia. ACS Sustain. Chem. Eng. **7**, 6839–6850 (2019). https://doi.org/10.1021/acssuschemeng.8b06163
110. Zhang, X.P., Kong, R.M., Du, H.T., et al.: Highly efficient electrochemical ammonia synthesis via nitrogen reduction reactions on a VN nanowire array under ambient conditions. Chem. Commun. **54**, 5323–5325 (2018). https://doi.org/10.1039/c8cc00459e
111. Ren, X., Cui, G.W., Chen, L., et al.: Electrochemical N_2 fixation to NH_3 under ambient conditions: Mo_2N nanorod as a highly efficient and selective catalyst. Chem. Commun. **54**, 8474–8477 (2018). https://doi.org/10.1039/c8cc03627f
112. Yesudoss, D.K., Lee, G., Shanmugam, S.: Strong catalyst support interactions in defect-rich γ-Mo_2N nanoparticles loaded 2D-h-BN hybrid for highly selective nitrogen reduction reaction. Appl. Catal. B Environ. **287**, 119952 (2021). https://doi.org/10.1016/j.apcatb.2021.119952
113. Ye, T.N., Park, S.W., Lu, Y.F., et al.: Contribution of nitrogen vacancies to ammonia synthesis over metal nitride catalysts. J. Am. Chem. Soc. **142**, 14374–14383 (2020). https://doi.org/10.1021/jacs.0c06624

114. Bligaard, T., Nørskov, J.K.: Ligand effects in heterogeneous catalysis and electrochemistry. Electrochim. Acta **52**, 5512–5516 (2007). https://doi.org/10.1016/j.electacta.2007.02.041
115. Gao, Q.S., Zhang, W.B., Shi, Z.P., et al.: Noble-metal-free electrocatalysts: structural design and electronic modulation of transition-metal-carbide electrocatalysts toward efficient hydrogen evolution. Adv. Mater. **31**, 1970009 (2019). https://doi.org/10.1002/adma.201970009
116. Sun, S.F., Zhou, X., Cong, B.W., et al.: Tailoring the d-band centers endows $(Ni_xFe_{1-x})_2P$ nanosheets with efficient oxygen evolution catalysis. ACS Catal. **10**, 9086–9097 (2020). https://doi.org/10.1021/acscatal.0c01273
117. Ramaiyan, K.P., Ozden, S., Maurya, S., et al.: Molybdenum carbide electrocatalysts for electrochemical synthesis of ammonia from nitrogen: activity and stability. J. Electrochem. Soc. **167**, 044506 (2020). https://doi.org/10.1149/1945-7111/ab7097
118. Peng, M., Qiao, Y.J., Luo, M., et al.: Bioinspired Fe_3C@C as highly efficient electrocatalyst for nitrogen reduction reaction under ambient conditions. ACS Appl. Mater. Interfaces **11**, 40062–40068 (2019). https://doi.org/10.1021/acsami.9b14143
119. Cheng, H., Ding, L.X., Chen, G.F., et al.: Nitrogen reduction reaction: molybdenum carbide nanodots enable efficient electrocatalytic nitrogen fixation under ambient conditions. Adv. Mater. **30**, 1870350 (2018). https://doi.org/10.1002/adma.201870350
120. Yu, G.S., Guo, H.R., Kong, W.H., et al.: Electrospun TiC/C nanofibers for ambient electrocatalytic N_2 reduction. J. Mater. Chem. A **7**, 19657–19661 (2019). https://doi.org/10.1039/c9ta07096f
121. Ma, L.Y., Li, Y.J., Xu, Y.H., et al.: Two-dimensional transition metal dichalcogenides for electrocatalytic nitrogen fixation to ammonia: advances, challenges and perspectives: a mini review. Electrochem. Commun. **125**, 107002 (2021). https://doi.org/10.1016/j.elecom.2021.107002
122. Chen, S.R., Liu, X., Xiong, J.B., et al.: Defect and interface engineering in metal sulfide catalysts for the electrocatalytic nitrogen reduction reaction: a review. J. Mater. Chem. A **10**, 6927–6949 (2022). https://doi.org/10.1039/d2ta00070a
123. Zhao, L., Xiong, Y.Y., Wang, X.X., et al.: Shearing sulfur edges of VS_2 electrocatalyst enhances its nitrogen reduction performance. Small **18**, 2106939 (2022). https://doi.org/10.1002/smll.202106939
124. Li, H., Shin, K., Henkelman, G.: Effects of ensembles, ligand, and strain on adsorbate binding to alloy surfaces. J. Chem. Phys. **149**, 174705 (2018). https://doi.org/10.1063/1.5053894
125. Fang, Z.W., Wu, P., Qian, Y.M., et al.: Gel-derived amorphous bismuth–nickel alloy promotes electrocatalytic nitrogen fixation via optimizing nitrogen adsorption and activation. Angew. Chem. Int. Ed. **60**, 4275–4281 (2021). https://doi.org/10.1002/anie.202014302
126. Li, W.X., Fang, W., Wu, C., et al.: Bimetal–MOF nanosheets as efficient bifunctional electrocatalysts for oxygen evolution and nitrogen reduction reaction. J. Mater. Chem. A **8**, 3658–3666 (2020). https://doi.org/10.1039/c9ta13473e
127. Sun, Y., Wang, Y., Li, H., et al.: Main group metal elements for ambient-condition electrochemical nitrogen reduction. J. Energy Chem. **62**, 51–70 (2021). https://doi.org/10.1016/j.jechem.2021.03.001
128. Sebastian, M., Das, S., Gopalan, N.K.: Nitrogen reduction reaction under ambient conditions by $K_3Ti_8O_{17}$ nanorod electrocatalyst. Sustain. Energy Fuels **6**, 1519–1528 (2022). https://doi.org/10.1039/d1se01932e
129. Chen, G.F., Cao, X.R., Wu, S.Q., et al.: Ammonia electrosynthesis with high selectivity under ambient conditions via a Li^+ incorporation strategy. J. Am. Chem. Soc. **139**, 9771–9774 (2017). https://doi.org/10.1021/jacs.7b04393
130. Li, C.B., Yu, J.L., Yang, L., et al.: Spinel $LiMn_2O_4$ nanofiber: an efficient electrocatalyst for N_2 reduction to NH_3 under ambient conditions. Inorg. Chem. **58**, 9597–9601 (2019). https://doi.org/10.1021/acs.inorgchem.9b01707
131. Utomo, W.P., Leung, M.K.H., Yin, Z.Y., et al.: Advancement of bismuth-based materials for electrocatalytic and photo(electro) catalytic ammonia synthesis. Adv. Funct. Mater. **32**, 2106713 (2022). https://doi.org/10.1002/adfm.202106713
132. Li, L.Q., Tang, C., Xia, B.Q., et al.: Two-dimensional mosaic bismuth nanosheets for highly selective ambient electrocatalytic nitrogen reduction. ACS Catal. **9**, 2902–2908 (2019). https://doi.org/10.1021/acscatal.9b00366
133. Gogotsi, Y., Anasori, B.: The rise of MXenes. ACS Nano **13**, 8491–8494 (2019). https://doi.org/10.1021/acsnano.9b06394
134. Wei, H., Jiang, Q., Ampelli, C., et al.: Enhancing N_2 fixation activity by converting Ti_3C_2 MXenes nanosheets to nanoribbons. Chemsuschem **13**, 5614–5619 (2020). https://doi.org/10.1002/cssc.202001719
135. Kong, W.H., Gong, F.F., Zhou, Q., et al.: An MnO_2–$Ti_3C_2T_x$ MXene nanohybrid: an efficient and durable electrocatalyst toward artificial N_2 fixation to NH_3 under ambient conditions. J. Mater. Chem. A **7**, 18823–18827 (2019). https://doi.org/10.1039/c9ta04902a
136. Xiao, Y.P., Li, Y., Guo, Z.L., et al.: Functionalized Mo_2B_2 MBenes: promising anchoring and electrocatalysis materials for Lithium-Sulfur battery. Appl. Surf. Sci. **566**, 150634 (2021). https://doi.org/10.1016/j.apsusc.2021.150634
137. Yang, X.W., Shang, C.J., Zhou, S., et al.: MBenes: emerging 2D materials as efficient electrocatalysts for the nitrogen reduction reaction. Nanoscale Horiz. **5**, 1106–1115 (2020). https://doi.org/10.1039/d0nh00242a
138. Fu, Y., Richardson, P., Li, K.K., et al.: Transition metal aluminum boride as a new candidate for ambient-condition electrochemical ammonia synthesis. Nano Micro Lett. **12**, 1–13 (2020). https://doi.org/10.1007/s40820-020-0400-z
139. Huang, K., Zhao, Z., Du, H., et al.: Rapid thermal annealing toward high-quality 2D cobalt fluoride oxide as an advanced oxygen evolution electrocatalyst. ACS Sustain. Chem. Eng. **8**, 6905–6913 (2020). https://doi.org/10.1021/acssuschemeng.0c00830
140. Li, P.P., Liu, Z.C., Wu, T.W., et al.: Ambient electrocatalytic N_2 reduction to NH_3 by metal fluorides. J. Mater. Chem. A **7**, 17761–17765 (2019). https://doi.org/10.1039/c9ta04706a
141. Yu, J.Y., Chang, B., Yu, W.Q., et al.: Chromium phosphide nanoparticles embedded in porous nitrogen-/phosphorus-doped carbon as efficient electrocatalysts for a nitrogen reduction reaction. Carbon Energy **4**, 237–245 (2022). https://doi.org/10.1002/cey2.160
142. Guo, W.H., Liang, Z.B., Zhao, J.L., et al.: Hierarchical cobalt phosphide hollow nanocages toward electrocatalytic ammonia synthesis under ambient pressure and room temperature. Small Methods **2**, 1800204 (2018). https://doi.org/10.1002/smtd.201800204
143. Xing, C.Y., Wu, C.Y., Xue, Y.R., et al.: A highly selective and active metal-free catalyst for ammonia production. Nanoscale Horiz. **5**, 1274–1278 (2020). https://doi.org/10.1039/d0nh00287a
144. Wang, H., Wang, L., Wang, Q., et al.: Ambient electrosynthesis of ammonia: electrode porosity and composition engineering. Angew. Chem. Int. Ed. **57**, 12360–12364 (2018). https://doi.org/10.1002/anie.201805514
145. Liu, S.S., Wang, M.F., Qian, T., et al.: Facilitating nitrogen accessibility to boron-rich covalent organic frameworks via electrochemical excitation for efficient nitrogen fixation. Nat. Commun. **10**, 3898 (2019). https://doi.org/10.1038/s41467-019-11846-x

146. Mao, S.J., Wang, C.P., Wang, Y.: The chemical nature of N doping on N doped carbon supported noble metal catalysts. J. Catal. **375**, 456–465 (2019). https://doi.org/10.1016/j.jcat.2019.06.039
147. Kong, Y., Li, Y., Yang, B., et al.: Boron and nitrogen co-doped porous carbon nanofibers as metal-free electrocatalysts for highly efficient ammonia electrosynthesis. J. Mater. Chem. A **7**, 26272–26278 (2019). https://doi.org/10.1039/c9ta06076f
148. Yu, X.M., Han, P., Wei, Z.X., et al.: Boron-doped graphene for electrocatalytic N_2 reduction. Joule **2**, 1610–1622 (2018). https://doi.org/10.1016/j.joule.2018.06.007
149. Song, P.F., Kang, L., Wang, H., et al.: Nitrogen (N), phosphorus (P)-codoped porous carbon as a metal-free electrocatalyst for N_2 reduction under ambient conditions. ACS Appl. Mater. Interfaces **11**, 12408–12414 (2019). https://doi.org/10.1021/acsami.8b20472
150. Tian, Y., Xu, D.Z., Chu, K., et al.: Metal-free N, S co-doped graphene for efficient and durable nitrogen reduction reaction. J. Mater. Sci. **54**, 9088–9097 (2019). https://doi.org/10.1007/s10853-019-03538-0
151. Shi, L., Li, Q., Ling, C.Y., et al.: Metal-free electrocatalyst for reducing nitrogen to ammonia using a Lewis acid pair. J. Mater. Chem. A **7**, 4865–4871 (2019). https://doi.org/10.1039/c8ta11025e
152. Nong, W., Liang, H.K., Qin, S.H., et al.: Computational design of two-dimensional boron-containing compounds as efficient metal-free electrocatalysts toward nitrogen reduction independent of heteroatom doping. ACS Appl. Mater. Interfaces **12**, 50505–50515 (2020). https://doi.org/10.1021/acsami.0c15872
153. Ji, S., Wang, Z.X., Zhao, J.X.: A boron-interstitial doped C_2N layer as a metal-free electrocatalyst for N_2 fixation: a computational study. J. Mater. Chem. A **7**, 2392–2399 (2019). https://doi.org/10.1039/c8ta10497b
154. Zhao, J.X., Ren, X., Li, X.H., et al.: High-performance N_2-to-NH_3 fixation by a metal-free electrocatalyst. Nanoscale **11**, 4231–4235 (2019). https://doi.org/10.1039/c8nr10401h
155. Zhang, L.L., Ding, L.X., Chen, G.F., et al.: Ammonia synthesis under ambient conditions: selective electroreduction of dinitrogen to ammonia on black phosphorus nanosheets. Angew. Chem. Int. Ed. **58**, 2612–2616 (2019). https://doi.org/10.1002/anie.201813174
156. Sun, Y.T., Jiang, T.Y., Duan, J.J., et al.: Two-dimensional nanomesh arrays as bifunctional catalysts for N_2 electrolysis. ACS Catal. **10**, 11371–11379 (2020). https://doi.org/10.1021/acscatal.0c02745
157. Geng, Z.G., Liu, Y., Kong, X.D., et al.: N_2 electrochemical reduction: achieving a record-high yield rate of 120.9 μg_{NH_3} $mg_{cat.}^{-1}$ h^{-1} for N_2 electrochemical reduction over Ru single-atom catalysts. Adv. Mater. **30**, 1870301 (2018). https://doi.org/10.1002/adma.201870301
158. Rasool, A., Anis, I., Dixit, M., et al.: Tantalum based single, double, and triple atom catalysts supported on g-C_2N monolayer for effective nitrogen reduction reaction: a comparative DFT investigation. Catal. Sci. Technol. **12**, 310–319 (2022). https://doi.org/10.1039/d1cy01292d
159. Ju, H., Seo, D.H., Chung, S., et al.: Green ammonia synthesis using CeO_2/RuO_2 nanolayers on vertical graphene catalyst via electrochemical route in alkaline electrolyte. Nanoscale **14**, 1395–1408 (2022). https://doi.org/10.1039/d1nr06411h
160. Liu, W., Li, C., Xu, Q., et al.: Anderson localization in 2D amorphous MoO_{3-x} monolayers for electrochemical ammonia synthesis. ChemCatChem **11**, 5412–5416 (2019). https://doi.org/10.1002/cctc.201901171
161. Zhang, P., Xiong, W., Zhou, M.: Effect of nickel oxide morphology on the nitrogen electrochemical reduction reaction. Nano Mater. Sci. **2**, 353–359 (2020). https://doi.org/10.1016/j.nanoms.2020.03.002
162. Xu, Y.S., Xu, X., Cao, N., et al.: Perovskite ceramic oxide as an efficient electrocatalyst for nitrogen fixation. Int. J. Hydrog. Energy **46**, 10293–10302 (2021). https://doi.org/10.1016/j.ijhydene.2020.12.147
163. Luo, Y.R., Chen, G.F., Ding, L., et al.: Efficient electrocatalytic N_2 fixation with MXene under ambient conditions. Joule **3**, 279–289 (2019). https://doi.org/10.1016/j.joule.2018.09.011
164. Chu, K., Li, Q.Q., Liu, Y.P., et al.: Filling the nitrogen vacancies with sulphur dopants in graphitic C_3N_4 for efficient and robust electrocatalytic nitrogen reduction. Appl. Catal. B Environ. **267**, 118693 (2020). https://doi.org/10.1016/j.apcatb.2020.118693
165. Wang, Y., Cui, X.Q., Zhao, J.X., et al.: Rational design of Fe-N/C hybrid for enhanced nitrogen reduction electrocatalysis under ambient conditions in aqueous solution. ACS Catal. **9**, 336–344 (2019). https://doi.org/10.1021/acscatal.8b03802
166. Shi, M.M., Bao, D., Li, S.J., et al.: Anchoring PdCu amorphous nanocluster on graphene for electrochemical reduction of N_2 to NH_3 under ambient conditions in aqueous solution. Adv. Energy Mater. **8**, 1800124 (2018). https://doi.org/10.1002/aenm.201800124
167. Guo, Y.X., Yao, Z.Y., Timmer, B.J.J., et al.: Boosting nitrogen reduction reaction by bio-inspired FeMoS containing hybrid electrocatalyst over a wide pH range. Nano Energy **62**, 282–288 (2019). https://doi.org/10.1016/j.nanoen.2019.05.051
168. Lv, J.L., Wu, S.L., Tian, Z.F., et al.: Construction of PdO-Pd interfaces assisted by laser irradiation for enhanced electrocatalytic N_2 reduction reaction. J. Mater. Chem. A **7**, 12627–12634 (2019). https://doi.org/10.1039/c9ta02045d
169. Kwong, W.L., Wågberg, T., Messinger, J.: Electrochemical N_2 reduction at ambient condition: overcoming the selectivity issue via control of reactants' availabilities. Int. J. Hydrog. Energy **46**, 30366–30372 (2021). https://doi.org/10.1016/j.ijhydene.2021.06.184
170. Dubouis, N., Grimaud, A.: The hydrogen evolution reaction: from material to interfacial descriptors. Chem. Sci. **10**, 9165–9181 (2019). https://doi.org/10.1039/c9sc03831k
171. Liang, J.W., Ma, S.X., Li, J., et al.: Boosting the acidic electrocatalytic nitrogen reduction performance of MoS_2 by strain engineering. J. Mater. Chem. A **8**, 10426–10432 (2020). https://doi.org/10.1039/d0ta03622f
172. Mukherjee, S., Cullen, D.A., Karakalos, S., et al.: Metal-organic framework-derived nitrogen-doped highly disordered carbon for electrochemical ammonia synthesis using N_2 and H_2O in alkaline electrolytes. Nano Energy **48**, 217–226 (2018). https://doi.org/10.1016/j.nanoen.2018.03.059
173. Miyoshi, D., Sugimoto, N.: Molecular crowding effects on structure and stability of DNA. Biochimie **90**, 1040–1051 (2008). https://doi.org/10.1016/j.biochi.2008.02.009
174. Nakano, S.I., Miyoshi, D., Sugimoto, N.: Effects of molecular crowding on the structures, interactions, and functions of nucleic acids. Chem. Rev. **114**, 2733–2758 (2014). https://doi.org/10.1021/cr400113m
175. Ricci, F., Lai, R.Y., Heeger, A.J., et al.: Effect of molecular crowding on the response of an electrochemical DNA sensor. Langmuir **23**, 6827–6834 (2007). https://doi.org/10.1021/la700328r
176. Xie, J., Liang, Z.J., Lu, Y.C.: Molecular crowding electrolytes for high-voltage aqueous batteries. Nat. Mater. **19**, 1006–1011 (2020). https://doi.org/10.1038/s41563-020-0667-y
177. Peng, M.K., Wang, L., Li, L.B., et al.: Molecular crowding agents engineered to make bioinspired electrolytes for high-voltage aqueous supercapacitors. eScience **1**, 83–90 (2021). https://doi.org/10.1016/j.esci.2021.09.004
178. Song, Y., Johnson, D., Peng, R., et al.: A physical catalyst for the electrolysis of nitrogen to ammonia. Sci. Adv. **4**, e1700336 (2018). https://doi.org/10.1126/sciadv.1700336

179. Kim, K., Yoo, C.Y., Kim, J.N., et al.: Electrochemical synthesis of ammonia from water and nitrogen in ethylenediamine under ambient temperature and pressure. J. Electrochem. Soc. **163**, F1523–F1526 (2016). https://doi.org/10.1149/2.0741614jes
180. Sažinas, R., Andersen, S.Z., Li, K., et al.: Towards understanding of electrolyte degradation in lithium-mediated non-aqueous electrochemical ammonia synthesis with gas chromatography-mass spectrometry. RSC Adv. **11**, 31487–31498 (2021). https://doi.org/10.1039/d1ra05963g
181. Suryanto Bryan, H.R., Karolina, M., Jaecheol, C., et al.: Nitrogen reduction to ammonia at high efficiency and rates based on a phosphonium proton shuttle. Science **372**, 1187–1191 (2021). https://doi.org/10.1126/science.abg2371
182. Krempl, K., Pedersen, J.B., Kibsgaard, J., et al.: Electrolyte acidification from anode reactions during lithium mediated ammonia synthesis. Electrochem. Commun. **134**, 107186 (2022). https://doi.org/10.1016/j.elecom.2021.107186
183. Wan, Y.C., Wang, Z.J., Li, J., et al.: Mo_2C-MoO_2 heterostructure quantum dots for enhanced electrocatalytic nitrogen reduction to ammonia. ACS Nano **16**, 643–654 (2022). https://doi.org/10.1021/acsnano.1c07973
184. Zhang, W.Q., Shen, Y.L., Pang, F.J., et al.: Facet-dependent catalytic performance of Au nanocrystals for electrochemical nitrogen reduction. ACS Appl. Mater. Interfaces **12**, 41613–41619 (2020). https://doi.org/10.1021/acsami.0c13414
185. Niu, L.J., An, L., Wang, X.Y., et al.: Effect on electrochemical reduction of nitrogen to ammonia under ambient conditions: challenges and opportunities for chemical fuels. J. Energy Chem. **61**, 304–318 (2021). https://doi.org/10.1016/j.jechem.2021.01.018
186. Anantharaj, S., Noda, S.: Appropriate use of electrochemical impedance spectroscopy in water splitting electrocatalysis. ChemElectroChem **7**, 2297–2308 (2020). https://doi.org/10.1002/celc.202000515
187. Duran, S., Elmaalouf, M., Odziomek, M., et al.: Electrochemical active surface area determination of iridium-based mixed oxides by mercury underpotential deposition. ChemElectroChem **8**, 3519–3524 (2021). https://doi.org/10.1002/celc.202100649
188. Yoo, J.M., Shin, H., Chung, D.Y., et al.: Carbon shell on active nanocatalyst for stable electrocatalysis. Acc. Chem. Res. **55**, 1278–1289 (2022). https://doi.org/10.1021/acs.accounts.1c00727
189. Zhang, Z., Wu, S.S., Yang, C., et al.: Li-N_2 batteries: a reversible energy storage system? Angew. Chem. Int. Ed. **58**, 17782–17787 (2019). https://doi.org/10.1002/anie.201911338
190. Atencio, A.P., Aviles, J.R., Bolaños, D., et al.: Anti-corrosive additives for alkaline electrolyte in Al-air batteries: NH_4 VO_3 and polyoxometalates. Electrochem. Sci. Adv. **2**, e2100125 (2022). https://doi.org/10.1002/elsa.202100125
191. Lee, W.H., Choi, S.R., Kim, J.G.: Effect of agar as electrolyte additive on the aluminum-air batteries. J. Electrochem. Soc. **167**, 110503 (2020). https://doi.org/10.1149/1945-7111/ab9cc7

Sebastian Cyril Jesudass is a doctoral student in the department of material science and engineering at Chonnam National University, Republic of Korea. He received his bachelor's and master's degrees in physics from Bharathiar University, India in 2018 and 2020, respectively. His research focuses on the design of multifunctional electrocatalytic materials for sustainable energy conversion and storage applications.

Subramani Surendran is a research professor in the Hydrogen Energy Technology Laboratory at Korea Institute of Energy Technology (KENTECH), Republic of Korea. He received his Ph.D. degree in flexible hybrid supercapacitors and water electrolyzers from Bharathiar University, India. He completed a research internship at DGIST, Republic of Korea. Since then, he has been a postdoctoral researcher in the Department of Materials Science and Engineering at Chonnam National University until February 2022. His research focuses on the experimental and theoretical interplay of electrochemistry on developing new electrode materials that are multifunctional toward various energy storage and conversion devices.

Joon Young Kim received his Ph.D. degree in applied chemistry with Nam Ho Heo at the Kyungpook National University (KNU) in 2019. He is currently a research professor in the Hydrogen Energy Technology Laboratory at the Korea Institute of Energy Technology (KENTECH), Republic of Korea. He is attempting to find and develop new zeolitic quantum dots for energy production, conversion, and storage.

Tae-Yong An is an integrated master's and doctoral student in the Hydrogen Energy Technology Laboratory at the Korea Institute of Energy Technology (KENTECH), Republic of Korea. He received his bachelor's degree in physics from Chosun University, Republic of Korea, in 2016. His research focuses on electrochemical ammonia synthesis under ambient conditions.

Gnanaprakasam Janani received her B.Sc. and M.Sc. in Physics in 2011 and 2013 from Bharathiar University, India. She obtained her Ph.D. degree in Material Science and Engineering at Chonnam National University, Republic of Korea, in 2022, working with Prof. Uk Sim. She is currently a postdoctoral researcher in the Hydrogen Energy Technology Laboratory at the Korea Institute of Energy Technology (KENTECH), Republic of Korea. She has broad interests in energy conversion and storage devices in the specific areas of bifunctional/multifunctional electrocatalysts for water splitting and rechargeable zinc-air batteries.

Tae-Hoon Kim is an assistant professor in the Department of Materials Science and Engineering at Chonnam National University, Republic of Korea. He received his bachelor's, M.S., and Ph.D. degrees from Sungkyunkwan University (SKKU) in 2010, 2012 and 2016, respectively. In 2012–2015, he was granted the Global Ph.D. Fellowship by National Research Foundation of Korea (NRF Korea). He worked at Ames Laboratory in USA as a postdoctoral research associate for 4 years (2017–2021). He joined Chonnam National University in 2021. His research interests include multiscale materials characterization with electron microscopy, microstructure and relating physical properties in various materials such as semiconductors, metals, magnets and nanomaterials.

Jung Kyu Kim is a tenure-track associate professor at the School of Chemical Engineering, Sungkyunkwan University (SKKU), Republic of Korea. He received his bachelor's, M.S., and Ph.D. degrees from SKKU in 2010, 2012 and 2015, respectively. In 2012–2015, he was granted the Global Ph.D. Fellowship by NRF Korea. In 2015–2018, he was a postdoctoral research scholar at Stanford University, USA. Since 2018, his research group focuses on the diverse energy conversions with tailored nanostructures including solar-to-electric, solar-to-electrochemical, and electric-to-chemical energy conversions.

Uk Sim is an associate professor in the Hydrogen Energy Technology Laboratory at Korea Institute of Energy Technology (KENTECH), Republic of Korea. He received his B.S., (2007), M.S., (2009), and Ph.D. degrees (2016) from Seoul National University. Since then, he has been a postdoctoral scholar at Stanford University until 2017. He was an associate professor in the Department of Materials Science and Engineering at Chonnam National University. He serves as the founder and CEO of Neel Sciences Inc., a research institute. His research focuses mainly on developing nanomaterials for energy production, conversion, storage, and renewable energy produced by photo- or electrochemical reactions to create a future sustainable energy system.